1 OF 2
AD
A038159

Characterization of MX Upper Stage Subscale Carbon-Carbons

ADA038159

Materials Sciences Laboratory
The Ivan A. Getting Laboratories
The Aerospace Corporation
El Segundo, Calif. 90245

11 March 1977

Interim Report

Prepared for

AIR FORCE ROCKET PROPULSION LABORATORY
Edwards Air Force Base, Calif. 93523

SPACE AND MISSILE SYSTEMS ORGANIZATION
AIR FORCE SYSTEMS COMMAND
Los Angeles Air Force Station
P.O. Box 92960, Worldway Postal Center
Los Angeles, Calif. 90009

AD No.
DDC FILE COPY

This report was submitted by The Aerospace Corporation, El Segundo, CA 90245, under Contract F04701-76-C-0077 with the Space and Missile Systems Organization, P. O. Box 92960, Worldway Postal Center, Los Angeles, CA 90009. It was reviewed and approved for The Aerospace Corporation by W. C. Riley, Director, Materials Sciences Laboratory. W. Payne, MKCC, was the project engineer.

This report has been reviewed by the Information Office (OI) and is releasable to the National Technical Information Service (NTIS). At NTIS, it will be available to the general public, including foreign nations.

This technical report has been reviewed and is approved for publication. Publication of this report does not constitute Air Force approval of the report's findings or conclusions. It is published only for the exchange and stimulation of ideas.

GERHARD E. AICHINGER
Technical Advisor
Contracts Management Office

FOR THE COMMANDER

FRANK J. BANE
Chief, Contracts Management Office

(19) REPORT DOCUMENTATION PAGE		READ INSTRUCTIONS BEFORE COMPLETING FORM
1. REPORT NUMBER (18) SAMSO-TR-77-34	2. GOVT ACCESSION NO.	3. RECIPIENT'S CATALOG NUMBER
4. TITLE (and Subtitle) (6) CHARACTERIZATION OF MX UPPER STAGE SUBSCALE CARBON-CARBONS.		5. TYPE OF REPORT & PERIOD COVERED (9) Interim rept.
		6. PERFORMING ORG. REPORT NUMBER (14) TR-0077(2622-02)-1
7. AUTHOR(s) (10) Jay G. Baetz, J. Stephen Evangelides, Anthony F. DiGiacomo		8. CONTRACT OR GRANT NUMBER(s) (15) F04701-76-C-0077
9. PERFORMING ORGANIZATION NAME AND ADDRESS The Aerospace Corporation Mat. Sc. Lab El Segundo, Calif. 90245		10. PROGRAM ELEMENT, PROJECT, TASK AREA & WORK UNIT NUMBERS (12) 123 p.
11. CONTROLLING OFFICE NAME AND ADDRESS Air Force Rocket Propulsion Laboratory Edwards AFB, Calif. 93523		12. REPORT DATE (11) 11 Mar 1977
		13. NUMBER OF PAGES 120
14. MONITORING AGENCY NAME & ADDRESS(If different from Controlling Office) Space and Missile Systems Organization Air Force Systems Command Los Angeles, Calif. 90009		15. SECURITY CLASS. (of this report) Unclassified
		15a. DECLASSIFICATION/DOWNGRADING SCHEDULE

16. DISTRIBUTION STATEMENT (of this Report)

Approved for public release; distribution unlimited.

17. DISTRIBUTION STATEMENT (of the abstract entered in Block 20, if different from Report)

18. SUPPLEMENTARY NOTES

19. KEY WORDS (Continue on reverse side if necessary and identify by block number)

Solid Rocket Nozzels
Carbon-Carbon Materials
Microstructure
Material Characterization
Crack Propagation
Surface Roughness
Thermal Expansion

20. ABSTRACT (Continue on reverse side if necessary and identify by block number)

The most significant characteristics of the carbon-carbon materials employed by Aerojet Solid Propulsion Company in the MX upper-stage subscale nozzle tests have been determined. These carbon-carbons included two dimensionally reinforced structures of both flat laminate and rosette construction as well as a three dimensionally reinforced composite.

19. KEY WORDS (Continued)

20. ABSTRACT (Continued)

Results of these studies characterize the materials by their response to the original fabrication process and to the rocket test environment.

The evaluation concentrated on microstructural and macrostructural examination, posttest surface roughness measurements, thermal expansion and thermal stability of the composite, and evaluation of the density/porosity/pore structural relationships.

Conclusions regarding the materials' operating performance and processing conditions are given, and recommendations for future studies are presented.

PREFACE

The Project Engineer for the Air Force Rocket Propulsion Laboratory was W. Payne, MKCC, and the Principal Investigator for The Aerospace Corporation was J. G. Baetz.

The authors wish to express their appreciation for the invaluable assistance of J. Jortner and F. Clayton of McDonnell-Douglas Corporation in making the surface roughness characterizations.

CONTENTS

FIGURES

FIGURES (Continued)

FIGURES (Continued)

FIGURES (Continued)

FIGURES (Continued)

I. INTRODUCTION AND SUMMARY

As part of the effort to develop a nozzle for the MX Upper Stage Advanced Development Motor under Air Force Space and Missile Systems Organization Contract F04701-73-C-0423, Aerojet Solid Propulsion Company (ASPC) has examined several carbon-carbon candidate materials. These materials were employed as entrance caps and throat supports for two subscale nozzle tests. Because the family of advanced, high-density carbon-carbons is in a very early stage of development, little is understood of either the fabrication process itself or the materials' response to the rocket motor environments. The former is true because of changes that are constantly being introduced to the processing procedure in an attempt to produce a superior performing product. The latter is true because of the complex and heterogeneous nature of the carbon-carbon family itself.

The Aerospace Corporation, under the direction of the Air Force Rocket Propulsion Laboratory (AFRPL), conducted a series of material characterization tasks. These tasks were planned to provide structural and environmental response data for ASPC design analysis verification and they consisted of the following elements:

1. The microstructure of each material was defined through the use of scanning electron microscopy (SEM) of etched and un-etched flamefront and backface surfaces. Electron diffraction x-ray analysis (EDAX) was used in conjunction with the SEM where analysis of foreign surface materials was desired. Metallographic techniques were employed in order to examine polished sections of each material.

2. Low-magnification photomicrographs were taken in each of the primary reinforcement directions of the 3D entrance in order to assess the as-processed material construction.

3. Crack propagation characteristics of the 3D material were developed and documented by photomicrographs in the SEM. This technique has proven to be a useful tool in evaluating reentry carbon-carbons.

4. The surface roughness characteristics of both entrance caps were defined and quantified. This task was accomplished by

PRECEDING AGE BLANK NOT FILMED

McDonnell-Douglas Corporation, Huntington Beach, Calif., whose effort in this area is gratefully acknowledged.

5.   Thermal expansion excursions were measured for each material up to 5072°F. The stability of the materials was examined by thermal cycling techniques. The thermal expansions of both throat supports were determined in the with-ply and cross-ply direction near both the flamefront and the backface. Three thermal expansions of the rosette entrance were measured with and across the primary reinforcement planes. The 3D material had its thermal expansions measured in each of the three polar coordinates, i.e., axial, radial, and circumferential.

6.   In a continued attempt to better define the relationship that performance has to this family of properties, pore size distributions, open-to-closed porosity relationships, bulk and real apparent densities, and specific pore volumes were determined at the fired surface, in the interior, and at the backface for each carbon-carbon.

The four carbon-carbon materials that were characterized consisted of two entrance caps and two throat retainers of the configurations shown in Fig. 1. Entrance SN001 was a rosette structure designated AG Carb 101 (K408). The plies were laid parallel to the centerline with a zero degree helix angle. The arc angle of the part was measured as 14 deg o.d. and 36 deg i.d. These values are in agreement with the 26 deg average reported by ASPC. The general posttest appearance of this part was good when we consider that it was not fabricated for use as a flamefront material. There were axial groves at 40 deg intervals around the circumference of the part. It is understood from conversations with ASPC that each groove corresponded to a slot in the propellant grain. The average bulk density of the part was measured as 1.595 g/cm^3 with an open porosity of 7%. The average secant coefficient of thermal expansion (CTE) with ply was 2.3 in./in/°F from room temperature to 5000°F. The cross-ply value was 3.2 in./in/°F. The posttested stability of the composite was quite good.

Entrance SN002 was a woven 3D consisting of Thornel 50 reinforcement with a pitch/resin matrix. The weave geometry resulted in the measured values detailed in an illustration presented later in the report. The
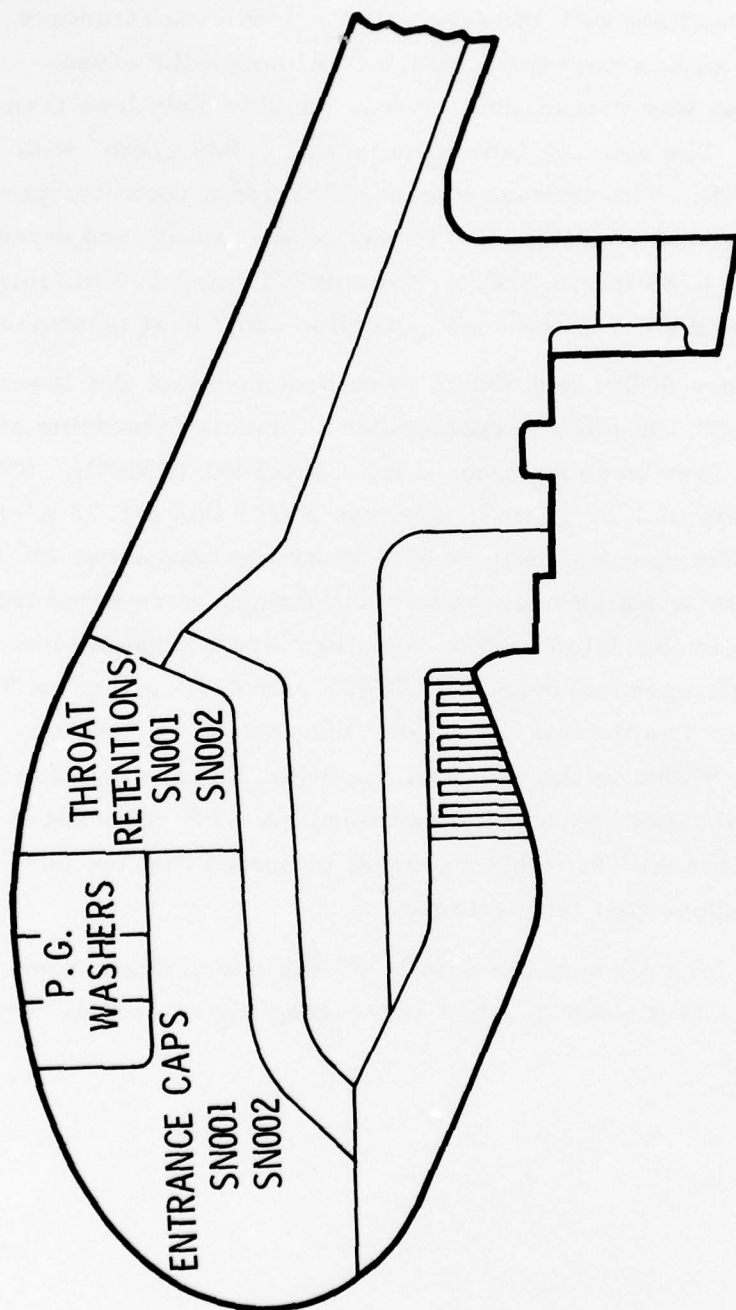
Figure 1. Nozzle Design

results were in good agreement with the fabricator's predicted structure. The posttest appearance of this part was uniform. Although the aforementioned SN002 grooving was measurable, it was considerably less than that observed in SN001. The average bulk density was 1.829 g/cm^3 with an open porosity of 8 1/2%. The average secant CTEs from room temperature to 5000°F in the as-fired condition and in the axial, radial, and circumferential directions were 0.85 in./in./°F, 1.9 in./in./°F, and 1.5 in./in./°F, respectively. There was a shift in thermal expansion after heat treatment.

Both throat retainers SN001 and SN002 were processed as flat laminate compression moldings with the plies perpendicular to nozzle centerline and varied only in density. They were designated AG Carb 5451 (K550D). SN001 had a nominal bulk density of 1.57 g/cm^3, whereas SN002 had a 1.73 g/cm^3 average bulk density. The open porosity of both retainers was about 7%. Considerable delaminations, which occurred during firing, were noted for both parts. The density in the delaminated, or valley areas, was as low as 1.53 g/cm^3 at over 9% open porosity for SN001 and 1.68 g/cm^3 at 9% open porosity for SN002. The thermal expansion excursions varied considerably from SN001 to SN002 in the as-fired condition. This variation was observed in both with- and cross-ply directions. A CTE reversal at about 4000°F was noted for SN001. This reversal indicated that the part had not been stabilized above that temperature.

The following sections present the details of this characterization study and the conclusions that were reached concerning the materials' processing and performance.

II. PROCEDURES AND RESULTS

A. CUTTING PLANS AND CHARACTERIZATION PROCEDURES

1. INCOMING MATERIAL

All test specimens received were examined for possible damage incurred in shipment. Upon acceptance of test specimens, the shipping invoice was verified and special instructions were duplicated. One copy was retained by the engineer accepting the specimens and one copy remained with the specimens. A work statement was initiated. The following statement of work was used for entrance SN001 AG Carb 101 Rosette, entrance SN002 FMI T50 3D cylindrical weave, and throat supports SN001 and SN002 AG Carb 5451 flat laminate. A cutting outline for these materials is shown in Fig. 2 (largest section for thermal expansion).

1. Metallography - Polish longitudinally cut section and radial/circumference surface (90 deg per section cut).

2. SEM - Scan fired surface and backside surface SEM photograph, as appropriate.

3. Porosity - Determine pore size distribution with mercury porosimeter and nitrogen adsorption techniques at three places, i.e., fired surface, backside surface, and internal.

4. Thermal Expansion - Determine the with-ply and cross-ply thermal expansion excursions room temperature to 5072°F at the near-fired surface and at the backside. Determine stability by rerunning 5072°F heated parts in each case.

The rationale used in drafting the work statement was: (1) to understand the as-fabricated condition of the specimen and (2) to generate an understanding of the reasons each material behaves as it does in the rocket motor environment.

2. SAMPLE PREPARATION

A specimen cutting plan was drafted after receiving the work statement. Sketches of each specimen were drawn. Figure 2 shows the cutting

ENTRANCE SN001 AG CARB 101 ROSETTE

THERMAL EXPANSION — POROSITY

SEM

METALLOGRAPHY

⑤ ③ ② ①

④ SURFACE ROUGHNESS

WITH PLY

THRU PLY-AXIS
CHANGES WITH
ROSETTE

ENTRANCE SN002 FMI T50 3D
CYLINDRICAL WEAVE

METALLOGRAPHY
AND ALIGNMENT

POROSITY

RADIAL

① ③ ②

⑤ ④

SEM AND SURFACE
ROUGHNESS

THERMAL EXPANSION
AND STABILITY

AXIAL

CIRCUMFERENTIAL

CRACK PROPAGATION

THROAT SUPPORTS SN001 AND
SN002 AG CARB 5451 FLAT LAMINATE

① ②

METALLOGRAPHY

③ ④

SEM

POROSITY

THERMAL EXPANSION
AND THERMAL STABILITY

Figure 2.   Cutting Plan for MX Upper Stage Subscale
Carbon-Carbon Characterization

plans for each of the entrances and throat retainers. Specific axes of orientation were identified, and areas from which samples were removed were coded as follows: (1) optical microscopy, (2) SEM, (3) porosity, and (4) thermal expansion.

Upon completion of the cutting plan, information describing each specimen was logged in a laboratory notebook that provided a cross reference of specimen identification versus laboratory function to be performed. Each specimen was also resketched, and the overall dimensions were recorded. Following the established test plan, the specimens were cross sectioned. Test specimens were removed by use of a wire saw, jewelers saw, or bandsaw, as applicable. (Precise sectioning of delicate material is usually accomplished with an automated fine-cut wire saw.)

3. PROCESSING

Each specimen removed was individually packaged and the appropriate identification number was attached with a sketch that provided the laboratory personnel with the following information: (1) task to be performed, (2) surface of interest, (3) principal axes of the material, and (4) special instructions as required. Figures 3 and 4 show the general processing plans for the two entrance carbon-carbons.

Upon completion of the assigned task, the data were reviewed with the person who performed the experiment. All photographs were identified and logged. Test results were transmitted to the requesting engineer for review. After the results were accepted, the test specimens and larger scraps of material were gathered and stored.

B. MICROSTRUCTURE

1. ENTRANCE SN001 – AG CARB 101 ROSETTE

The general appearance of the rosette entrance indicated an adequate level of performance, especially when we consider that this material was originally intended for use as a substrate. The reported erosion rate was

ENTRANCE SN001
AG CARB 101

POLISH AND
PHOTOGRAPH
(90 frm sect)

LONGITUDINAL SECTION

FIRED SURFACE   METALLOGRAPHY

POLISH SURFACE AND PHOTOGRAPH
ROSETTE STRUCTURE

FIRED SURFACE   SEM

SEM SCAN FOR SURFACE EFFECTS FROM FIRING

EXAMINE BACKFACE FOR AS-PROCESSED STRUCTURE
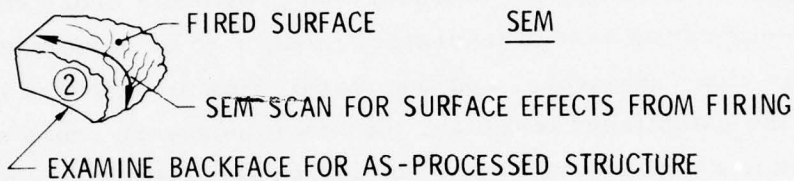
FIRED SURFACE   POROSITY
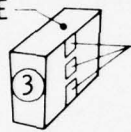
OBTAIN PORE SIZE DIST COMBO Hg POROSIMETER
AND N_2 ADSORPTION ON FIRED FACE, BACKFACE
AND INTERIOR

SURFACE ROUGHNESS

PROVIDE McDONNELL DOUGLAS WITH SECTION ④
FOR SURFACE ROUGHNESS EXPERIMENT

FIRED SURFACE   THERMAL EXPANSION AND STABILITY

MEASURE THERMAL EXPANSION WITH-PLY AND CROSS-PLY
TO 5072°F - RERUN TO CHECK THERMAL STABILITY

NOTE: Axis do not comply with part axis since this
is a rosette structure with-ply and crossply
directions will have to be determined visually
from $\Delta L/L_0$ section

Figure 3.   MX Upper Stage Subscale Carbon-Carbon
Characterization Processing Plan

-18-

ENTRANCE SN002   FMI T50 3D   METALLOGRAPHY

AXIALLY OR
LONGITUDINALLY
SECTIONED SURFACE   POLISH SURFACE - PHOTOGRAPH
                                                TO SHOW AXIAL AND RADIAL FIBER
                                                ALIGNMENT WITH CIRCUMFERENTIAL
POLISH SURFACE   YARN BUNDLE ENDS

MAINTAIN EXISTING CURVATURE.   POLISH SURFACE - PHOTOGRAPH TO SHOW
PHOTOGRAPH TO SHOW CIRCUM-   RADIAL ALIGNMENT WITH AXIAL BUNDLE ENDS
FERENTIAL AND AXIAL FIBER
ALIGNMENT WITH RADIAL YARN
BUNDLE ENDS   SEM AND SURFACE ROUGHNESS

                                    FIRED SURFACE

AXIALLY SECTIONED SURFACE   SEM EXAMINATION FOR SURFACE
                                                EFFECTS DUE TO FIRING

CIRCUMFERENTIALLY SECTIONED SURFACE   SEM EXAMINATION OF BACKFACE
                                                FOR AS-PROCESSED SURFACE CONDITION

UPON COMPLETION, DELIVER TO McDONNELL
DOUGLAS FOR SURFACE ROUGHNESS EXPERIMENTATION
                                    FIRED SURFACE   POROSITY
CENTER SECTION
(all vertical surfaces cut)   OBTAIN PORE SIZE DISTRIBUTION USING
                                                COMBINATION OF Hg POROSIMETER AND
                                                NITROGEN ADSORPTION TECHNIQUES - OF
                                                FIRED SURFACE, OUTER SURFACE AND INTERIOR

                                                CRACK PROPAGATION

FIRED SURFACE
                                    LONGITUDINAL SECTION

                                                SECTION FOR CRACK PROPAGATION STUDIES

RADIAL DIRECTION

                                                THERMAL EXPANSION AND STABILITY
                            FIRED SURFACE
                                                MEASURE AXIAL, RADIAL AND CIRCUMFERENTIAL
CIRCUMFERENTIAL   RADIAL   THERMAL EXPANSION TO 5072°F - REMEASURE
(curved surface)   TO CHECK MATERIAL STABILITY
                                   AXIAL

Figure 4.   MX Upper Stage Subscale Carbon-Carbon
            Characterization Processing Plan

consistent with the measured average bulk density of 1.596 g/cm^3 (Section II.E). There were indications of preferential erosion/corrosion along the angle of the rosette plies, particularly where the entrance face presented a near normal aspect ratio to the gas stream. Sections 1 and 2 shown in the cutting plan (Fig. 2) were transmitted to metallography and SEM for microstructural examination. There they were potted and polished (metallography only) in accordance with standard procedures. Figure 5 illustrates the various locations where photomicrographs were taken. Figure 6 is a reference photograph that shows the potted metallography sample. Figures 7 and 8 are magnified sections of the flamefront surface at locations 2 and 3, respectivel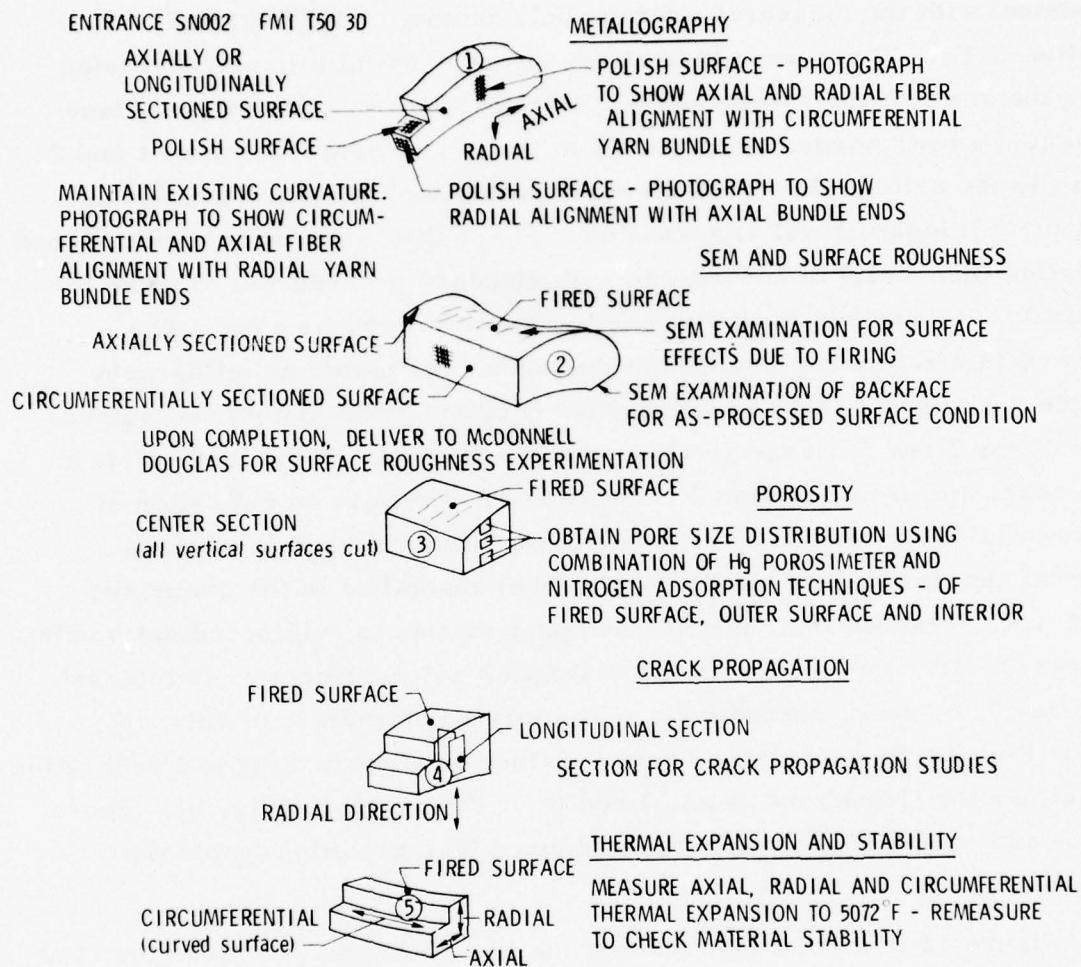y. The gas flow was from right to left in each case, and from location 2 to location 1. There is no indication of preferential attack due to fiber orientation. The mechanism of mass removal appears more dependent upon local anomalies in the composite itself, i.e., cracked fiber bundles and poor matrix to reinforcement binding. Figures 9, 10, and 11 depict the magnified microstructure at internal locations 3, 4, and 5, respectively. The internal structure of entrance SN001 (Fig. 10) has a greater degree of fiber bundle cracking and separation than either the flamefront (Figs. 7 and 8) or the backface (Fig. 9). These cracks and separations are probably induced by fabrication (cooldown) stresses.

Figure 12 is a reference photograph that shows the locations for SEM examination taken from Fig. 5. Figures 13-20 are various magnification SEM photomicrographs of the surface areas pointed out in Figure 5. Of particular note is the obscuring of the surface by a phase of carbon deposition similar to the one noted in the MX lower stage subscale characterization studies. This deposition is evident at higher magnification in all areas of this entrance (Figs. 14, 16, and 18). The backface photomicrographs (Figs. 19 and 20) are of limited value in examining the structure because of the large amount of debris on the surface. These debris appear to be the carbon residue from a bond surface.

METALLOGRAPH SECTIONS
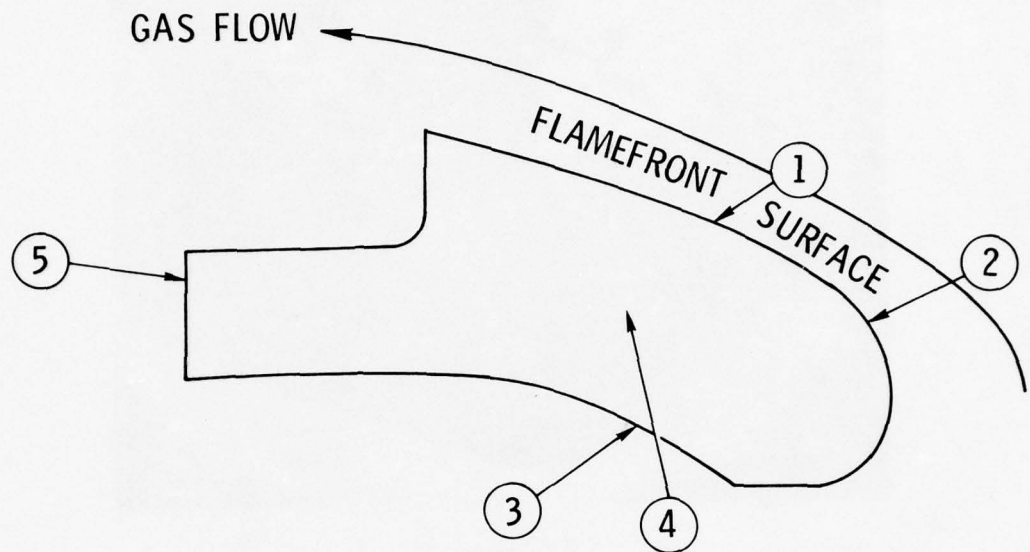
SEM SURFACES
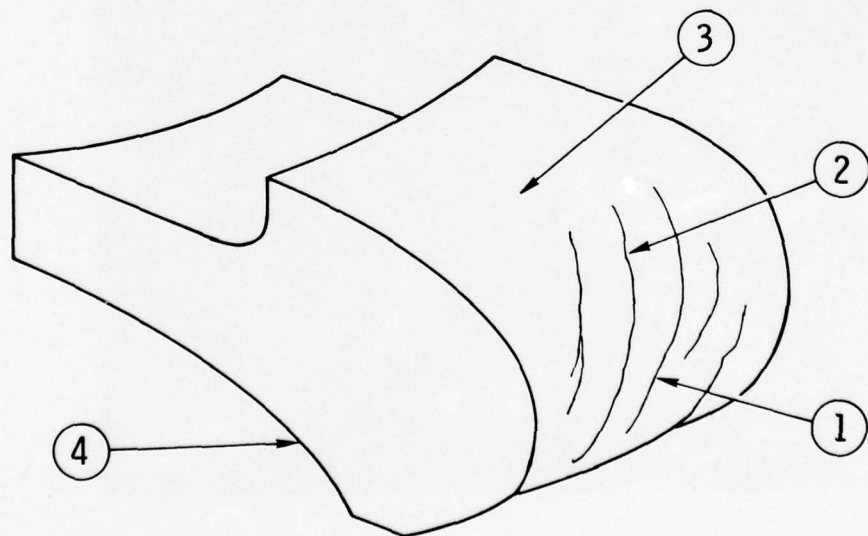
Figure 5. Microphotograph Locations, Entrance SN001
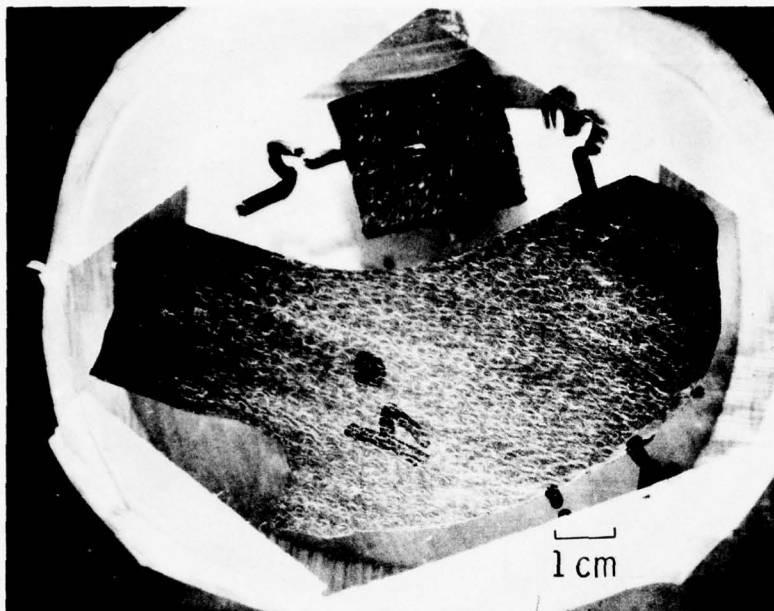
Figure 6. Entrance SN001 AG Carb 101 (K 408)
Metallograph Reference Photograph
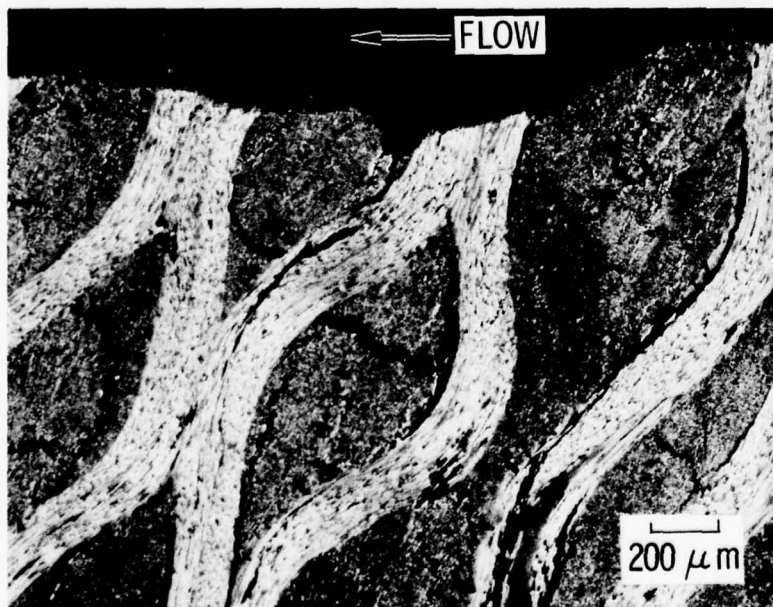
Figure 7. Entrance SN001 Metallograph
Location 1 (200 μm)
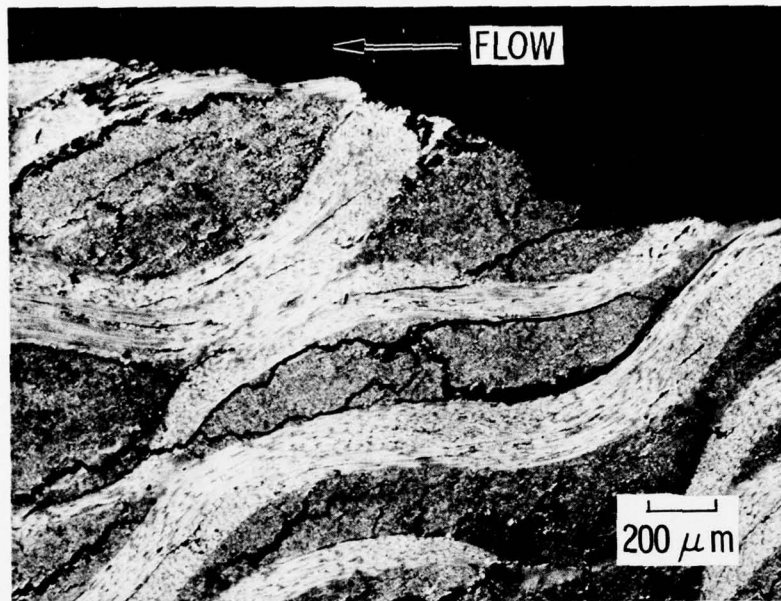
Figure 8. Entrance SN001 Metallograph
Location 2 (200 μm)
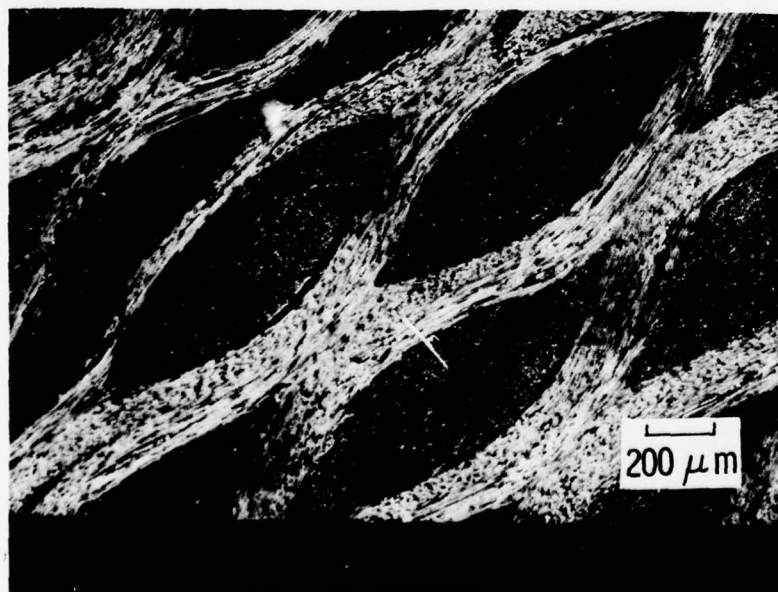
Figure 9. Entrance SN001 Metallograph
Location 3 (200 μm)
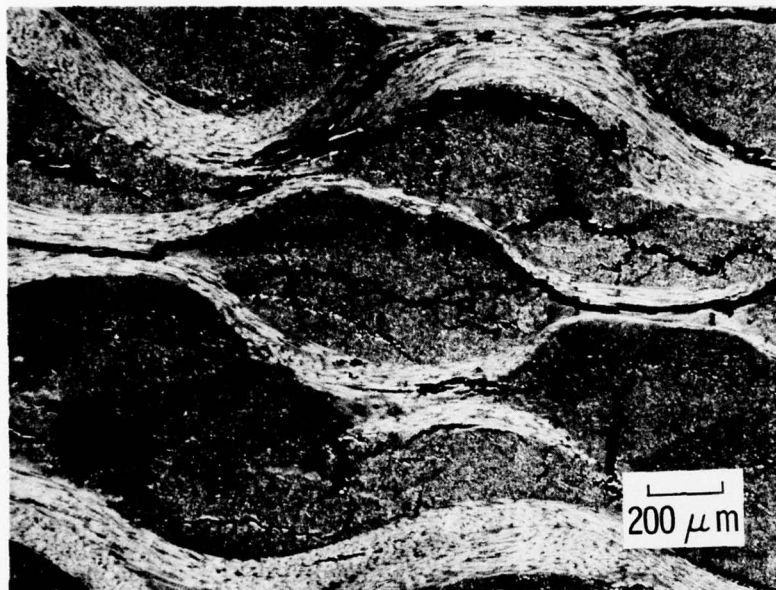
Figure 10. Entrance SN001 Metallograph
Location 4 (200 μm)
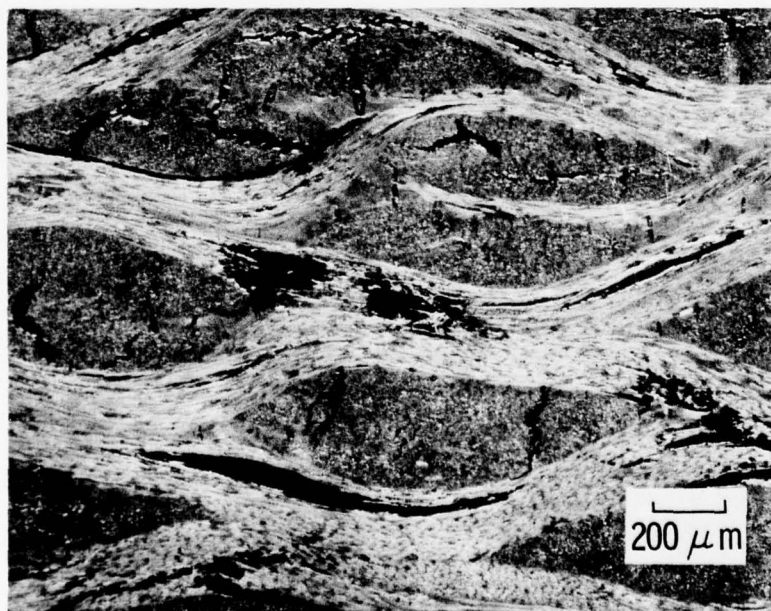
Figure 11. Entrance SN001 Metallograph
Location 5 (200 μm)
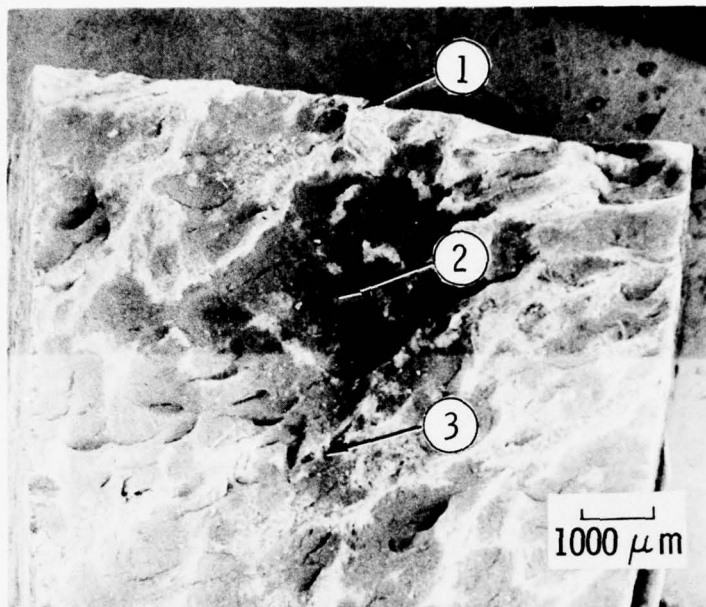
Figure 12. Entrance SN001 AG Carb 101 (K 408)
SEM Reference Photograph
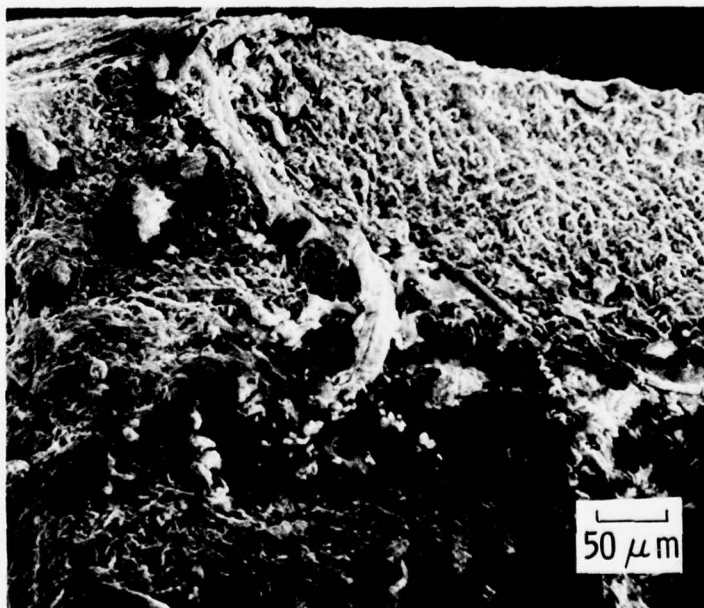
Figure 13. Entrance SN001 SEM Location 1 (50 μm)
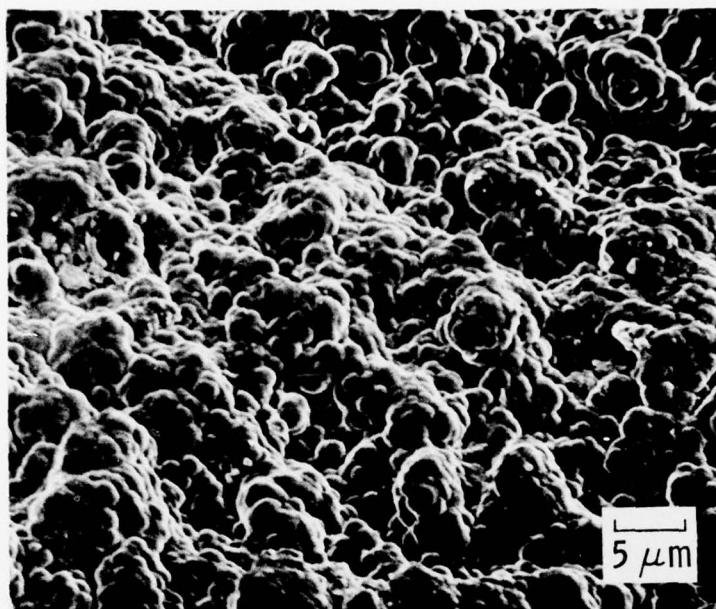
Figure 14.   Entrance SN001 SEM Location 1 (5 μm)
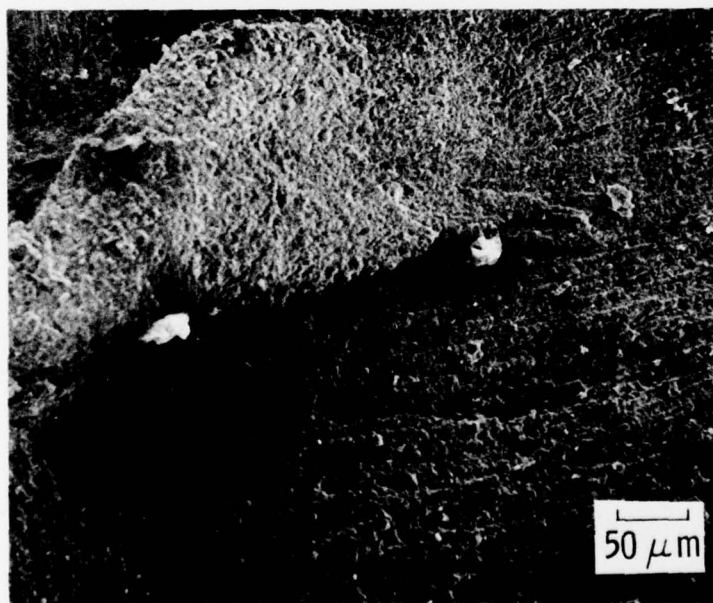
Figure 15.   Entrance SN001 SEM Location 2 (50 μm)
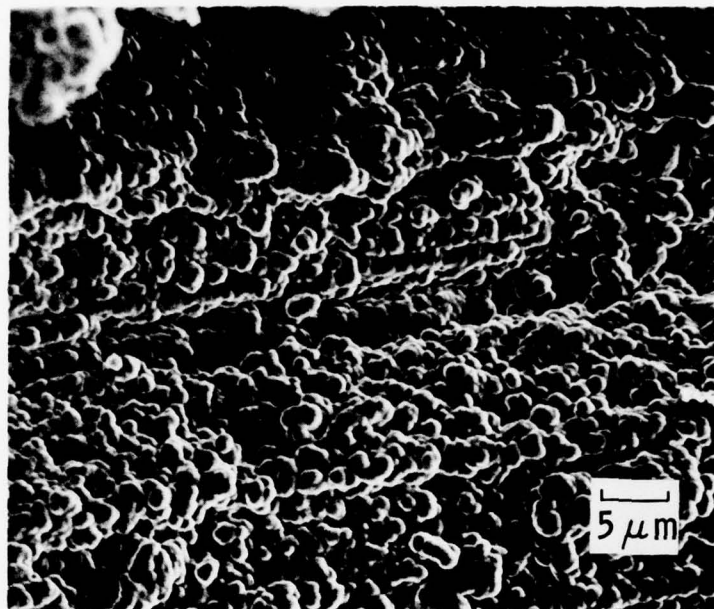
Figure 16.   Entrance SN001 SEM Location 2 (5 μm)
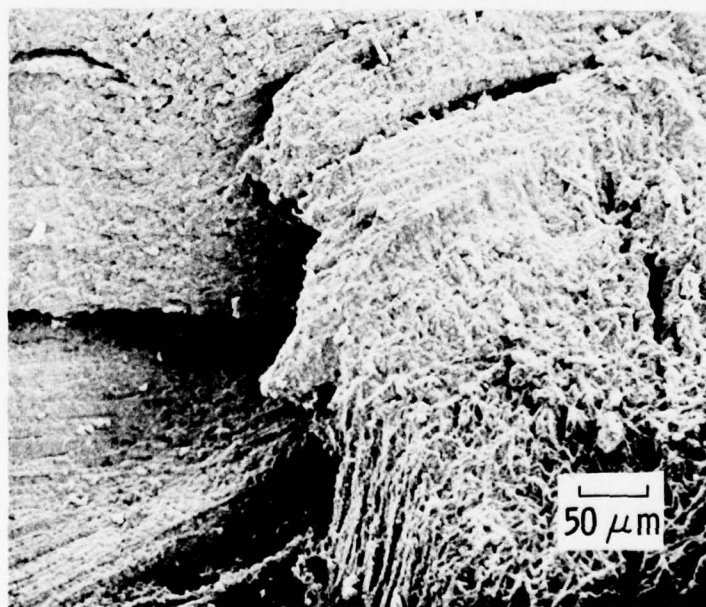
Figure 17.   Entrance SN001 SEM Location 3 (50 μm)
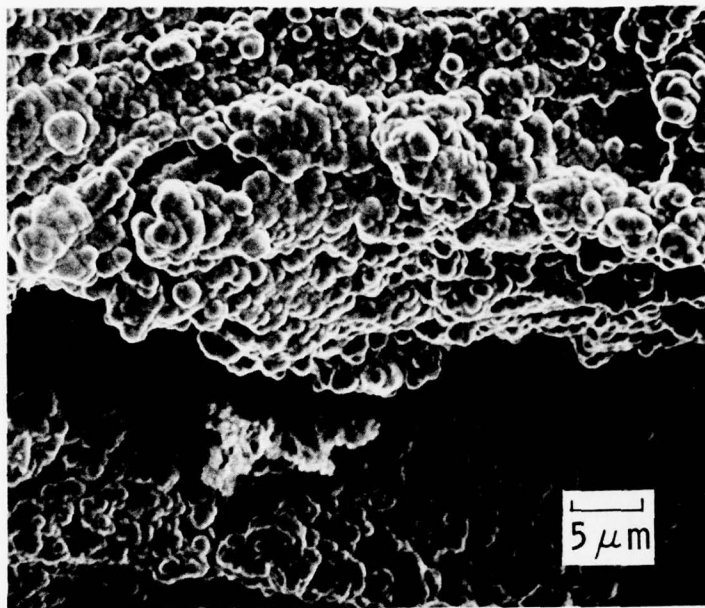
Figure 18. Entrance SN001 SEM Location 3 (5 μm)
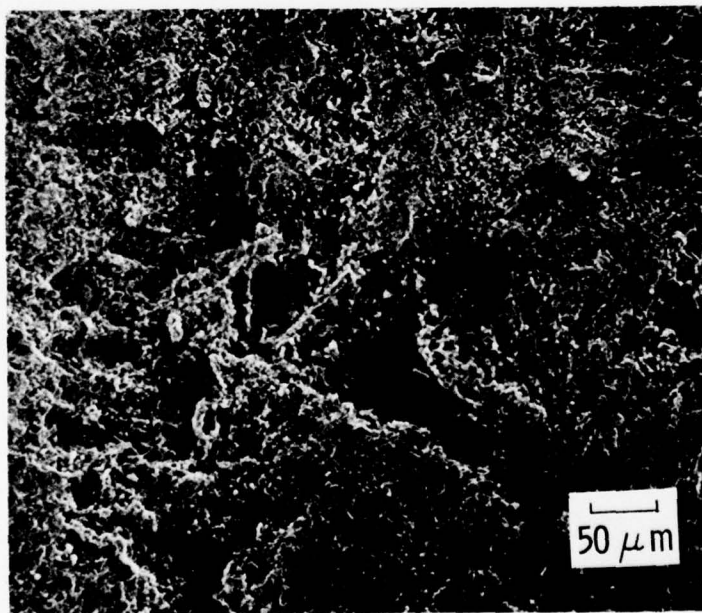
Figure 19. Entrance SN001 SEM Location 4 (50 μm)
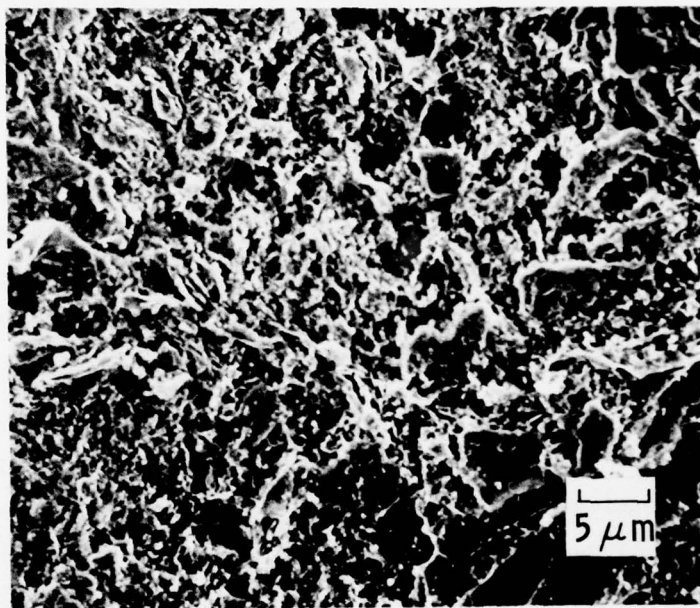
Figure 20. Entrance SN001 SEM Location 4 (5 µm)

2. ENTRANCE SN002 – FMI T50 3D CYLINDRICAL WEAVE

The 3D reinforcement composite represents a particularly interesting material concept for achieving performance improvements in the rocket nozzle environment. For this reason, special emphasis has been placed upon the examination of entrance SN002. Therefore, in addition to the microstructural examination of the fired sections and surfaces, an evaluation of the basic weave geometry was conducted. In addition, an experimental crack propagation study was conducted on this material. The results of these efforts are presented in this section.

An examination of the weave geometry indicated that the overall pattern was reasonably symmetrical throughout the body of the part. The normality of axials to radials was consistent. There was some variation of the circumferential fiber pattern from a truly circular pattern in the radial direction as well as a deviation from a true cylindrical configuration in the axial direction, but, in general, the structure appeared consistent with similarly constructed parts. A random location on the tested part was selected for measuring the weave geometry. A section was removed, potted, polished, and examined optically on the Leitz metallograph. The center-to-center spacings of the fiber bundles were measured in the three primary reinforcement directions and compared with data supplied by Fiber Materials, Inc. (FMI). The results depicted in Fig. 21 show the close agreement between the measured and the preform geometry predictions of FMI.

The posttest microstructural analyses of entrance SN002 were designed to assess the type and number of material changes occurring at and beneath the fired surface. These analyses entailed scanning electron microscopy of fired samples and observation of crack propagation in subsurface regions. The crack propagation evaluation was conducted on only one of the four materials, ENT002. These types of microstructural analyses will ultimately result in recommendations for improved material fabrication procedures.
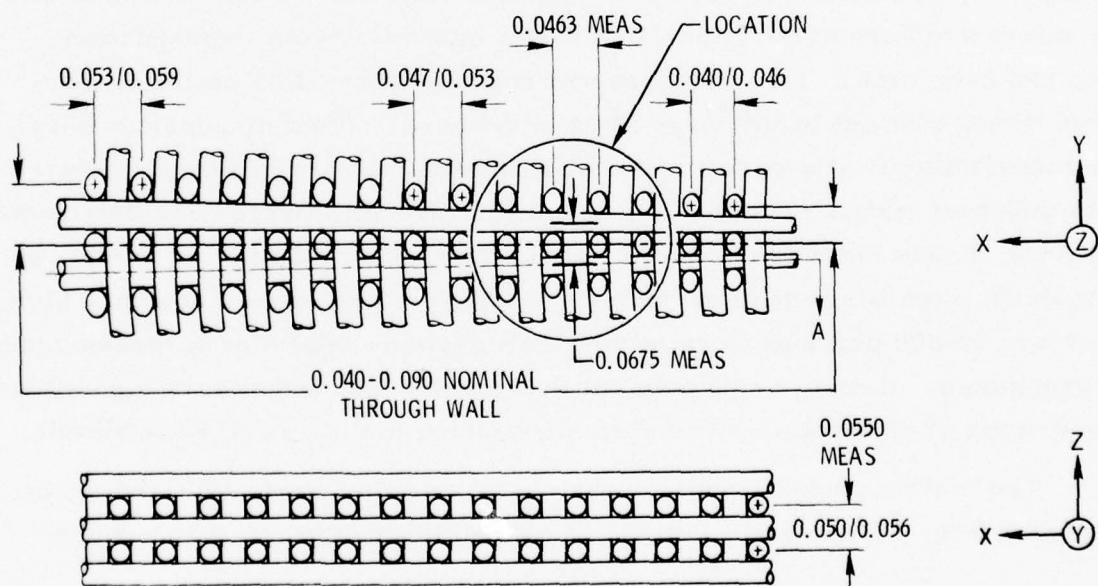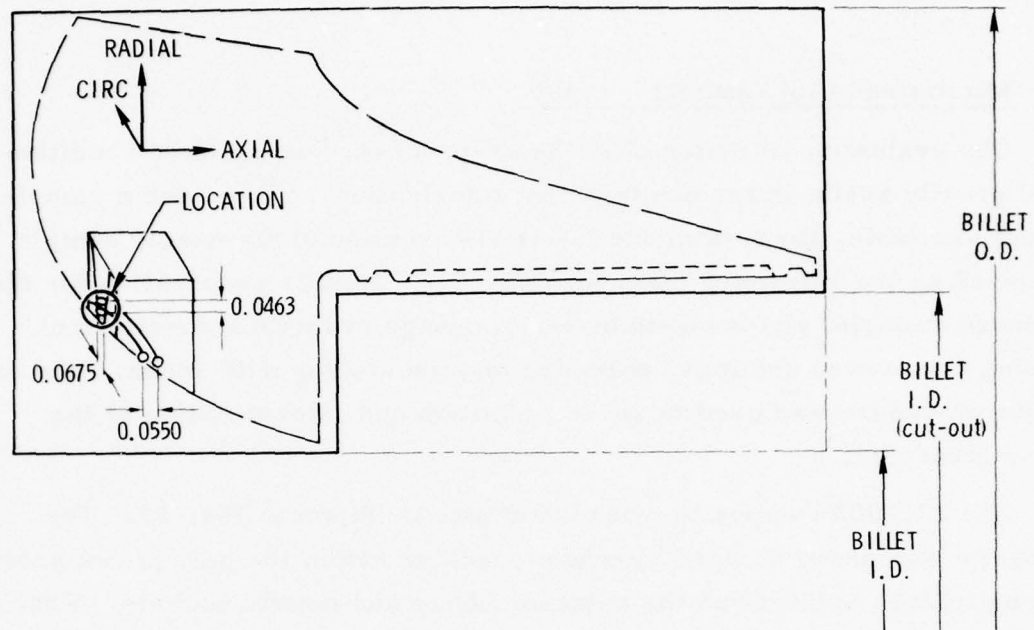
Figure 21. Entrance SN002 Preform Geometry
(dimensions in inches)

-31-

a. Microstructural Characterization

The evaluation of material in the as-processed or prefired condition would greatly assist in the posttest characterization. Since such a sample was not available, the bottom and lower side section of the nozzle sample were used as the reference material (Fig. 22). Sample preparation for the reference material and in-depth material change evaluation consisted of excising transverse sections, polishing and ion etching with xenon. The ion etching procedure was used to aid in definition and interpretation of the matrix structure.[1]

The ENT002 composite macrostructure is shown in Fig. 23. The composite was characterized by macrocracking within the matrix pad between the longitudinal bundles and the adjacent fibers and matrix pockets. From the macrographs, it appears that these cracks form a contiguous network. This material was originally thought to have been processed solely by multiple high pressure (10,000 psi) petroleum pitch procedures. However, the microstructure clearly indicated that a midcycle resin impregnation step had been used. This was apparent from the glass-like material (non-graphitized) present in the large fiber interstices. After discussions with the manufacturer, it was determined that multiple impregnation procedures with different matrix precursors were used. Although processing details were unknown, it was determined that the procedure consisted of from one to two petroleum pitch impregnations under atmospheric pressure, numerous high pressure (<5000 psi) petroleum pitch impregnations, and a midprocess resin impregnation. It must be pointed out that for detailed and accurate posttest evaluations of materials, a complete processing history must be available.

The matrix pocket consisted mainly of a porous nongraphitized resin material (Fig. 24). Matrix cracking and the closed-pore structure were

[1] J. E. Zimmer, J. L. White, J. S. Evangelides, and R. A. Meyer, Carbon Nose Tip Materials Technology: Volume 1, Microstructure and Fracture of Carbon Materials, TOR-0076(6726-02)-2, The Aerospace Corporation, El Segundo, California (September 1975).

METALLOGRAPH SECTIONS

GAS FLOW

FLAMEFRONT SURFACE
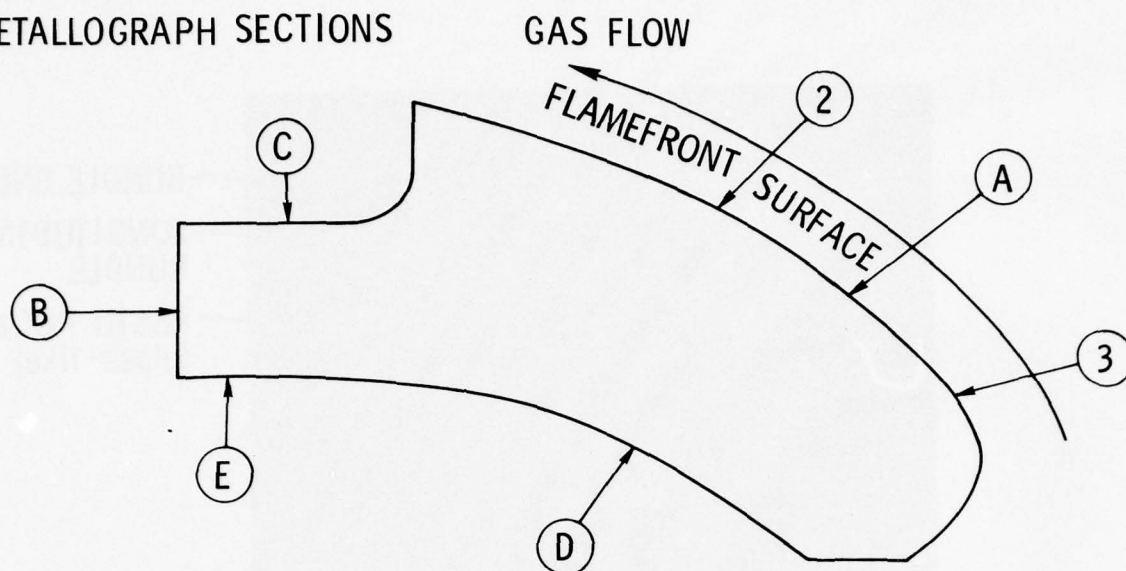
SEM SURFACES
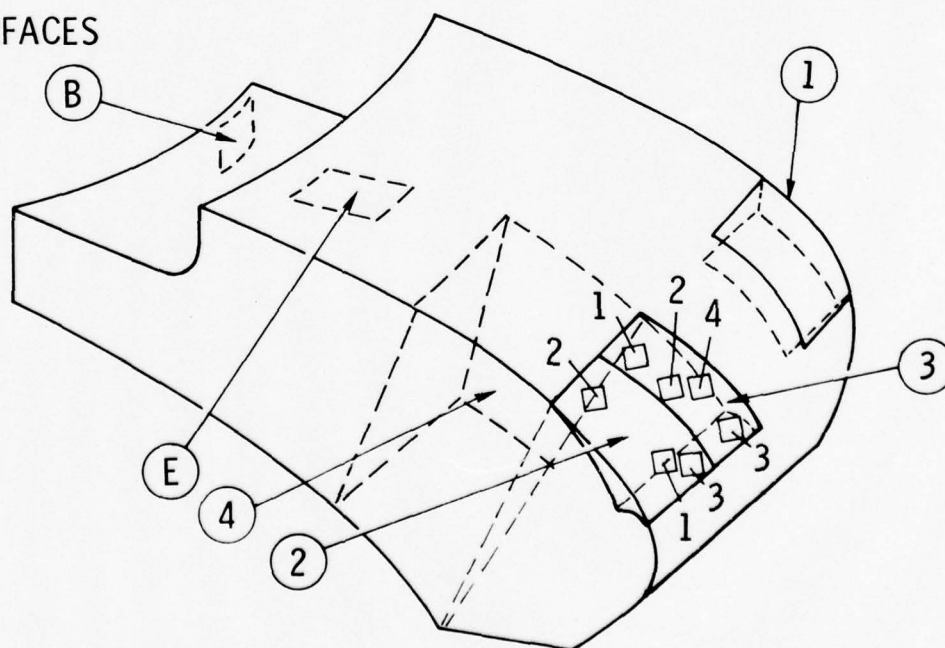
Figure 22. Photomicrograph Locations, Entrance SN002

-33-

BUNDLE END
LONGITUDINAL BUNDLE
RESIN POCKET (glass-like)

500 μm
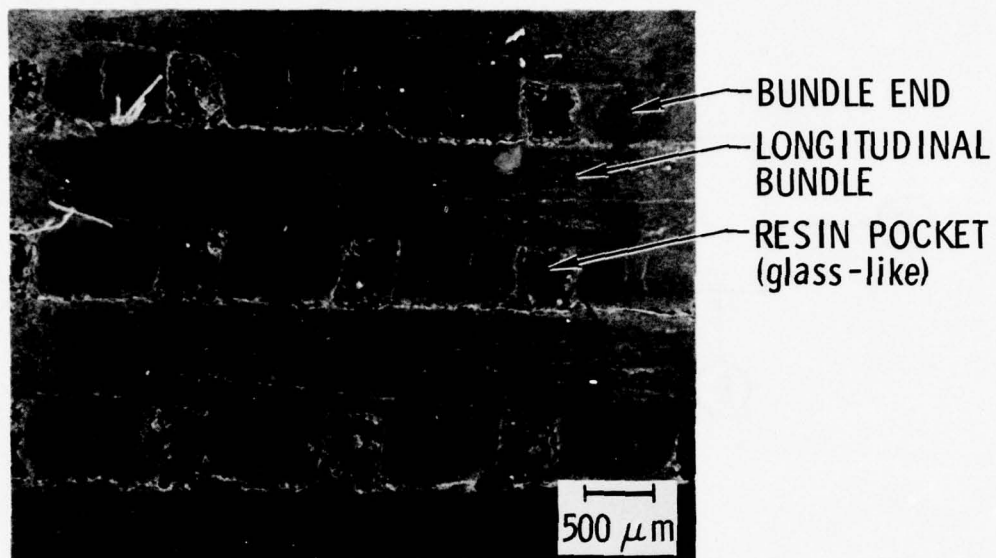
Figure 23. Micrograph of Composite ENT 002

GRAPHITIZED
RESIN

NON-
GRAPHITIZED
RESIN

THORNEL 50
FILAMENT

GRAPHITIZED
RESIN

200 μm

100 μm

4 μm
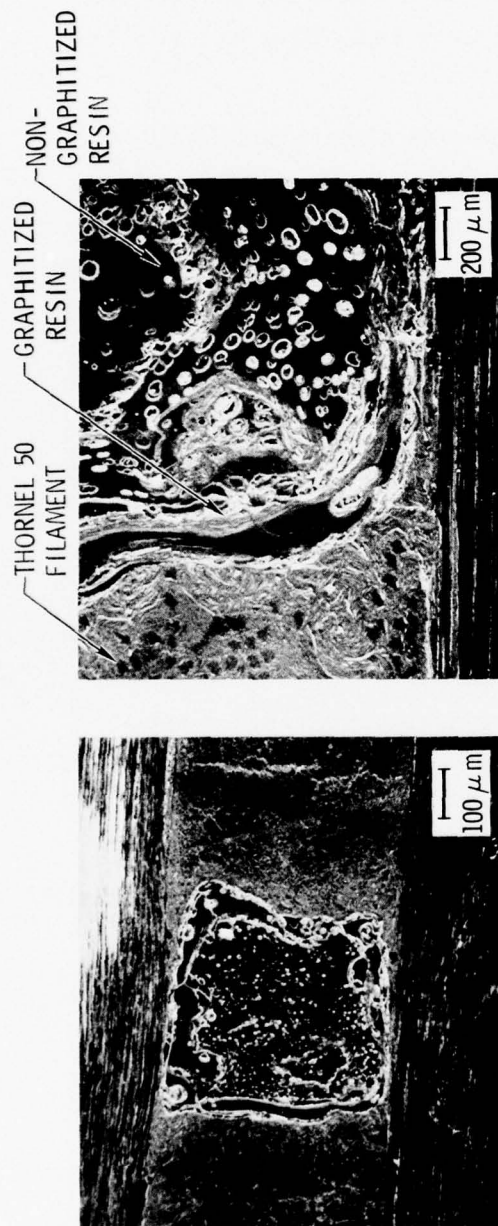
Figure 24. Scanning Electron Micrographs of Reference Material ENT 002

-35-

quite apparent. A portion of the resin material did graphitize, as indicated in the figure. The matrix flow lines or lamina were indicative of the graphite basal plane orientation.

The matrix structure within a fiber bundle was almost parallel to the filament surface (Fig. 25), although regions did exist between filaments where a more random orientation existed (Fig. 26). The fish scale matrix appearance was caused by the graphite basal planes intersecting the polished surface at intermediate angles between 0 and 90 deg. The matrix structure within a fiber bundle transverse to the filament axis is shown in Fig. 27.

Since the pretest characterization was accomplished on a backface sample, cross-sectional views were taken of the backface to determine if any damages or changes in material structure were occurring (Fig. 28). Low-magnification views of this region showed the same crack pattern adjacent to longitudinal bundles and the same matrix porosity as in the other sample. However, more detailed higher-magnification views suggested that some damage was present. Of course, it can not be determined whether this occurred during processing and handling or during the test firing. Longitudinal filament, matrix fracture, and matrix cracking within a transverse bundle are shown in Fig. 29. Although the general microstructural characteristics, pores, and graphite orientation were similar, it was not necessarily true for the microcracking. Therefore, it was not obvious that the backface material was representative of pretest material.

Examination of the fired surface showed the typical gouge marks and pores parallel to the gas flow. Generally, gross macrocracks surrounded the fiber bundles as shown in Fig. 30. Upon cooling, portions of the nozzle material appeared to be coated with redeposited carbon. Detailed microstructural views from areas A-D of Section 2 indicated that the entire surface was coated (Fig. 31). Figure 32 is a cross-sectional view through a coated region of this specimen. This masked the actual fired surface and prohibited further analyses of this specimen. However, specimen 4, which was adjacent to specimen 2, was uncoated.

FILAMENT

PITCH
MATRIX

5 µm
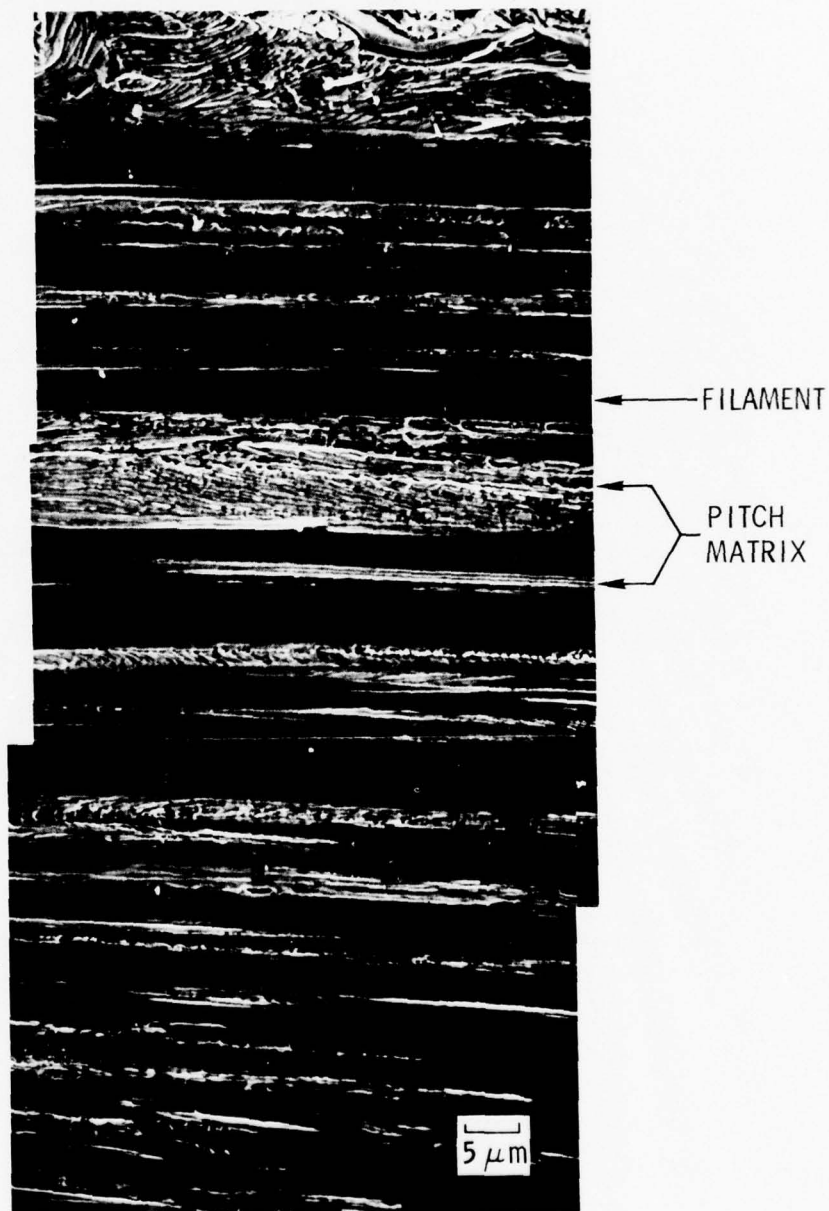
Figure 25.   Scanning Electron Micrographs of Matrix
Structure Within a Fiber Bundle of ENT 002

GRAPHITE BASAL PLANES NORMAL TO SURFACE

"FISH SCALE" - GRAPHITE BASAL PLANES AT INTERMEDIATE ANGLE TO SURFACE

4 μm
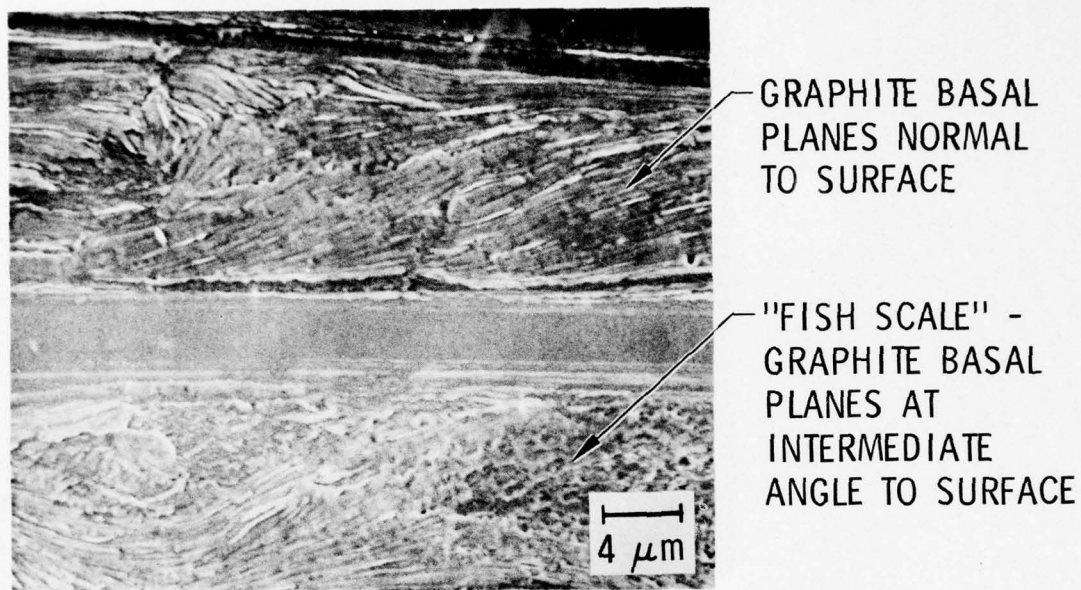
Figure 26. Scanning Electron Micrograph of Matrix Structure in ENT 002
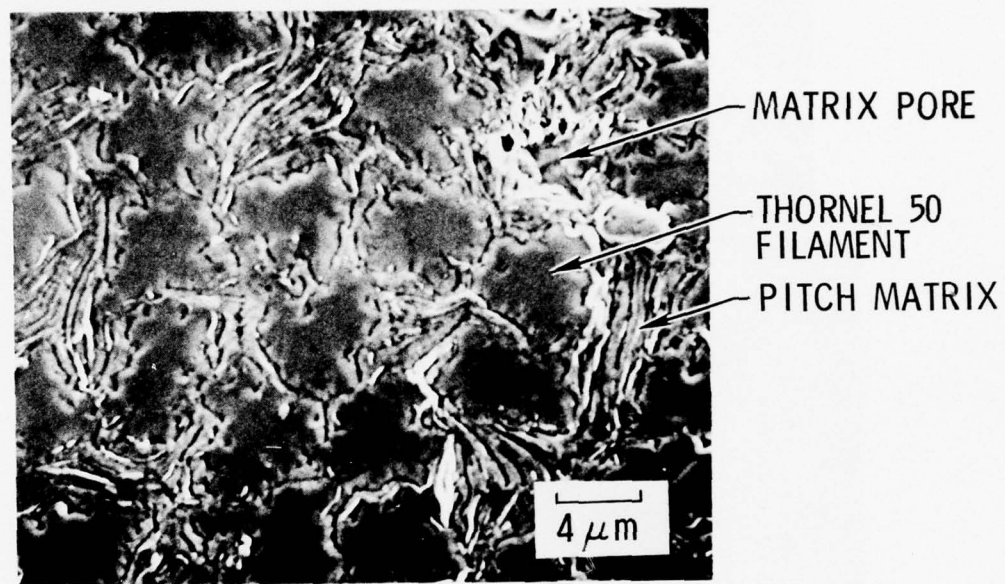
Figure 27. Scanning Electron Micrograph of ENT 002
Transverse to Filament Axis

Figure 28. Scanning Electron Micrographs of Back
Face Material in Cross Section
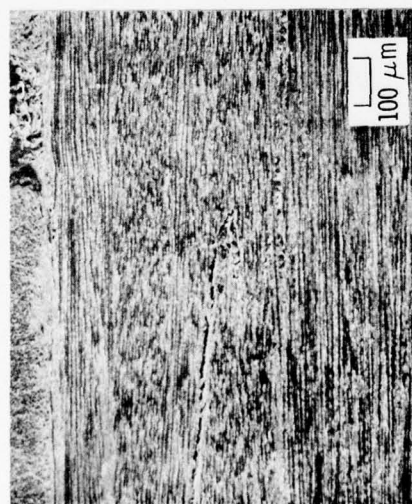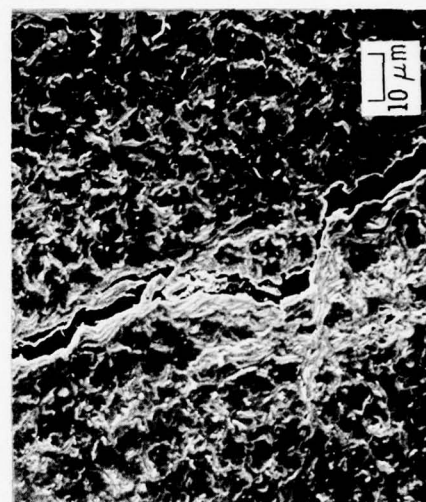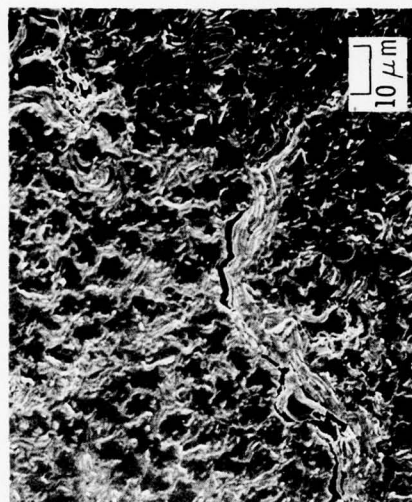
Figure 29. Scanning Electron Micrographs of Filament and Matrix Region in Back Face Region
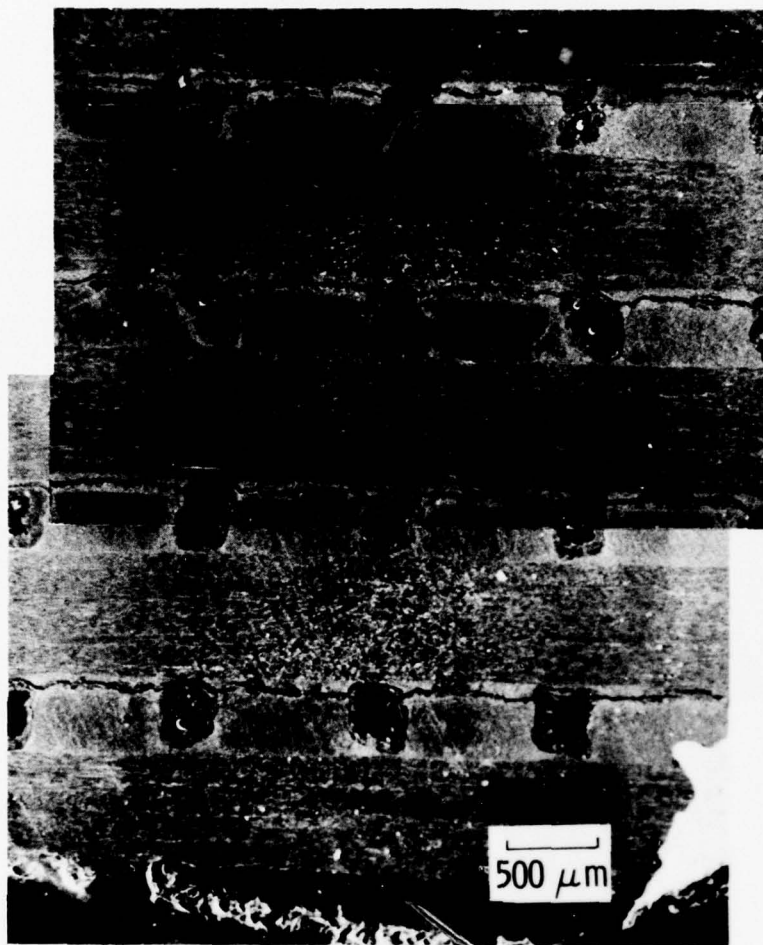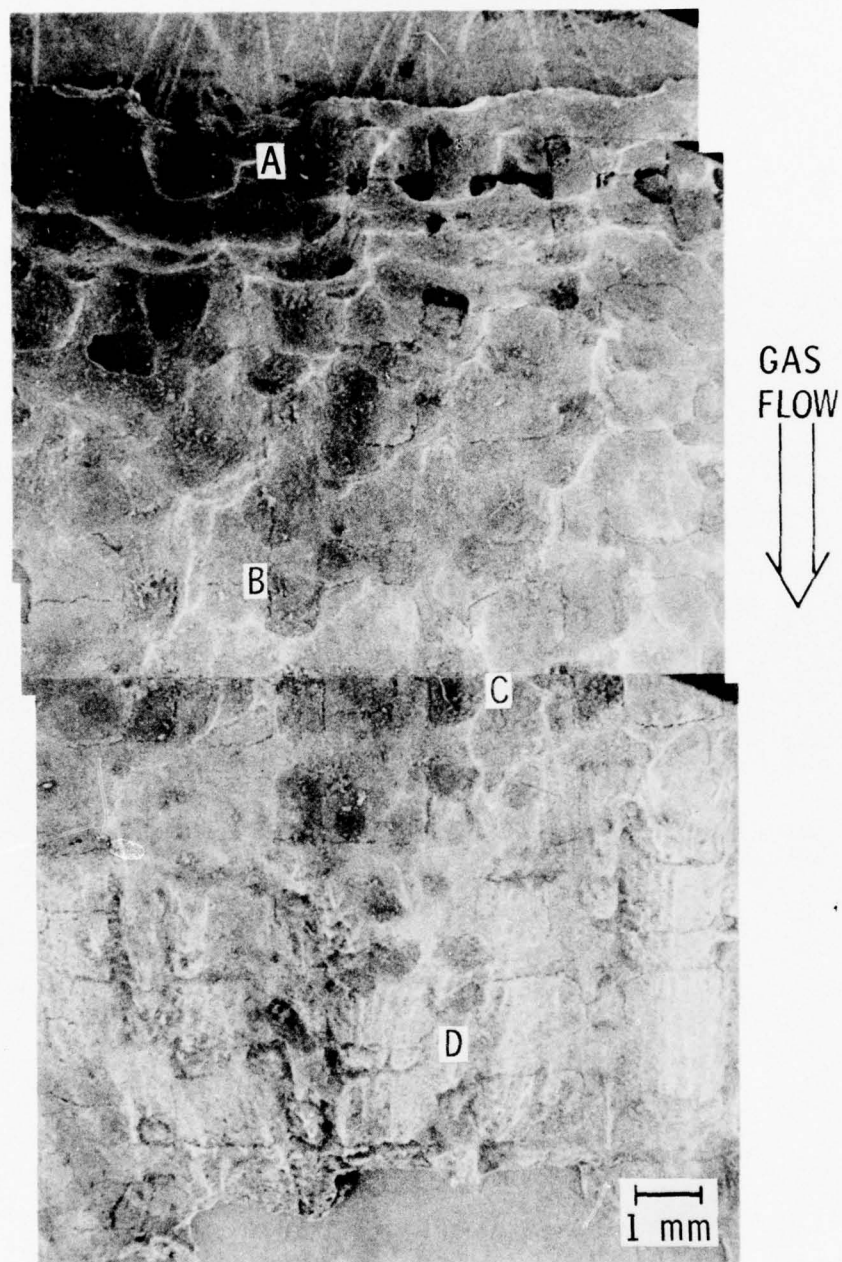
Figure 30. Scanning Electron Micrographs of
ENT 002 Sample No. 2
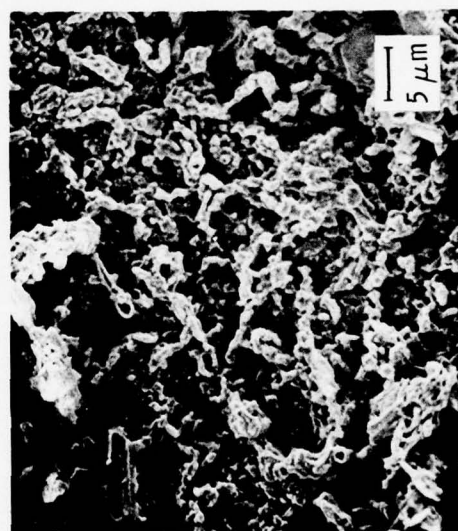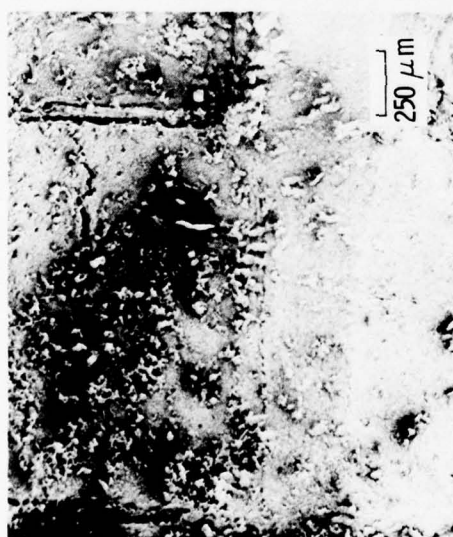
Figure 31. Scanning Electron Micrographs of Section 2 of ENT 002
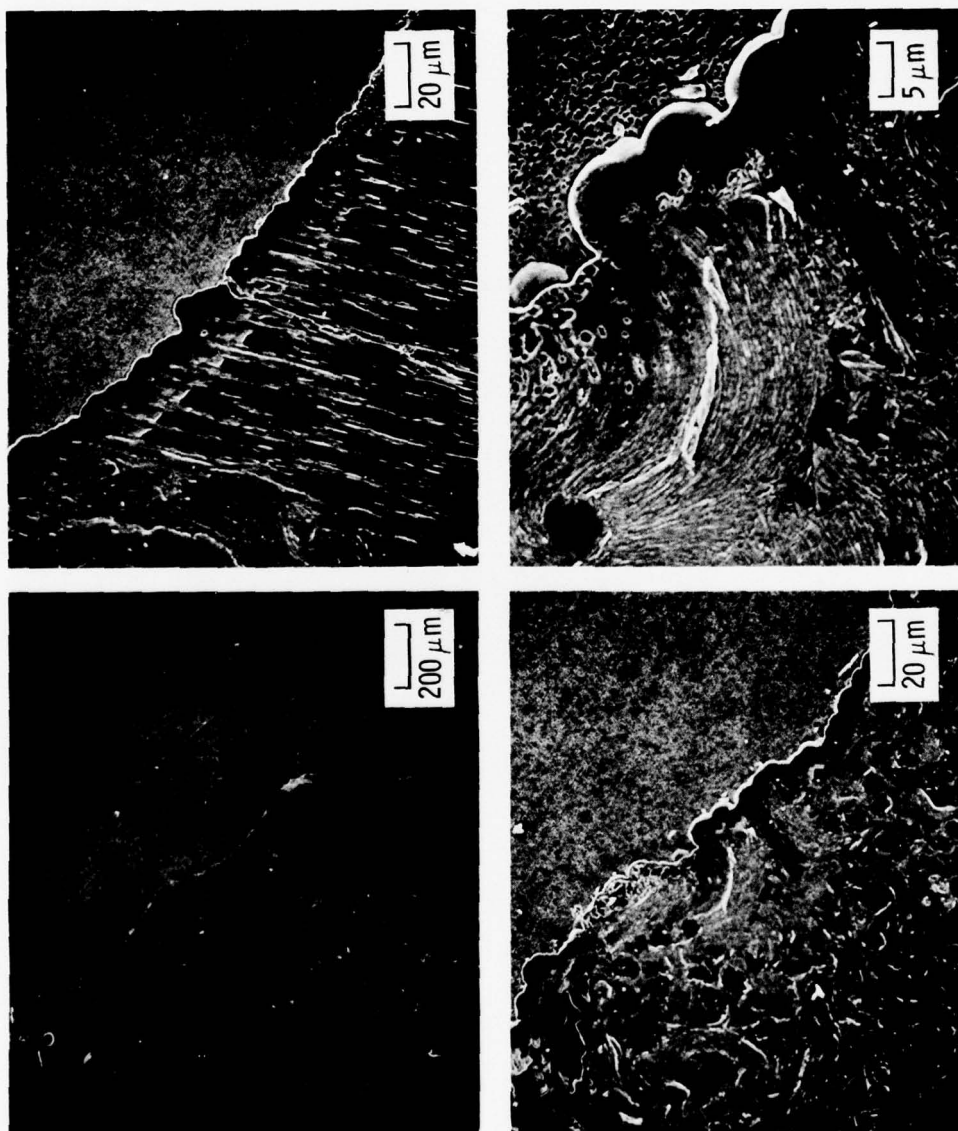
Figure 32. Scanning Electron Micrographs of Coated Surface in Cross Section

-44-

In order to characterize the response of the composite surface to the rocket nozzle environment, filament ends, filament sides, and bulk matrix areas were examined. To the right of the crack in location A of Fig. 33 is a region where the filament ends were oriented normal to the surface and the gas flow; to the left of the crack, the filaments intersected the surface and gas flow at an acute angle. In both cases, the filament ends were below the matrix. Recall that the matrix was aligned with the graphite basal planes parallel to the filament surface. This sheath structure can be seen to exist above the filament ends in Fig. 34. In addition, the filament ends appear flatter than the tapered sheath ends, suggesting either uniform filament mass loss or mechanical fracturing of filaments, or both. The flat filament surface indicates that mechanical fracturing may have occurred. The depth of eroded or affected material appeared greater when the filament ends were oriented at the acute angle of Fig. 31 (a) and (b). A clearer view of the different filament and matrix heights is shown in the higher magnification micrographs of Fig. 35.

The filaments that were parallel to the fired surface had a slightly more uniform appearance (Fig. 36). An example of longitudinal filament tensile fracture was also found. The orientation of this fiber bundle with respect to gas flow is shown for area B in Fig. 33.

The characteristics of a bulk matrix pocket after firing depended on the type and number of irregularities, e.g., pores or broken filaments and the degree of preferred orientation (Fig. 37). The fired appearance of a uniform glassy structure with a large pore is shown in Fig. 37(b). The lower left corner of this micrograph is representative of a region with a collection of small pores. A large concentration of pores in the glassy carbon matrix resulted in a much more irregular appearance. In addition to the characteristic dried bed pattern, this structure had developed into more conical shapes. Shown in Fig. 38 is a higher magnification view of the bed pattern and a porous conical region. At the time this photo was taken, several closed pores were being etched opened. The characteristic

-45-
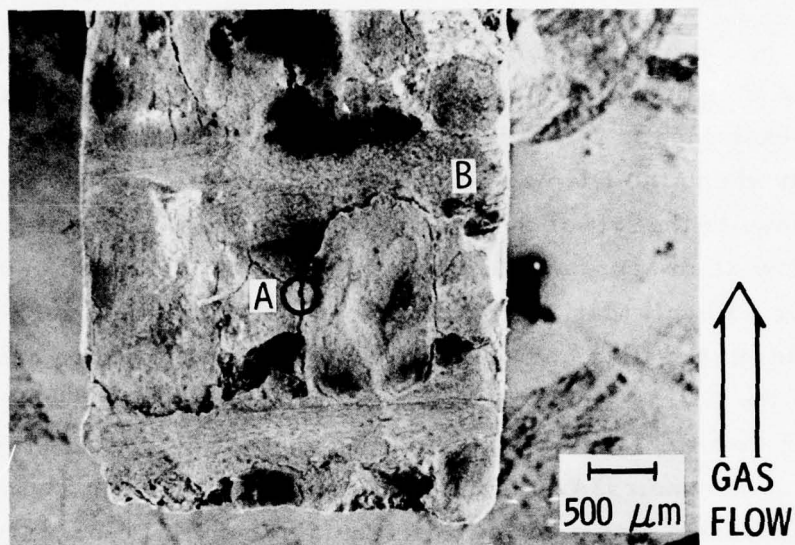
Figure 33. Scanning Electron Micrograph of Specimen 4 Location 1

FILAMENT ─── MATRIX

(a)

MATRIX
FILAMENT
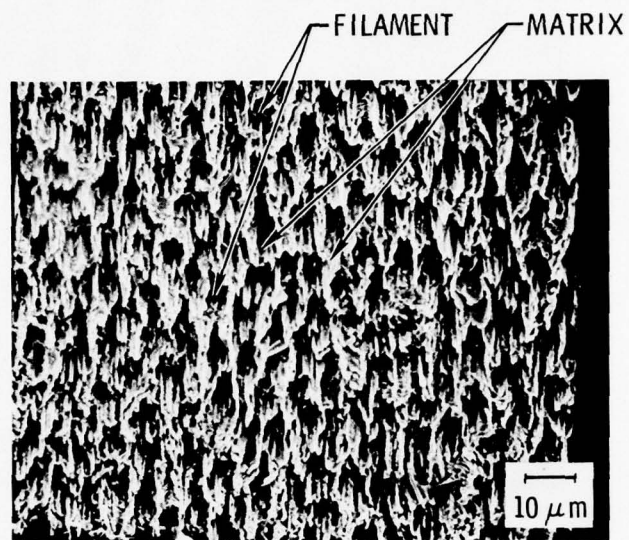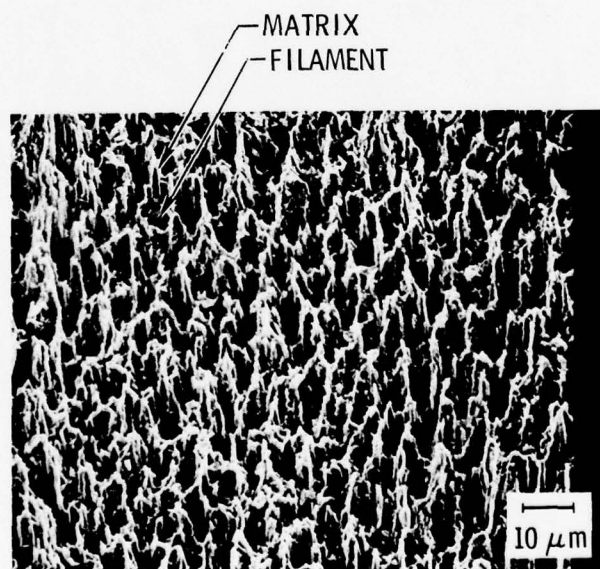
(b)

Figure 34. Scanning Electron Micrographs of Filament Ends
at Acute Angle (a) and Normal Angle (b)
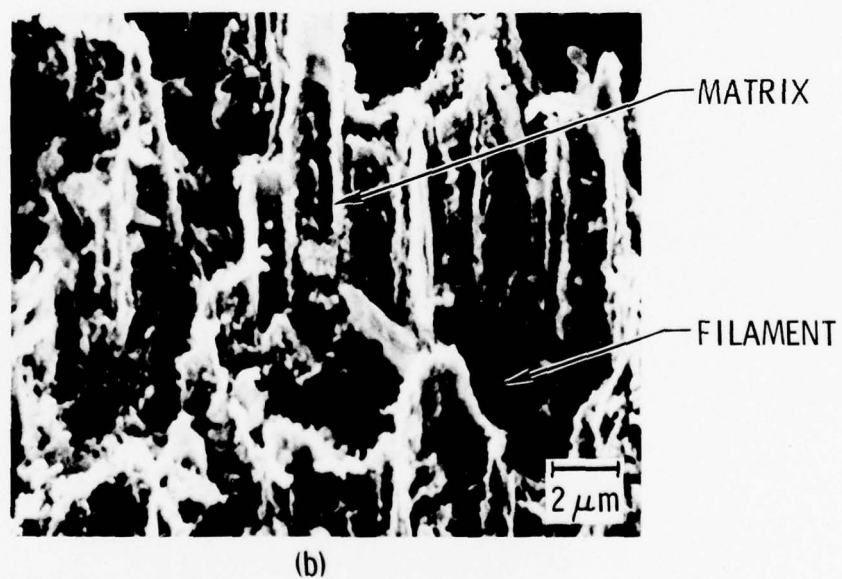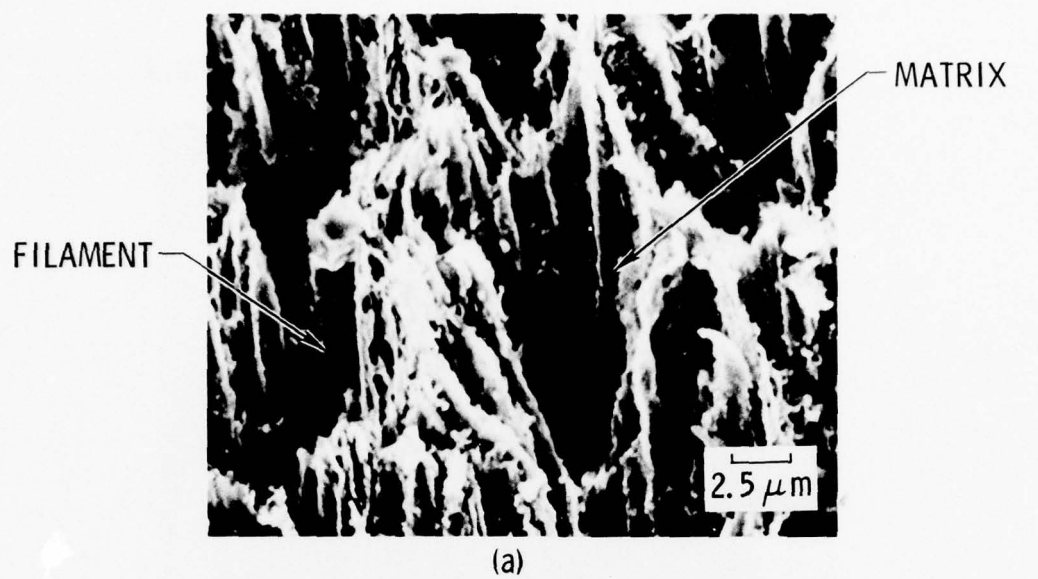
Figure 35. Scanning Electron Micrographs of Filament Ends at Acute Angle (a) and Normal Angle (b)
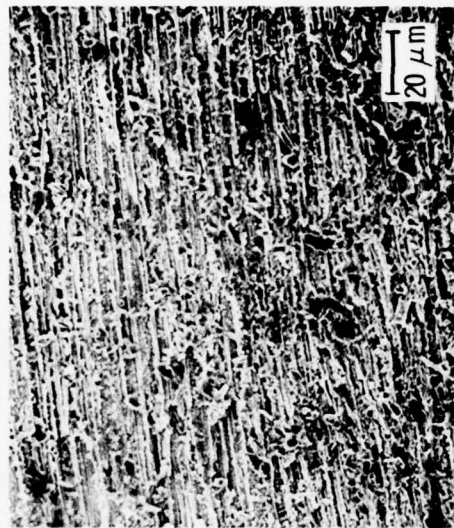
Figure 36. Scanning Electron Micrographs of Longitudinal Fiber Parallel to Fired Surface
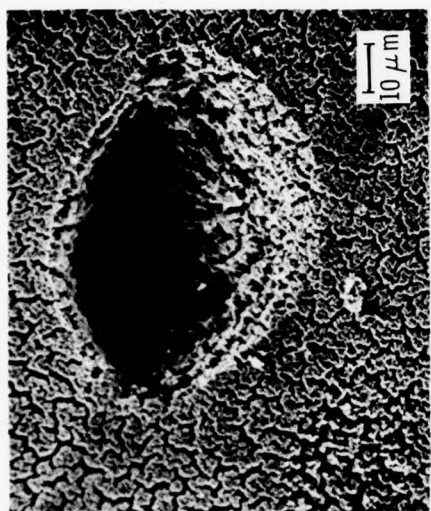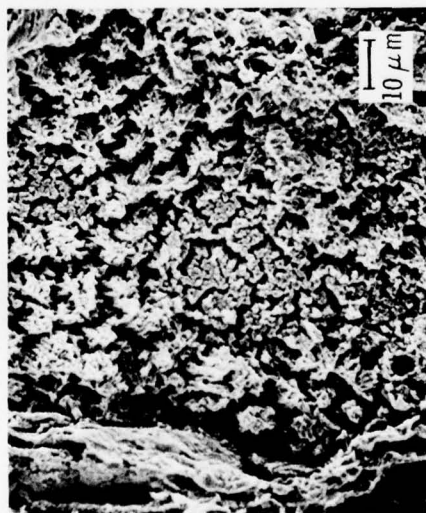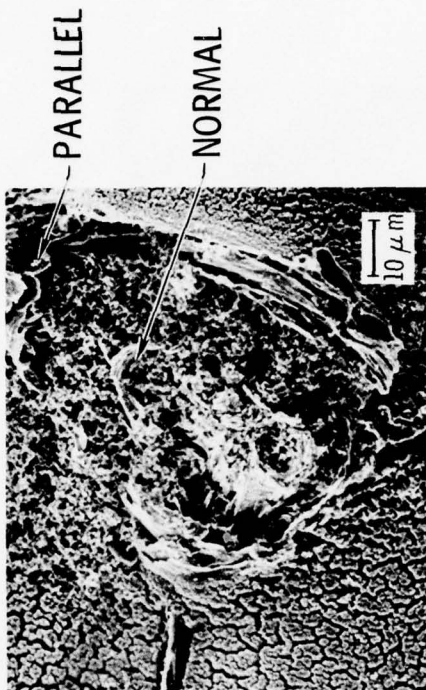
Figure 37. Scanning Electron Micrographs of Bulk Matrix Packet
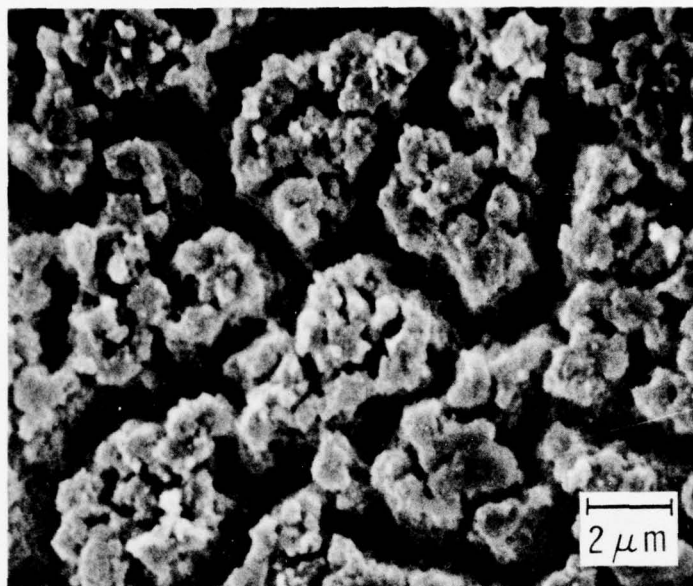
(a) BED PATTERN
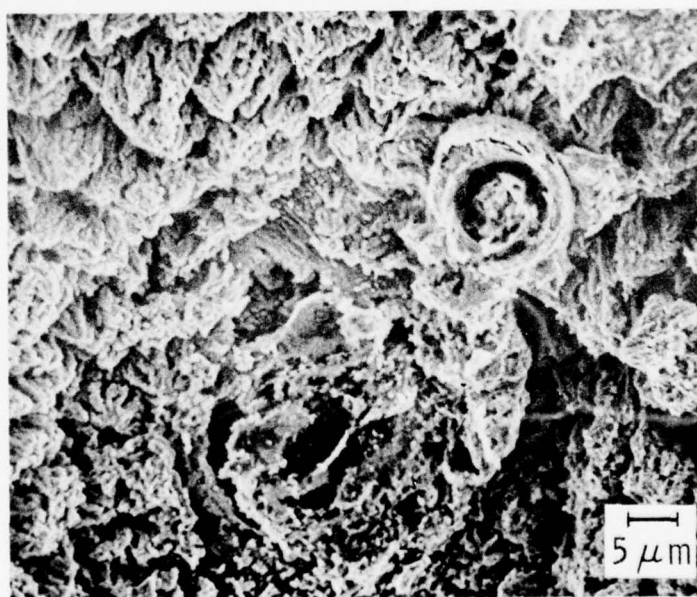
(b) CONICAL PATTERN

Figure 38. Scanning Electron Micrographs of Bulk
Matrix Response Patterns

-51-

response of the bulk matrix with debris (broken filaments) and a more graphitic structure is shown in Fig. 37(d). The aligned graphitic basal planes are seen at various angles to the plane of view, as indicated in the figure.

The depth to which these material changes occurred was determined by taking a cross section of the fired sample (Fig. 39). The continuous array of macrocracks parallel to the fiber bundles is apparent. A portion of a transverse bundle remains just above a bulk matrix pocket (indicated by the arrow). A slightly higher magnification view indicates that it is ready to be mechanically removed (Fig. 40).

As in the surface analyses, the fiber ends that were perpendicular to the fired surface appeared to suffer less material degradation than those at an acute angle. This damage is shown in Figs. 40 and 41, where ion etching allows easy identification of degraded material. A rough estimate of this distance for these two cases is 18 μm (range: 13 to 34 μm) for normal orientation and 39 μm (range: 27 to 54 μm) for acute orientation. A more detailed view of the type of degradation occurring in the two fiber ends is shown in Fig. 42. Longitudinal cracks within the fibers are seen to progress to a depth of 800 μm in Fig. 41.

Fibers parallel to the fired surface showed essentially surface effects (Fig. 43). The initiation of microcracks between filaments beneath the surface is the mechanism whereby the mechanical removal of filaments occurs. This cracking was taking place in the top two filaments of Fig. 43(b). A complete separation of a single filament from the bundle had taken place at the edge of the bundle. Excluding the depth of microcrack generation, material changes occurred to depths of approximately 7 μm (range: 1-14 μm).

The porosity and cracking within the bulk matrix pockets, particularly at regions where the material had become oriented, provided weak points for material loss (Fig. 44). The weak graphitic planes allow macrocracks
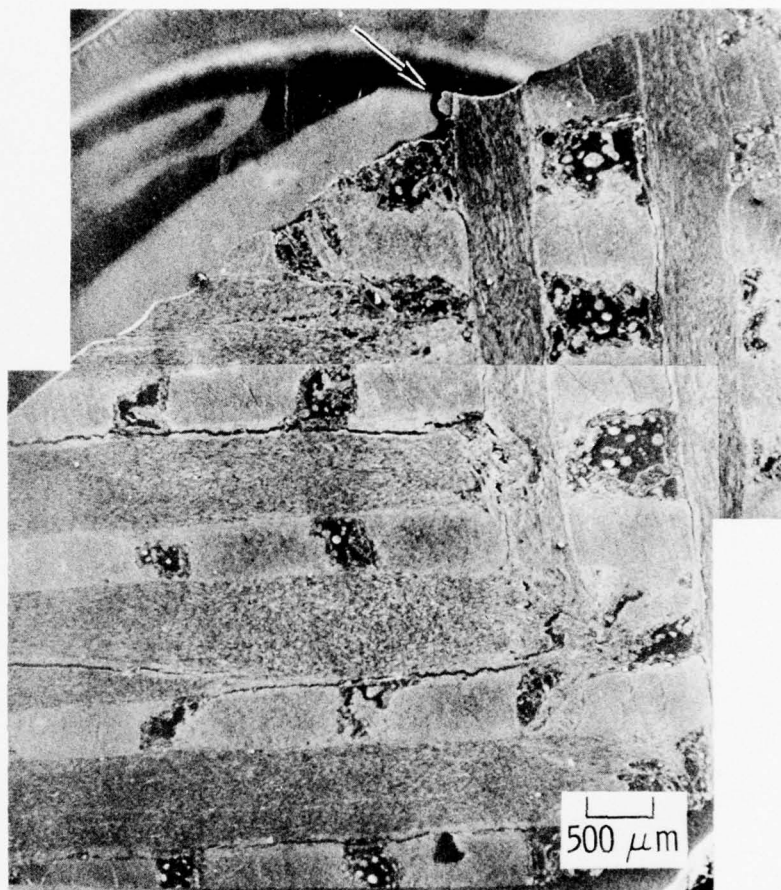
Figure 39. Scanning Electron Micrographs of ENT 002 Cross Section
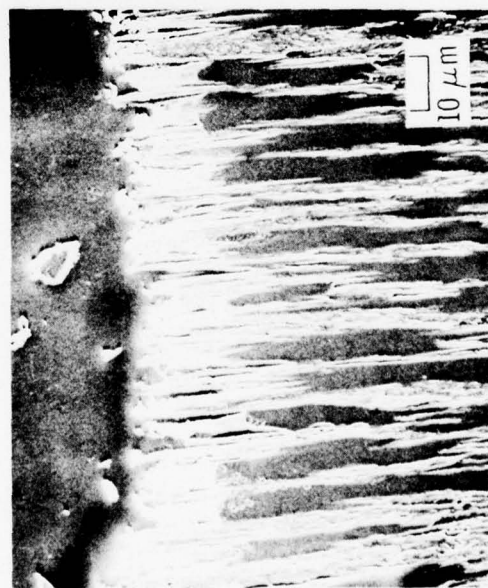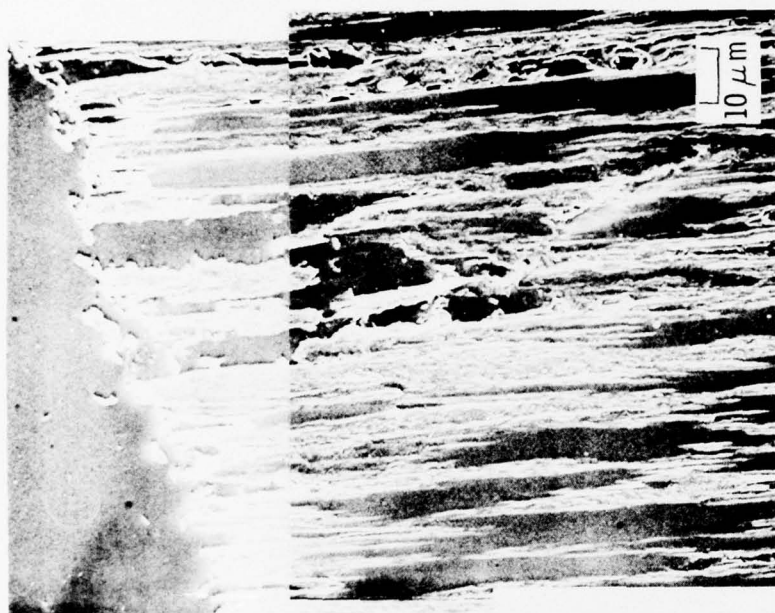
Figure 40. Scanning Electron Micrographs of Fiber Ends Normal to Fired Surface
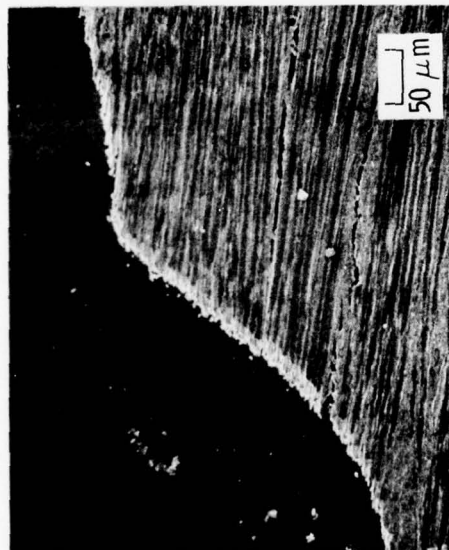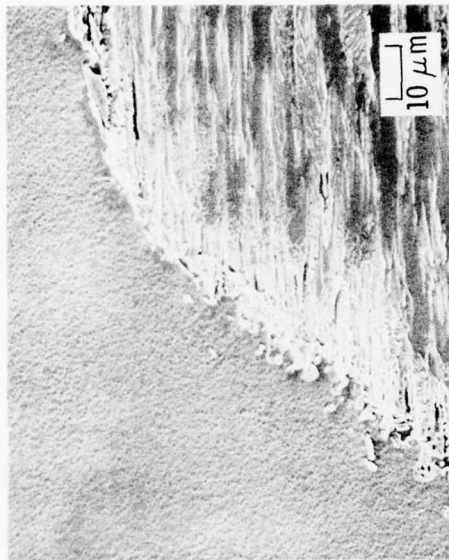
Figure 41. Scanning Electron Micrographs of Fiber Ends at an Acute Angle to Fired Surface

Figure 42. Scanning Electron Micrographs of Fiber Ends with Typical
Filament-Matrix Degradation Shown
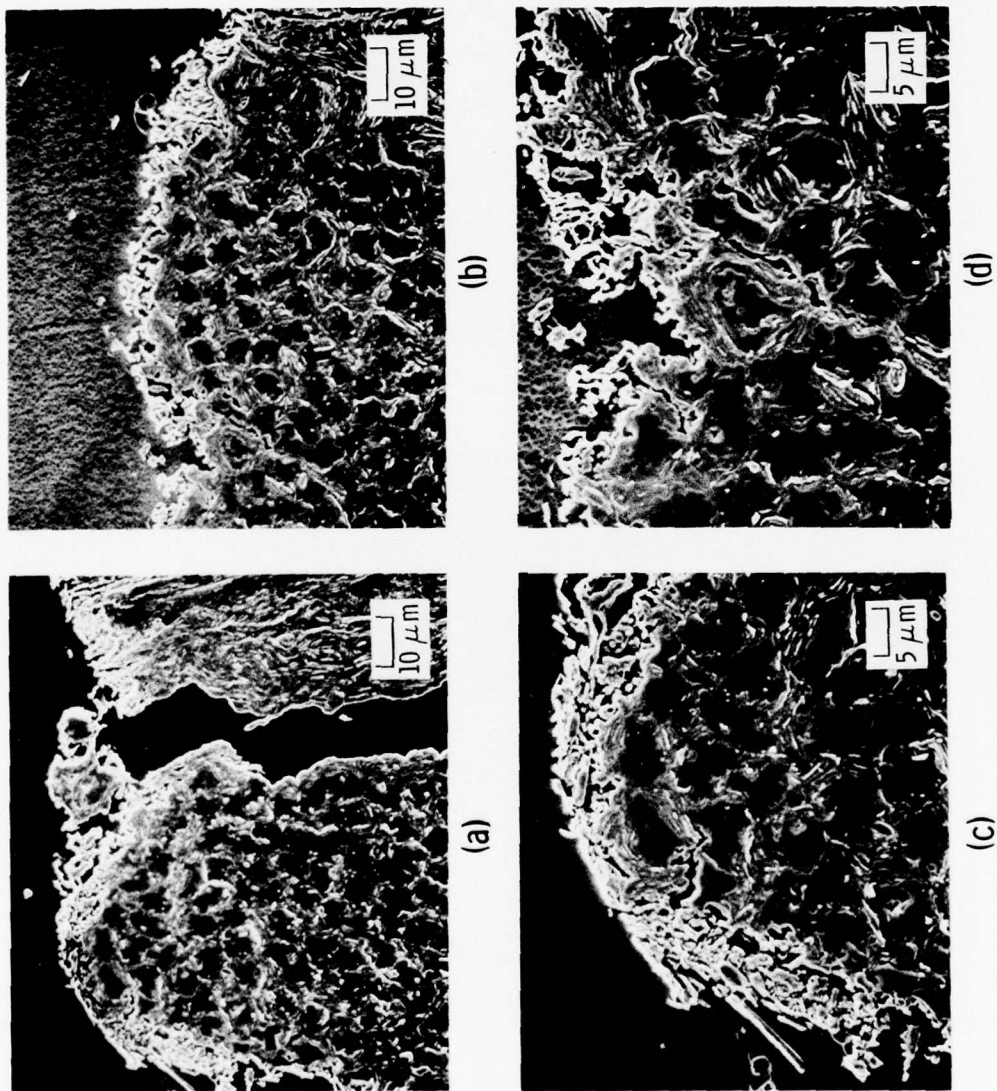
Figure 43.   Scanning Electron Micrographs of Fiber Bundle Parallel to Fired Surface
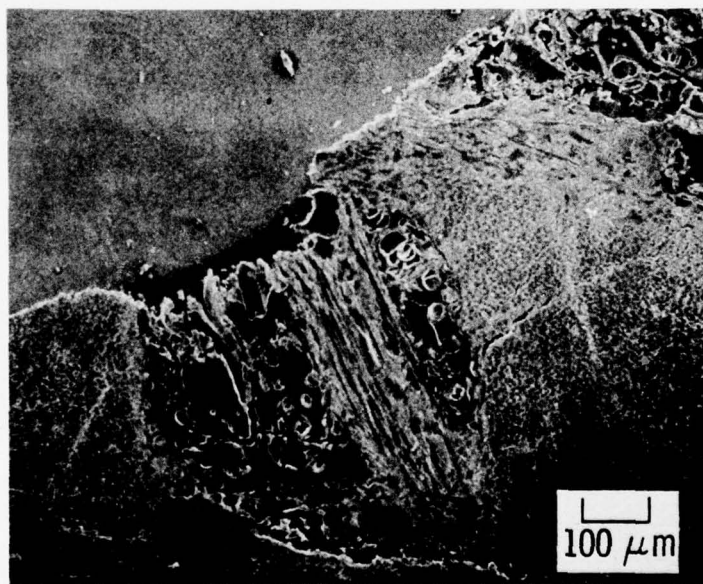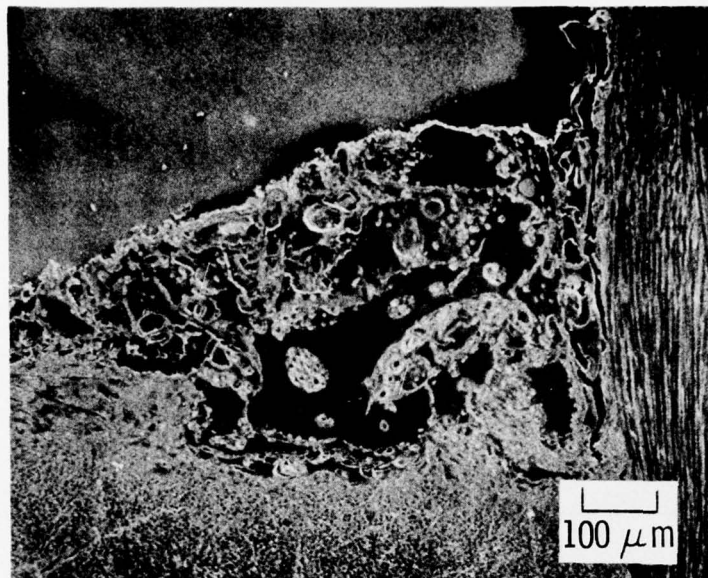
Figure 44. Scanning Electron Micrographs of Bulk Matrix Pocket

to develop, which frees large portions of the glassy carbon material to a depth of 350 µm. The characteristic bed and conical patterns that were observed on the fired surface are shown in cross sections in Fig. 45. The depth of degraded material on the glassy carbon matrix was from 4 to 9 µm. The development of microporosity within the degraded material and opening of closed microporosity in the glassy carbon are shown in Fig. 45(b). The rough cross-sectional appearance of regions containing large amounts of closed porosity and partial graphitic orientation was consistent with fired surface characteristics. These conditions are consistent with observations of tested reentry nose tips; of course the degradation mechanisms differ.

b. Crack Propagation

Thermal stresses in the radial direction on the nozzle material can cause microcrack formation; an exposure to the motor environment can result in aggravated erosion or mechanical removal of the weakened section. Previous research on the tensile behavior of carbon-carbon composites has shown that microcracks generated under stress can close upon unloading and become undetectable. In order to examine the feasibility of observing the difference in microcrack formation between pretest and posttest material, exploratory crack propagation tests were conducted in the SEM by bonding a test specimen to an aluminum substrate and loading in flexure (Fig. 46). Also show is the method for excising specimens from the nozzle sample. The top triangular piece represented the fired specimen, whereas the bottom rectangular piece was used for the pretest reference material. Three tests were conducted, one reference and two posttests.

A macrograph of the reference material prior to loading is shown in Fig. 47. Upon loading, the reference sample fractured parallel to the matrix lamina adjacent to the filaments (Fig. 48). This was typical of other crack propagation tests where the weak graphite basal planes were the first to fracture.[2] Note that the failures were not at the filament-matrix interfaces but within the matrix.

[2] J. Jortner and F.I. Clayton, Carbon-Carbon Microstructure: Causes and Effects on Nosetip Ablation, Report MDC No. G6390, McDonnell Douglas Astronautics Company (April 1976).

-59-
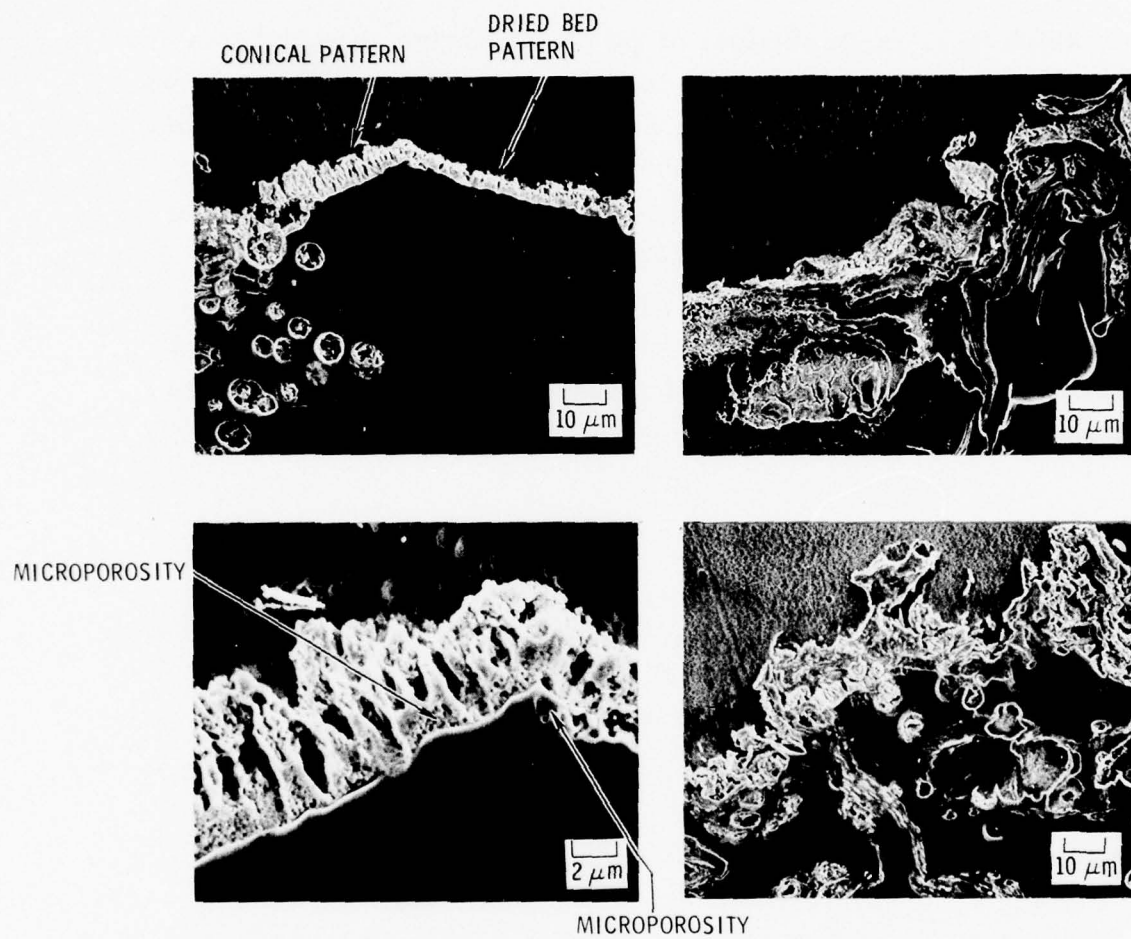
Figure 45.   Scanning Electron Micrographs of Bulk Matrix
Pocket in Cross Section
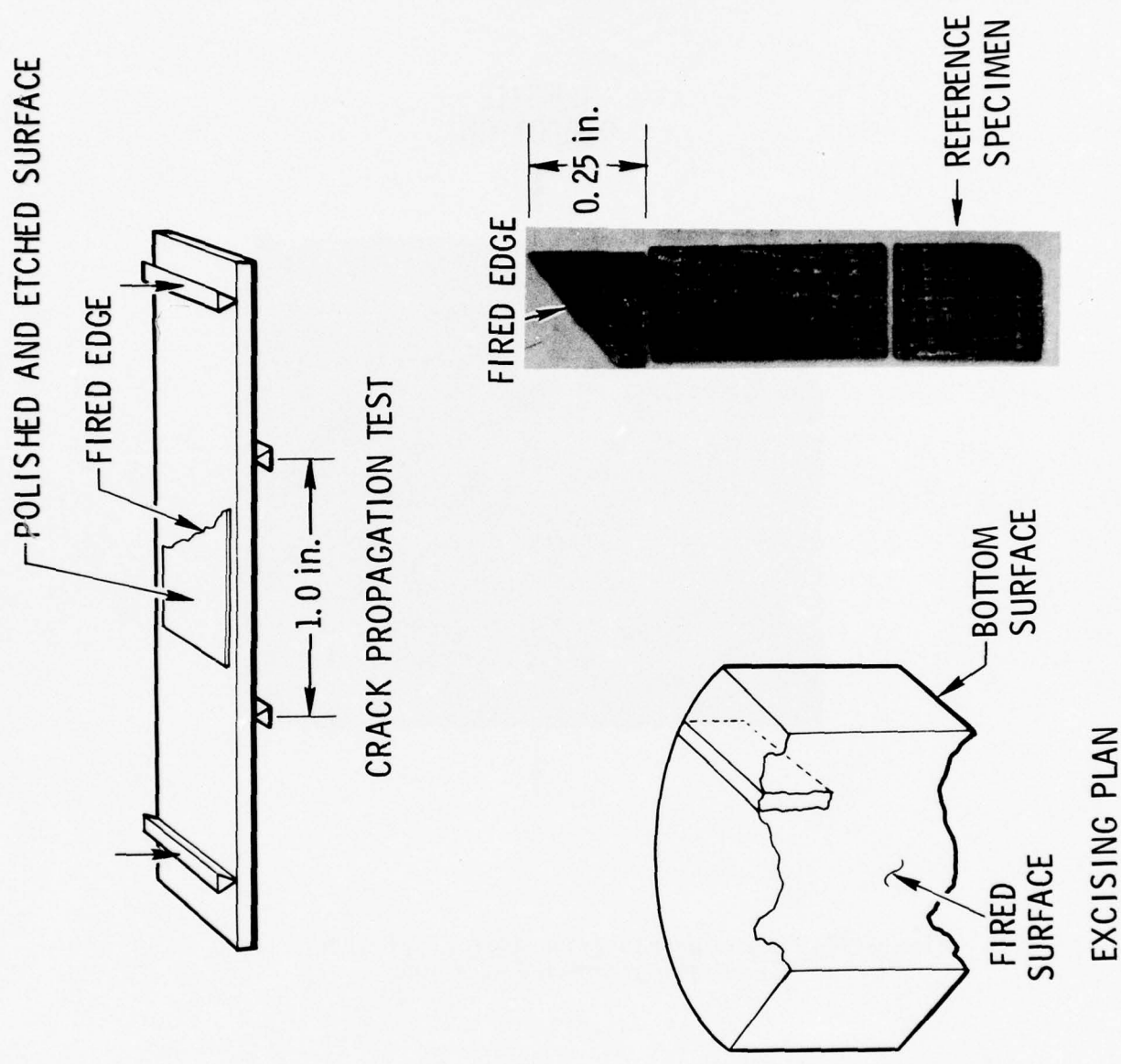
Figure 46. Schematic of Excising Plan and Crack Propagation Test

TENSILE
DIRECTION

500 μm
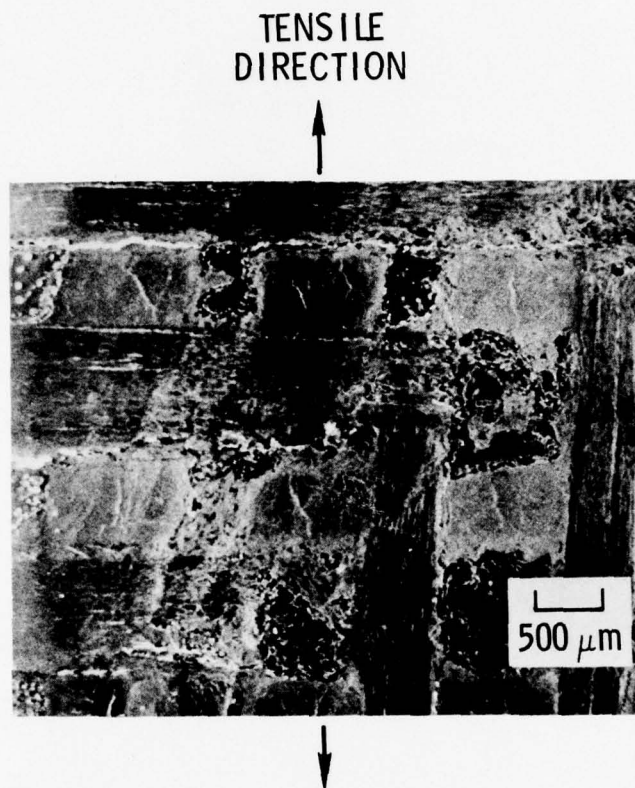
Figure 47. Scanning Electron Micrograph of Specimen
Crack Propagation Reference
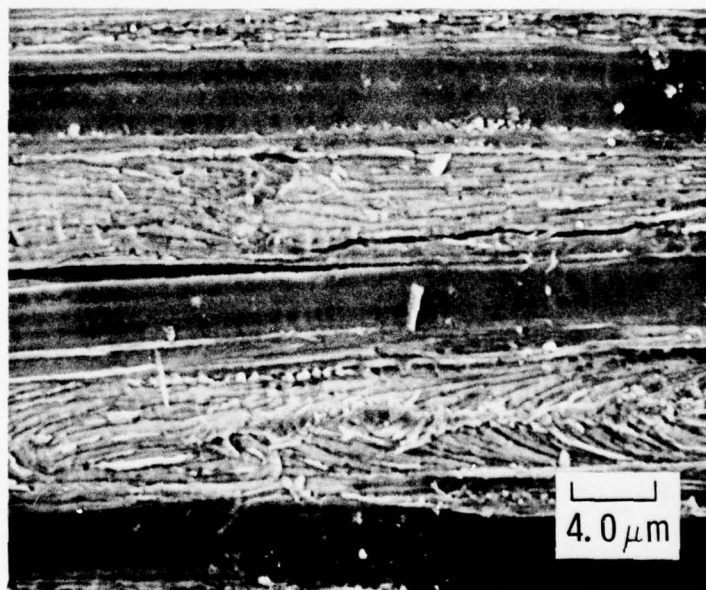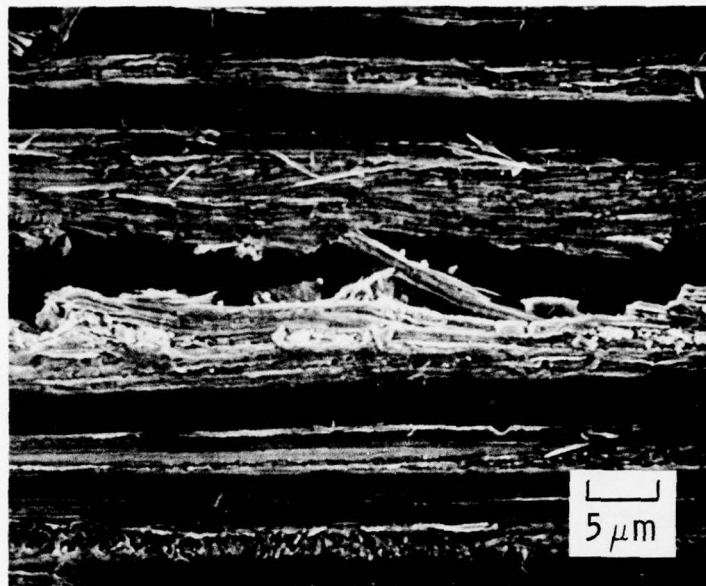
Figure 48. Scanning Electron Micrographs of Matrix Fracture
in Crack Propagation Reference Specimen

Crack propagation in the fired sample was initiated by macrocrack generation parallel to the fiber bundles (Fig. 49). This crack propagated a considerable distance into the specimen, traversing a number of fiber bundles and matrix pockets (Fig. 50); the failure, again, was within the matrix phase. The cracks occur principally at the edge of the fiber bundles, although, in the reference specimen, cracks were generated both at the edges and within the fiber bundle. Even though a limited number of specimens have been tested, the results indicate that the rocket motor environment degraded the matrix material at the edges of the fiber bundles such that this became the point of easy fracture. This supports the microstructural observation of material degradation.

3.   THROAT SUPPORT SN001 – AG CARB 5451 FLAT
      LAMINATE

The erosion of both throat support sections was anomalous in appearance. The metallograph and SEM photomicrographs were taken in locations where this condition could be evaluated. Figure 51 depicts the various areas of throat supports SN001 and SN002 that were subjected to examination. The general nature of the unusual erosion pattern is perhaps best illustrated by Fig. 52. This figure is a reference photograph of the polished cross section of throat support SN001. It shows the repetitive axial sawtooth pattern of the eroded surface section. Figures 53 and 54 are magnified metallograph sections taken at an angle slightly off cross-polarized lighting conditions. Figure 55, taken at area B, shows the basic basket weave pattern of the structure as viewed in a line normal to the lamina. Figure 53 illustrates the detail of the structure at the surface (area 2, Fig. 51). Figure 54 shows the in-depth structure (area 1).

Because of the nature of the lighting, it was concluded that the structure of the reinforcement at the tops of the teeth, or regions of least material mass removal, is predominantly cloth. This cloth is oriented with the warp/fill direction in a right-angle configuration. However, the orientation at the grooves is nearly 45 deg. The initial reaction is to assume that the

FIRED SURFACE

400 μm
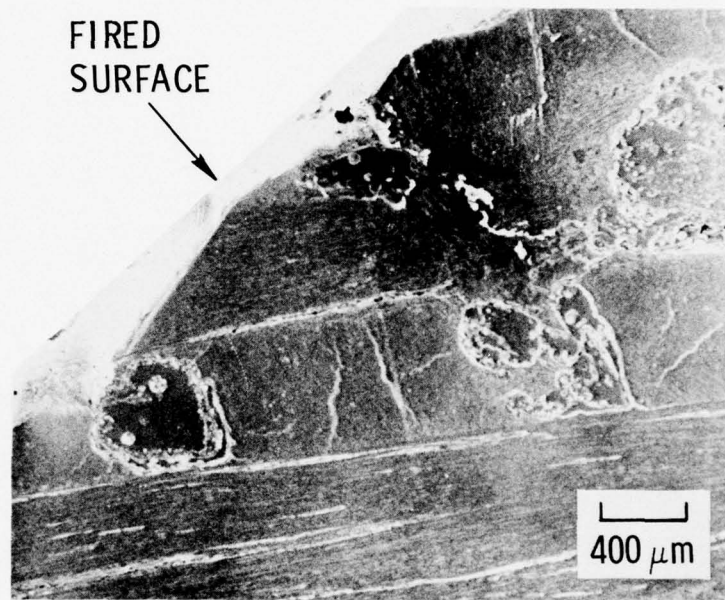
Figure 49. Scanning Electron Micrograph of Fired Specimen Under Load
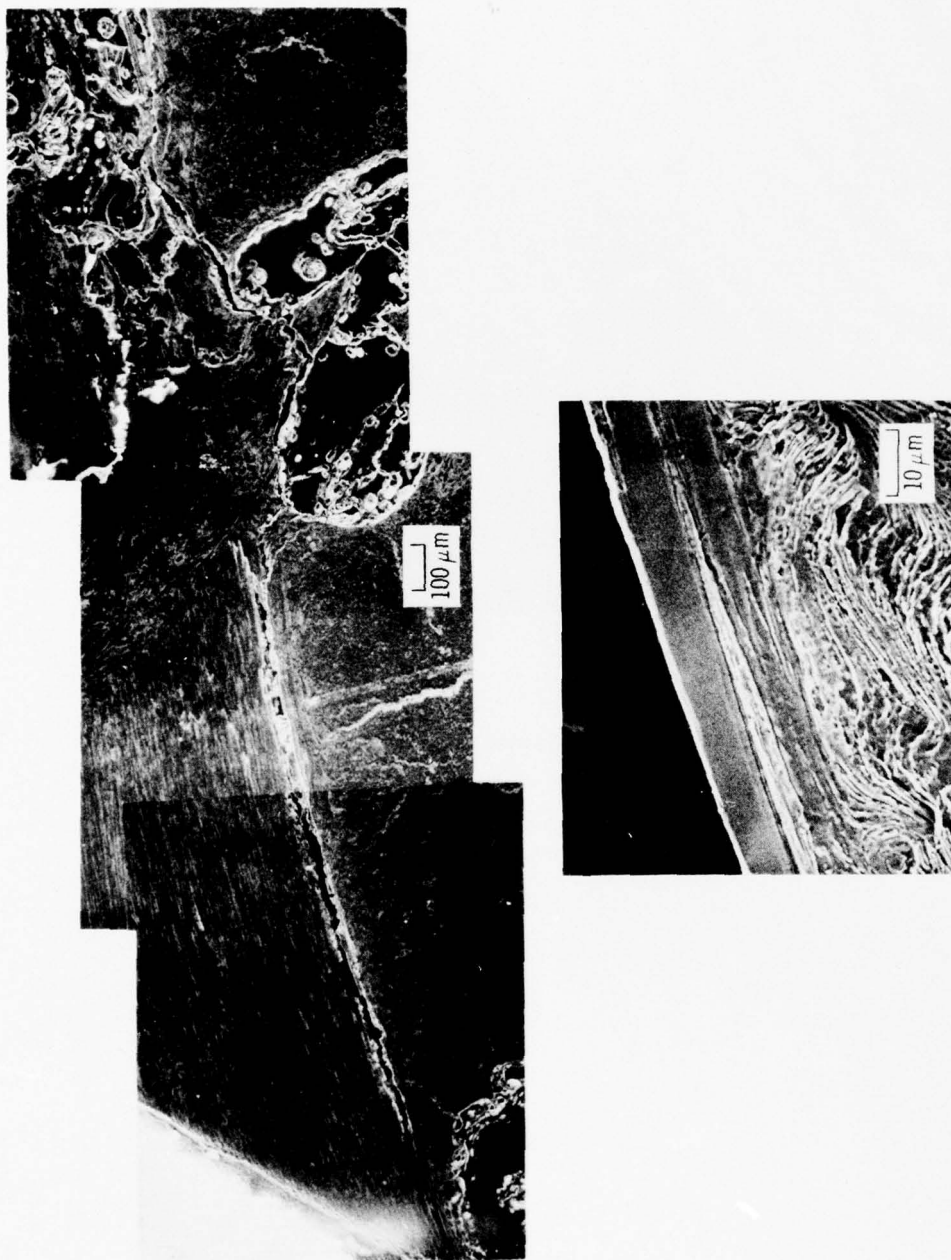
Figure 50. Scanning Electron Micrographs of Crack Generation in Fired Specimen

METALLOGRAPH SECTIONS

FLAMEFRONT SURFACE

GAS FLOW

B

3

1

2

SEM SURFACES

1

2

3

B

A
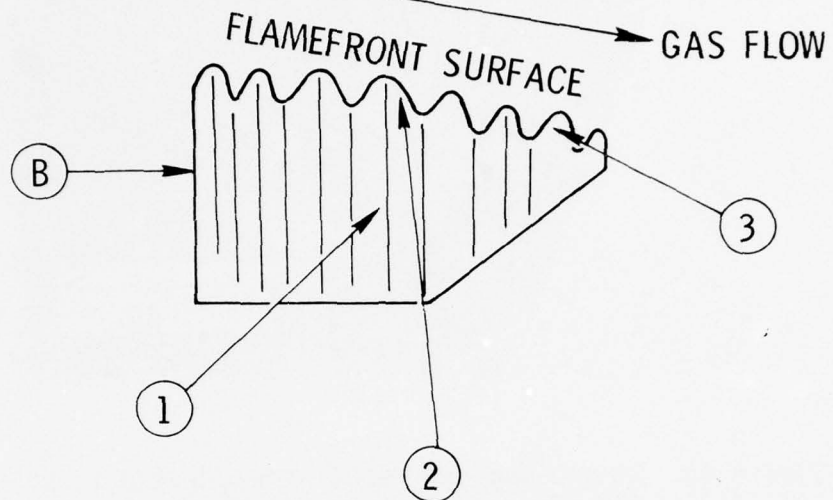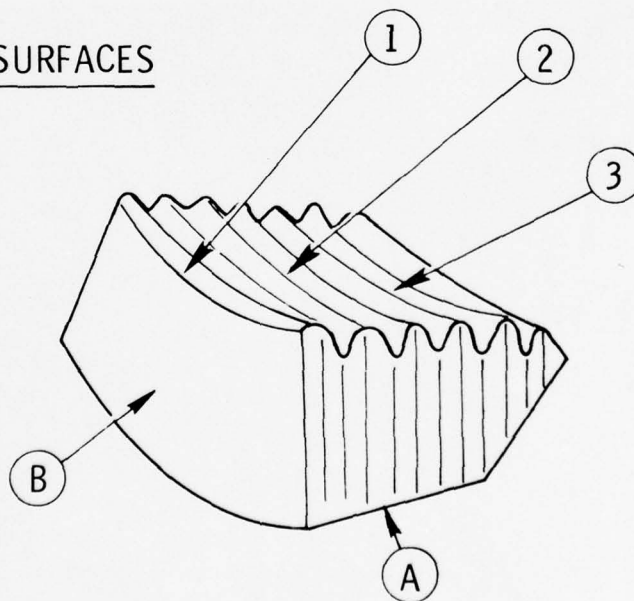
Figure 51. Photomicrograph Location, Throat Supports SN001 and SN002

Figure 52. Throat Support SN001 AG Carb 5451 (K 550D)
Metallograph Reference Photograph
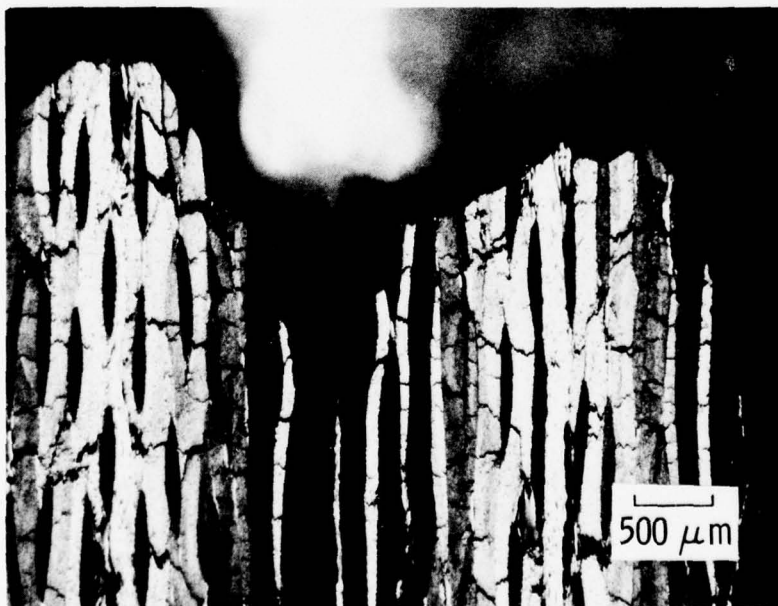
Figure 53. Throat Support SN001 Metallograph Location 2 (500 μm)

Figure 54.   Throat Support SN001 Metallograph Location 1 (500 μm)

Figure 55.   Throat Support SN001 Metallograph Location B (200 μm)

reinforcement orientation is directly affecting the performance of the part. Two facts acted as deterrents to such a conclusion. First, the condition of these parts commonly has not been noted in other parts made in a similar manner. Second, if the orientation of the reinforcement is driving the mass removal and, as we can see from the section view, the plies have been rotated, then the erosion pattern axially should be spiral grooving not merely repetitive delaminations. It therefore was evident that a more detailed examination of the structure was required prior to drawing a conclusion as to causes for the anomalous performance.

A check of the local porosity reveals a 30% increase in open porosity in the grooved regions over those areas containing peaks. In addition, there is a substantial reduction in fiber packing in the grooved areas. The center-to-center packing spacing at the peaks is on the order of 10 to 11 mil; but the same spacing in the grooves is 15 to 16 mil. These factors have led us to the following conclusion. The anomalous erosion/corrosion performance of the throat retainers was caused, at least in part, by the fabrication processing technique. It appears that a partial cure of or a debulking operation on each set of lamina between valleys was effected during process and prior to total composite cure. The resultant composite then is similar to a series of shingles bonded together by glue lines that, when exposed to the thermal environment of the rocket motor firing, delaminate at these planes of weakness. The fact that separation occurred early is shown by the SEM photomicrographs of the surface at the delamination locations. Figures 56, 57, and 58 are increasingly higher-magnification SEM photomicrographs taken at a delamination site. The smooth surfaces of the individual plies and of the walls surrounding the separation indicate that this phenomenon occurred early, allowing the corrosion process to proceed at some depth between plies. Figure 59 is an SEM photomicrograph similar to Figure 56, but taken at another location on the surface. This figure shows the same material response as that seen in location 1. Figure 60 is a photomicrograph of the surface at location 2.

Figure 56. Throat Support SN001 SEM Location 1 (500 µm)
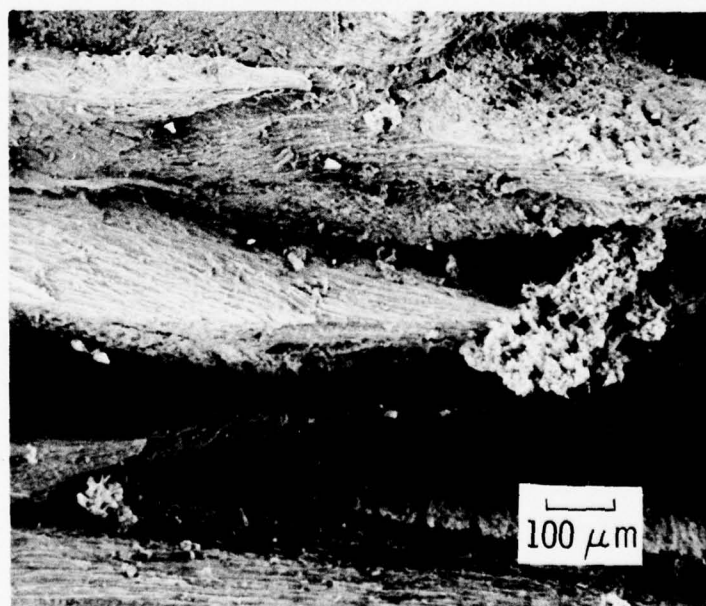
Figure 57. Throat Support SN001 SEM Location 1 (100 µm)
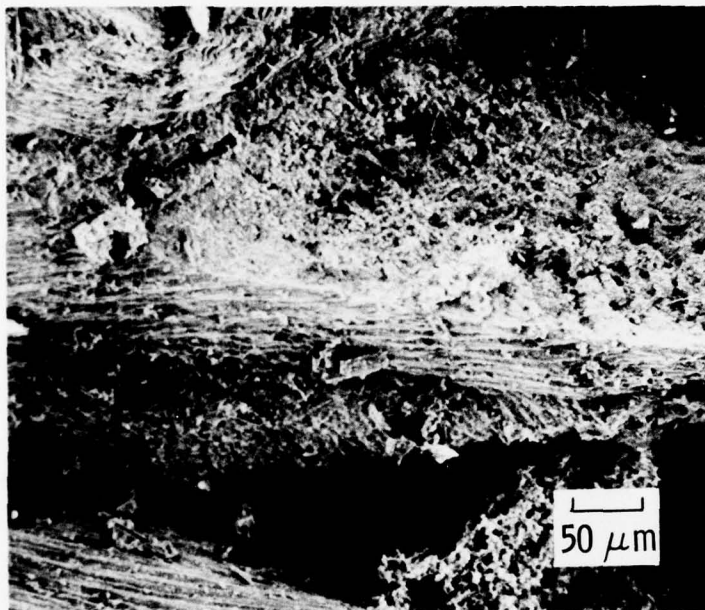
Figure 58. Throat Support SN001 SEM Location 1 (50 μm)
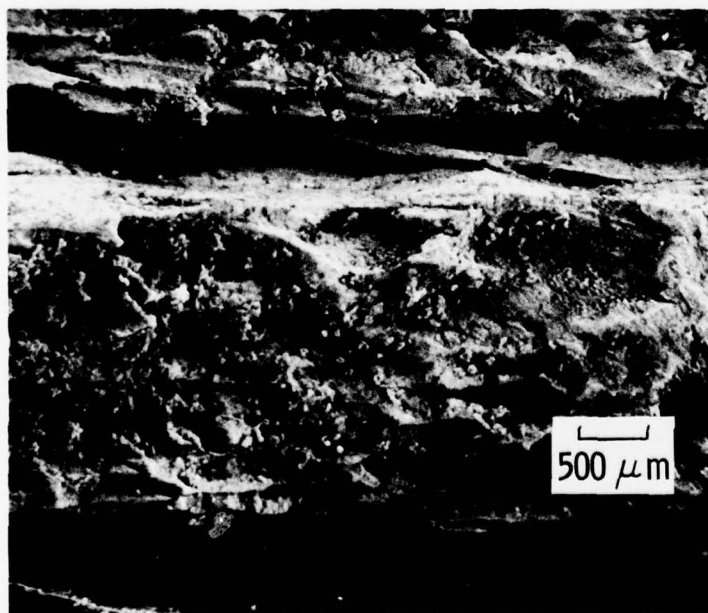
Figure 59. Throat Support SN001 SEM Location 2 (500 μm)
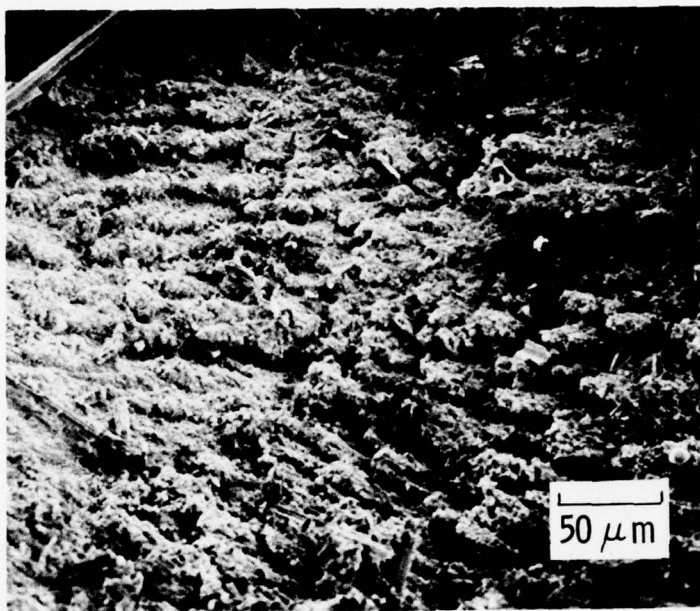
Figure 60.   Throat Support SN001 SEM Location 2 (50 μm)

4.   THROAT SUPPORT SN002 – AG CARB 5451 FLAT
     LAMINATE

As mentioned in the preceding section, the erosion pattern of throat
support SN002 was very similar to that of SN001. The photomicrographs
of SN002 were taken to be complementary to SN001. Figure 61 shows the
overall cross section of throat support SN002 after test. Figures 62 and 63
are photomicrographs taken along the fired surface. Figure 64 illustrates
the weave structure at 90 deg to the fired sections. The sawtooth erosion
pattern is again very evident. In this case, the peaks and valleys do not
coincide with the reinforcement direction, as noted for throat support SN001.
Figure 63, taken in slightly off cross-polarized light, dramatically illus-
trates the lack of systematic repetition of the light and dark patterns. This
fact supports the hypothesis that fabrication condition rather than weave
geometry is driving performance of these parts. Figures 65 and 66 are
photomicrographs of the fired surface at location 1 (see Fig. 51). They show
a structure quite similar to throat support SN001.

Figures 67, 68, and 69 are SEM photomicrographs taken at areas 1,
2, and 3 of the exit surface. These photographs illustrate an interesting feature
common to all locations of the exit surface. In each case, the reinforce-
ment has been removed to a significantly greater depth than the matrix.
Although insufficient data exist on which to base a conclusion, efforts to
find the cause of this phenomenon will be continued. Intuitively, this
phenomenon seems inconsistent with a mass removal mechanism that is
predominantly thermochemical. Determining the casual relationship between
these materials, i.e., the matrix-reinforcement combination, and their
response may be a key element in pinpointing performance.

Figures 67-69 also show the presence of a foreign element or com-
pound that exists in the form of microspheroids that are randomly distributed
along the surface of the matrix. A high magnification photomicrograph of
one sphere (Fig. 70) indicates the smooth nature of the material. This
quality, coupled with the location at the peaks of the residue matrix,

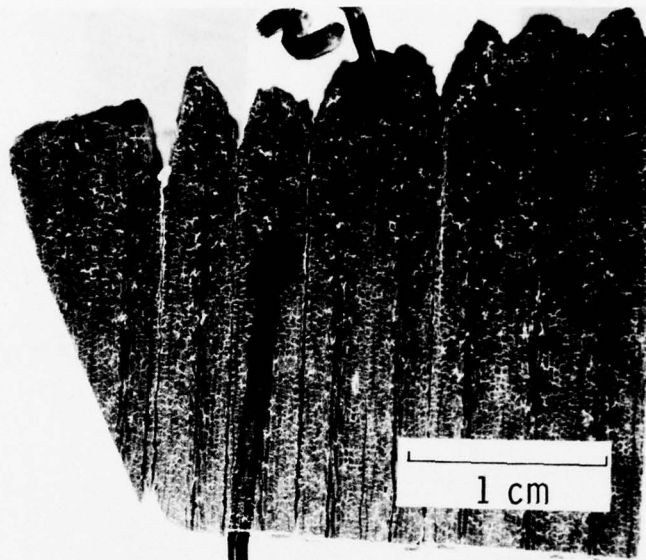Figure 62. Throat Support SN002 Metallograph Location 2 (500 μm)
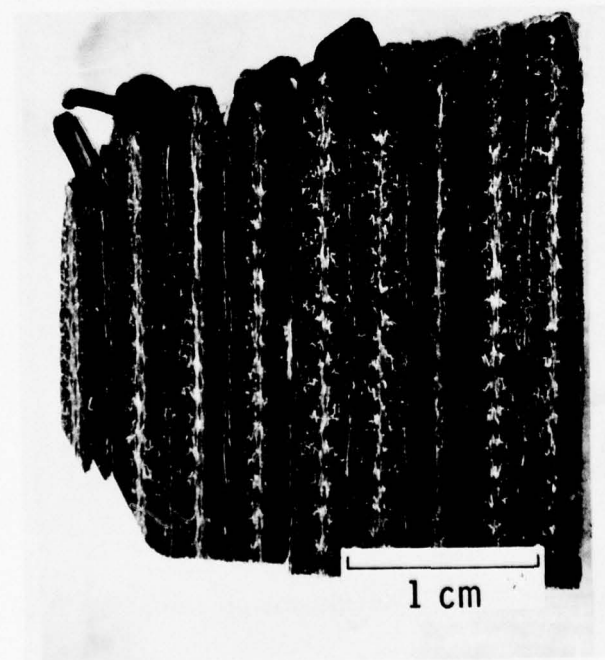
Figure 61. Throat Support SN002 AG Carb 5451 (K 550D) Metallograph Reference Photograph

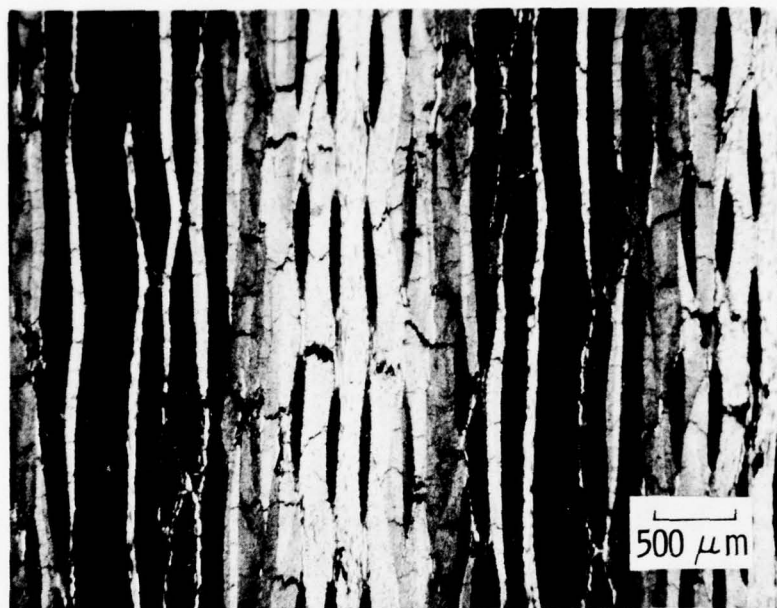Figure 63.   Throat Support SN002 Metallograph Location 3 (500 μm)
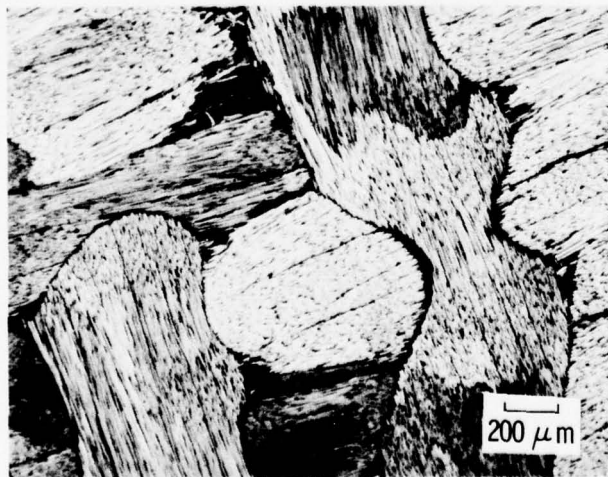
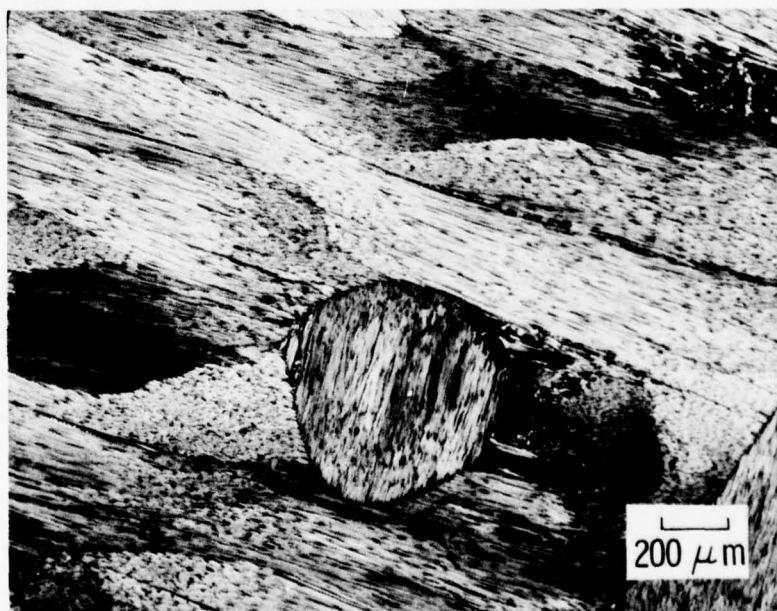Figure 64.   Throat Support SN002 Metallograph Location B (200 μm)
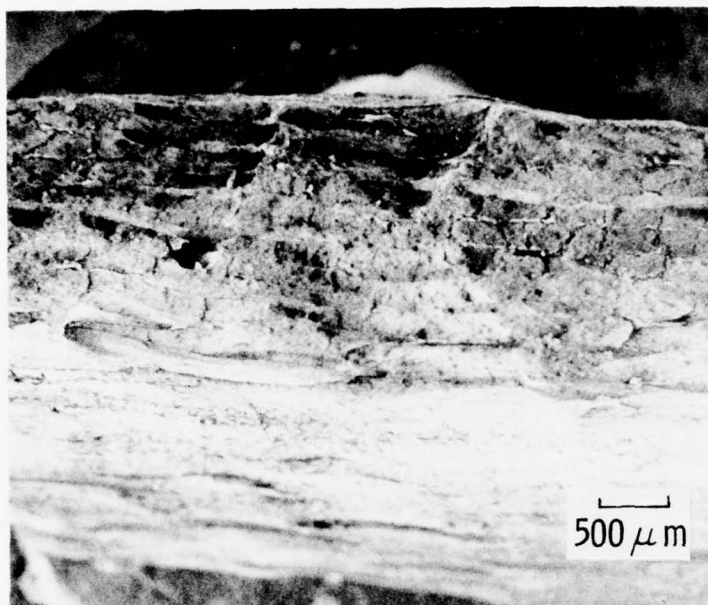
Figure 65. Throat Support SN002 SEM Location 1 (500 μm)
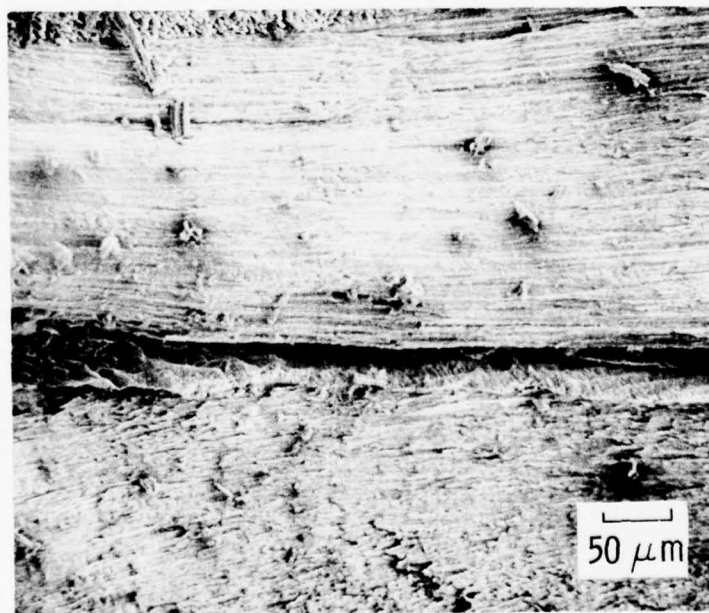
Figure 66. Throat Support SN002 SEM Location 1 (50 μm)

Figure 68. Throat Support SN002 SEM
Location 2 (5 μm)

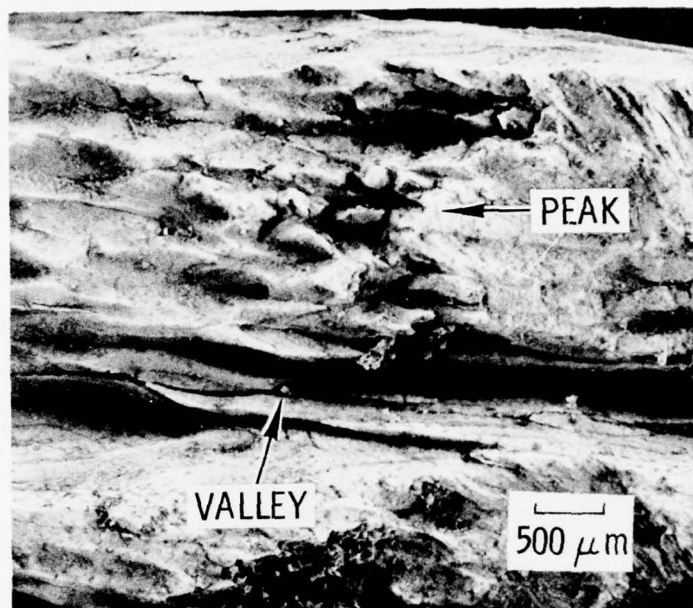
Figure 67. Throat Support SN002 SEM
Location 1 (5 μm)
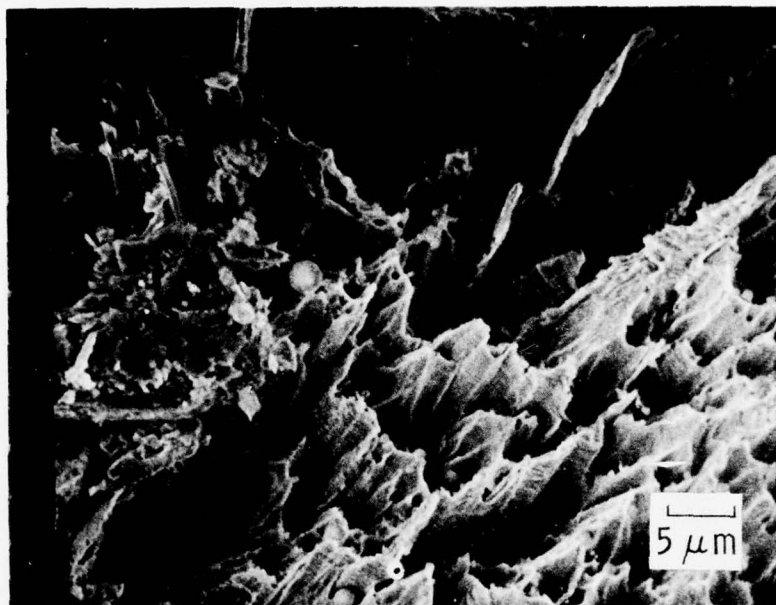
Figure 69.   Throat Support SN002 SEM Location 3 (5 μm)
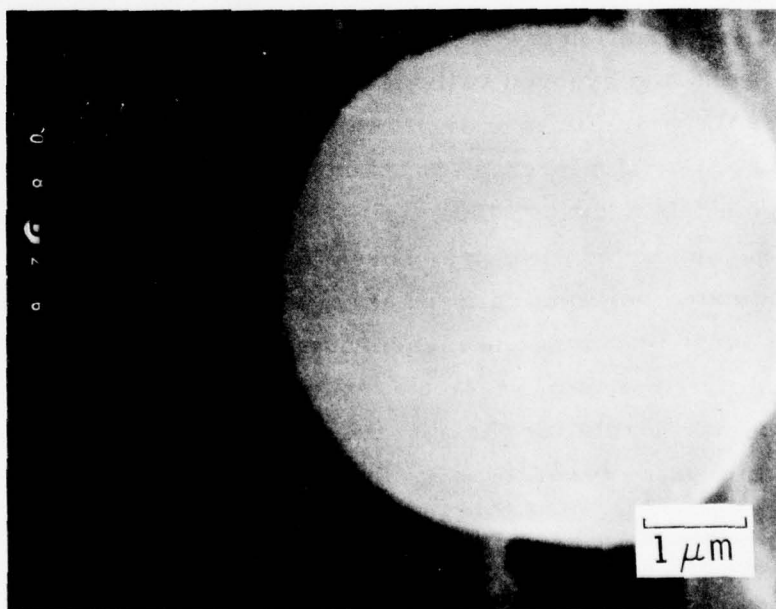
Figure 70.   Throat Support SN002 SEM Location 2 (1 μm calcium spheroid)

indicates that the material was condensed on the surface at the end of the firing or at blow-down. An EDAX scan of the material (Fig. 71) determined that it was primarily calcium. The area was also subjected to inspection by the ion microprobe mass analyzer (IMMA). Figure 72 is a calcium map made of a single spheroid that verifies the predominance of elemental calcium.

C. SURFACE ROUGHNESS MEASUREMENTS[*]

Surface roughness affects heat transfer and ablation rate in reentry vehicle nose tip environments and has been correlated to microstructural parameters in carbon-carbon materials.[2] Quantitative estimates of the roughness of ablating surfaces of carbon-carbon rocket motor parts also may prove useful. In a limited exploratory effort, the posttest surface roughnesses were measured on samples from two carbon-carbon nozzle inlets. The two materials were the 3D cylindrical woven part and a 2D rosette part, both fired in the second-stage MX test. The parts exhibited circumferential variation in erosion that appeared as an alternating series of rounded peaks and grooved valleys. Figure 73 shows this variation in a portion of the 3D part. For investigation of this phenomenon, roughnesses were measured at two circumferential locations on each part, a peak region and a valley region. In addition, the axial variation in roughness was explored in a valley region on the 3D part. These locations of roughness measurement are indicated schematically in Fig. 74. In addition to summarizing the quantitative roughness data and measurement techniques, this section includes some estimates of surface area augmentation as well as some qualitative remarks relating the observed roughness elements to the materials' microstructure.

---

[*] The technical effort for this section was provided by F. I. Clayton and J. Jortner, McDonnell Douglas Astronautics Company, Huntington Beach, California.
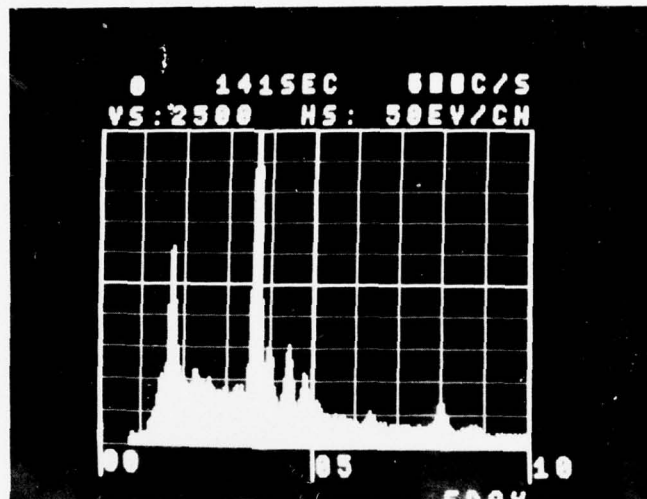
Figure 71. Throat Support SN002 EDAX Scan
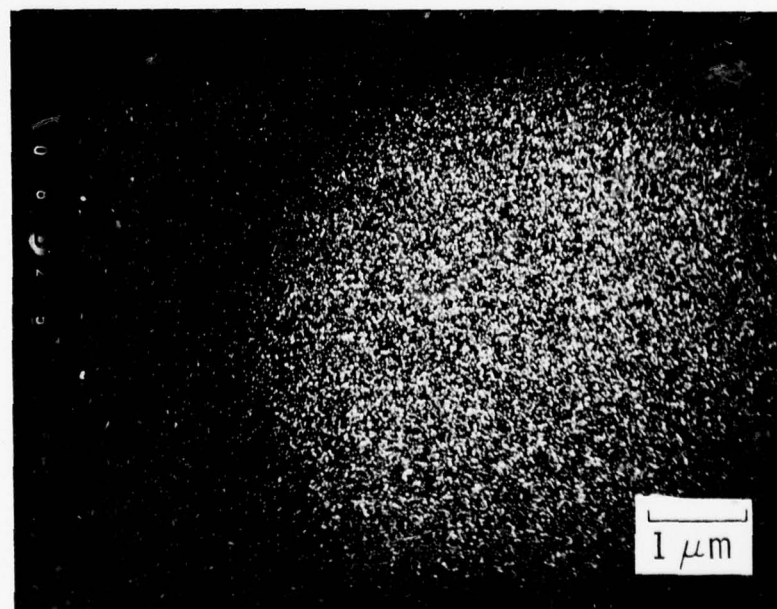
Figure 72. Throat Support SN002 SEM Location 2 (1 μm calcium map)

PEAK   VALLEY

1.5 cm
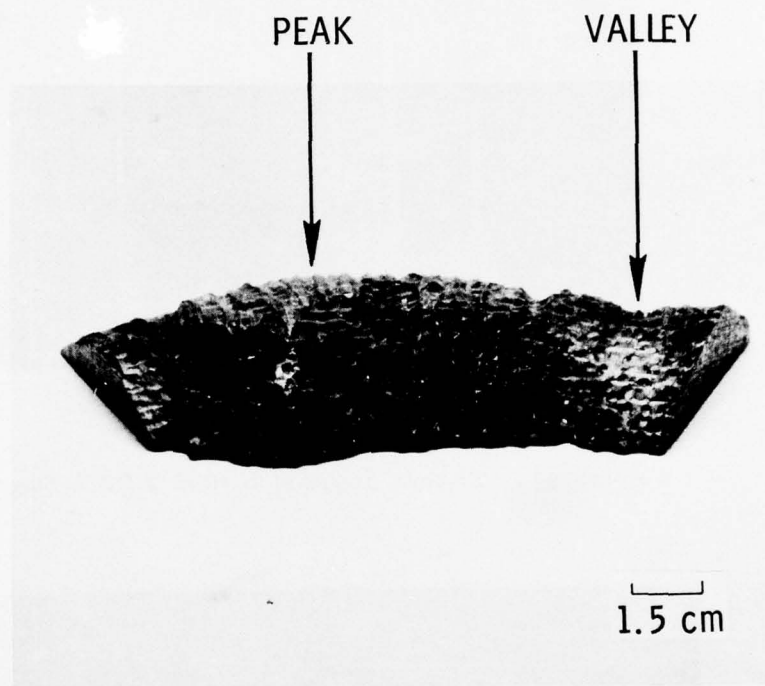
Figure 73. Photograph of Portion of 3D Carbon-Carbon Entrance Section
Posttest with Circumferential Variation in Erosion Shown
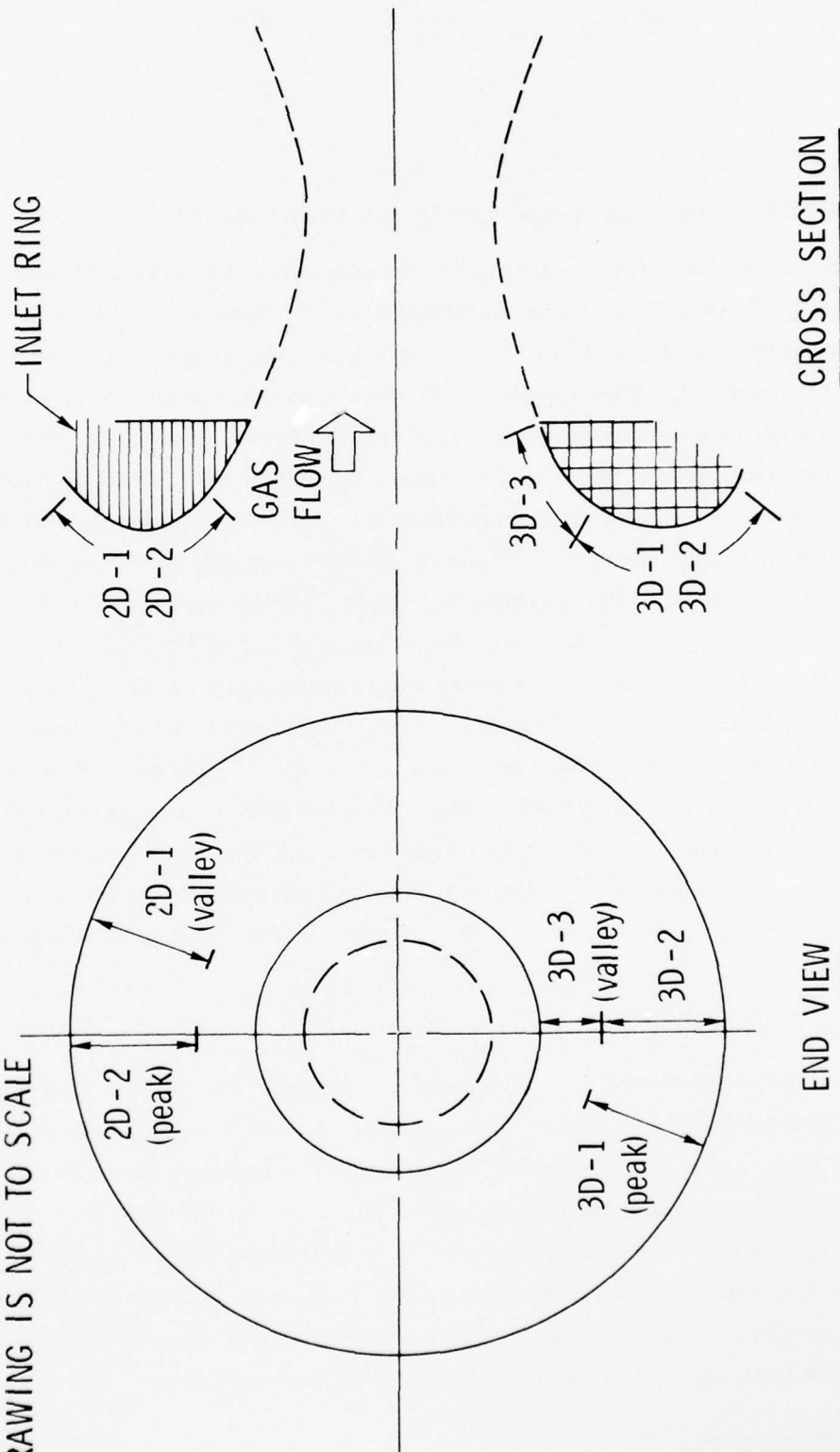
Figure 74. Schematic of Locations of Roughness Data Acquisition

1.   PROCEDURE FOR ROUGHNESS MEASUREMENT

The procedure for obtaining the measurements is as follows: The specimen is inspected visually to determine the locations for sectioning. The specimen is sectioned so that an axial profile of the cross section of the surface is obtained. The specimen is then mounted in an epoxy compound, cured, and polished utilizing standard metallurgical polishing techniques. Photomicrographs are taken of the entire length of the cross section. These micrographs are cut and spliced together to form a continuous mosaic of the cross section of the surface. Figures 75-79 show the mosaics obtained for the present samples. The sample numbers key the mosaics to the locations shown in Fig. 74. These mosaics have been reduced in size for convenience in presentation; the actual roughness measurements, as described below, are made at a higher magnification. Onion skin paper is overlaid on this mosaic, and the surface contour is traced by hand. This tracing is inspected visually, and the individual surface irregularities are marked for width and location of peak and are numbered. Such a tracing is shown in Fig. 80, which is a surface contour of the 2D rosette entrance designated SN001. A standard grid is used to measure the height, width, and peak-to-peak spacing.

2.   ROUGHNESS DATA

The measurements are tabulated in Tables 1-5. The numbers for each roughness element are in scale units; each unit is equal to 0.002 in. Relevant aspects of the theory of roughwall effects upon skin friction and heat transfer have been summarized.[3] The parameter used in heat transfer analysis to characterize roughness is the equivalent sand roughness, which combines the effects of height, width, spacing, and inclination of the elements into one number. The equations used to convert the measurements of Tables 1-5 into equivalent sand roughness k_s are presented as

[3]R. B. Dirling, Jr. , "A Method for Computing Roughwall Heat Transfer Rates on Reentry Nosetips," presented at AIAA 8th Thermophysics Conference, Palm Springs, California, 16-18 July 1973.

FLOW

├─0.100 in.─┤

RADIAL
DIRECTION
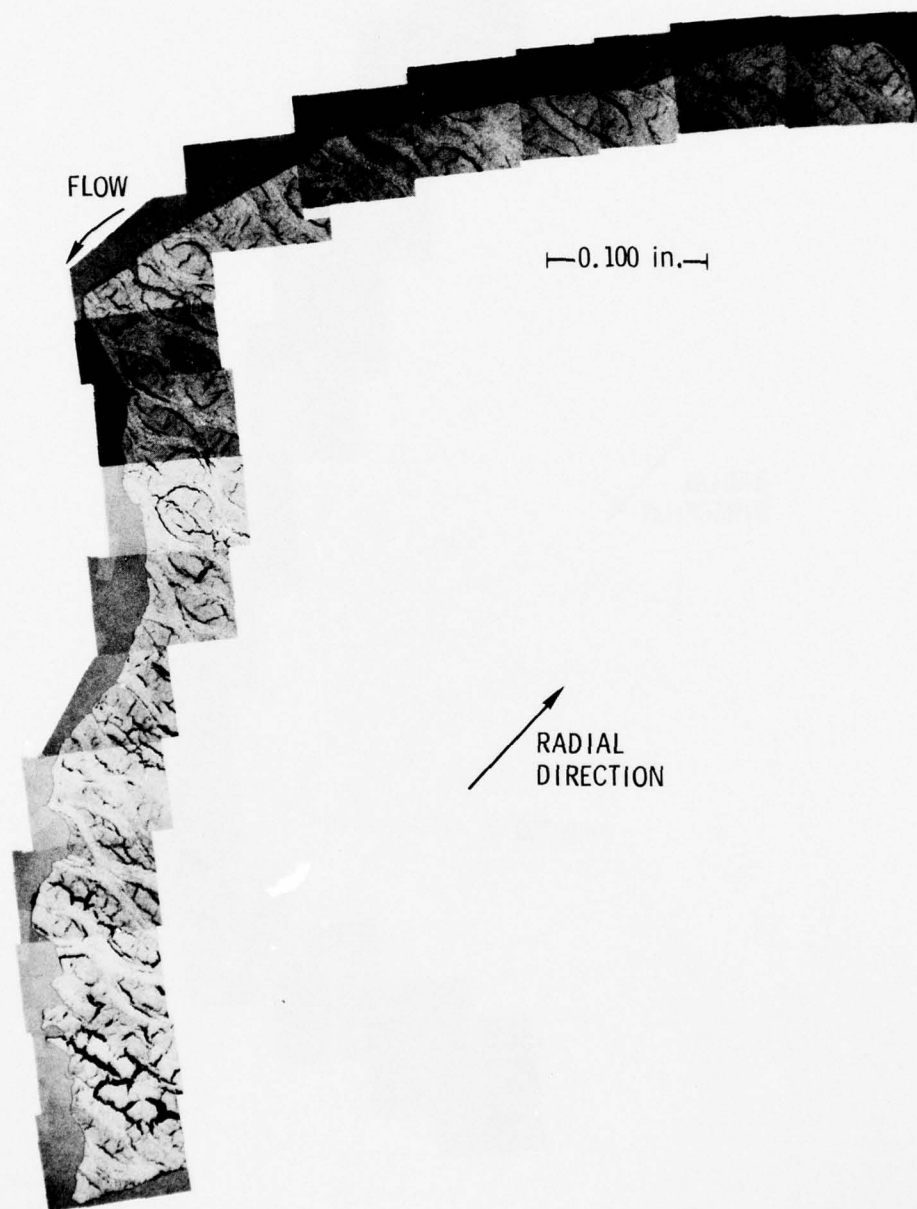
Figure 75. Photomicrograph Mosaic, 2D-1

FLOW

RADIAL
DIRECTION

├─0.100 in.─┤
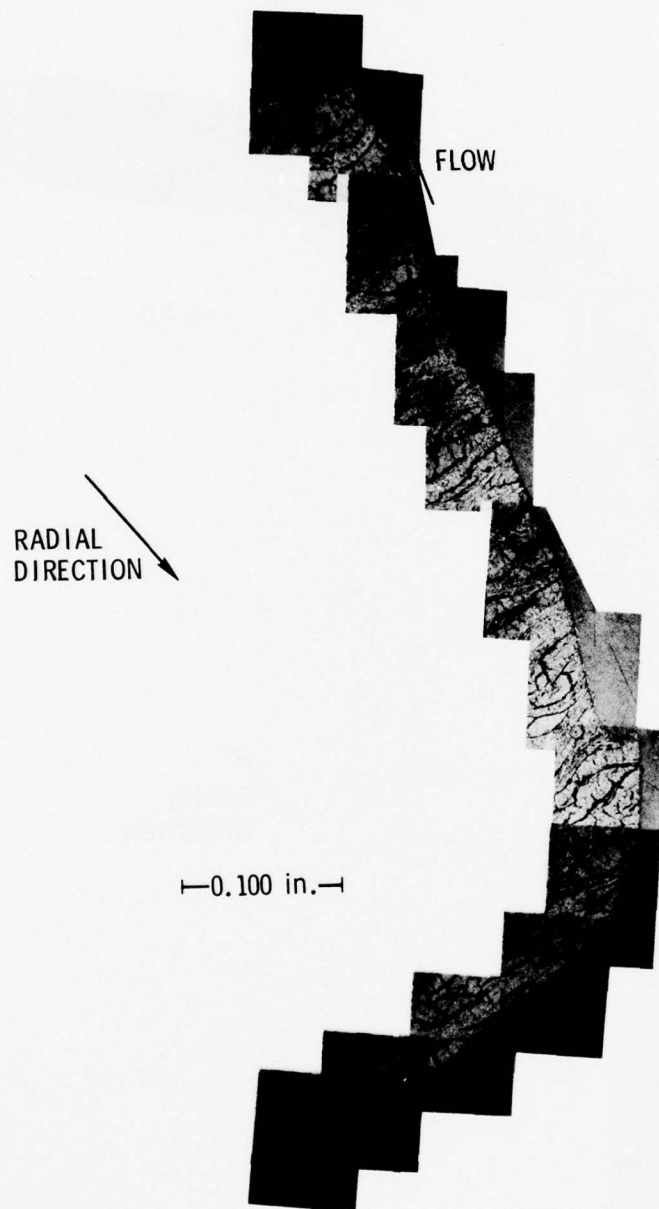
Figure 76. Photomicrograph Mosaic, 2D-2

FLOW

⊢0.100 in.⊣

RADIAL
DIRECTION
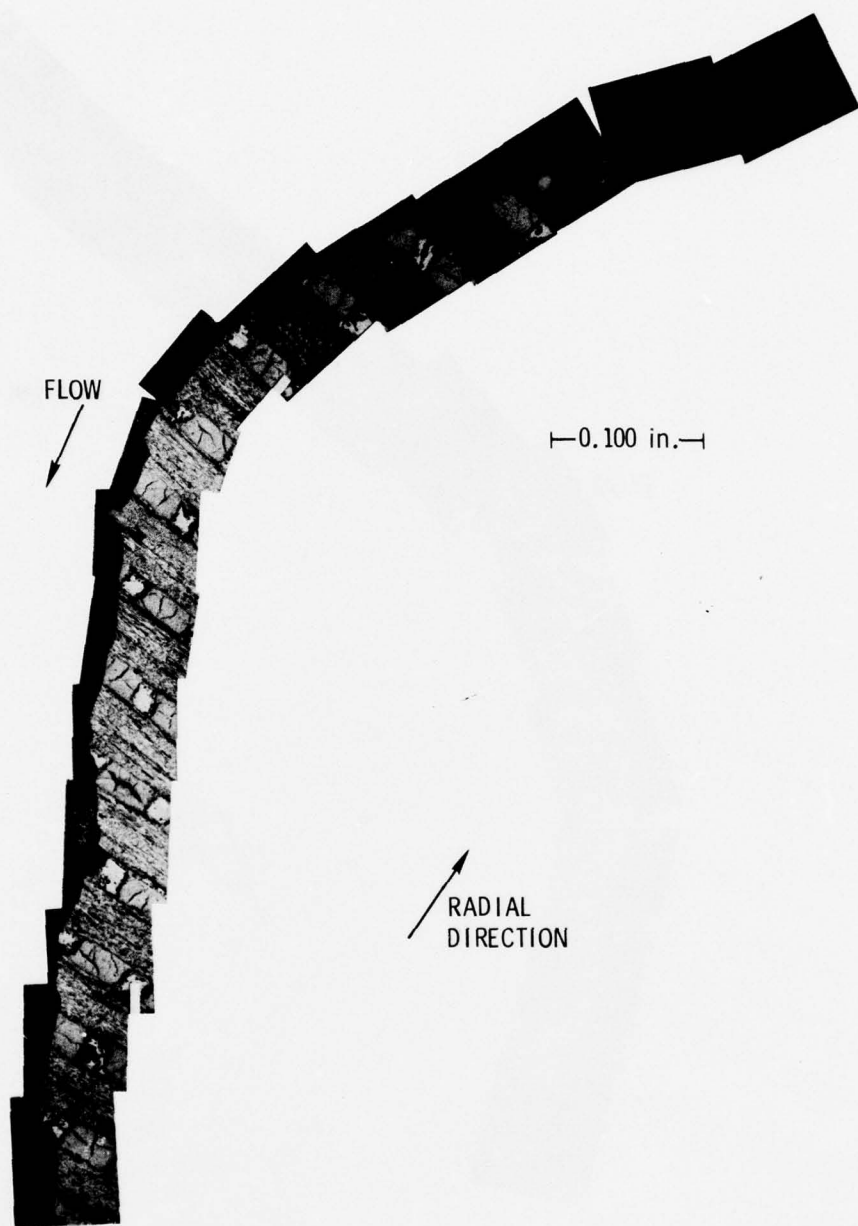
Figure 77. Photomicrograph Mosaic, 3D-1
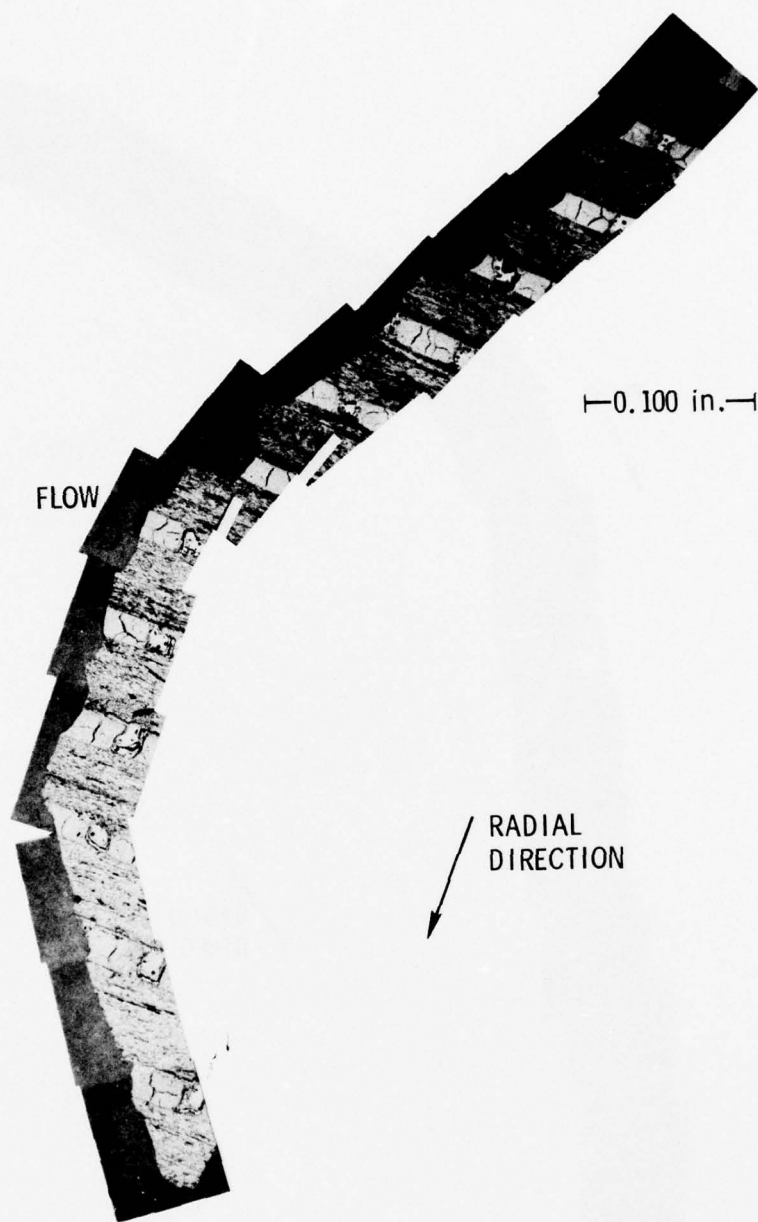
Figure 78. Photomicrograph Mosaic, 3D-2

FLOW

RADIAL
DIRECTION

⊢0.100 in.⊣
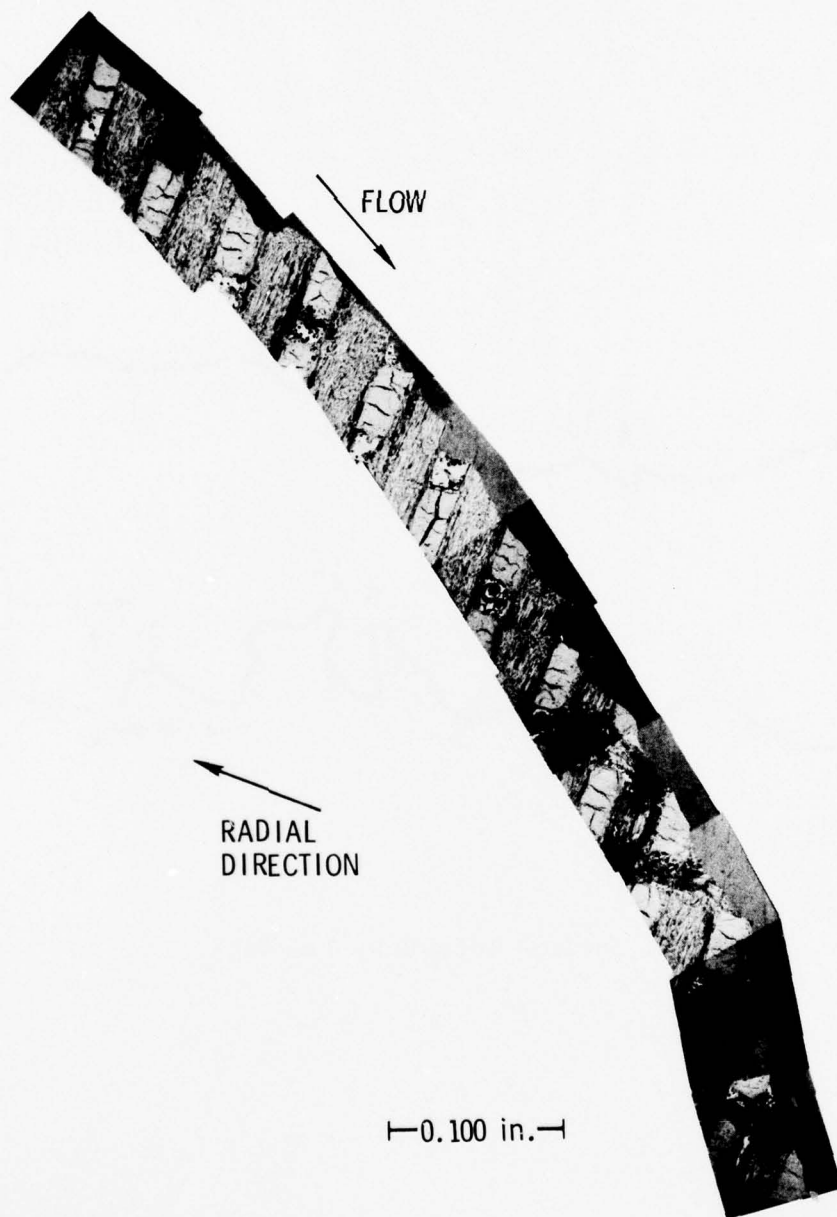
Figure 79. Photomicrograph Mosaic, 3D-3

ROUGHNESS
ELEMENT
NUMBER
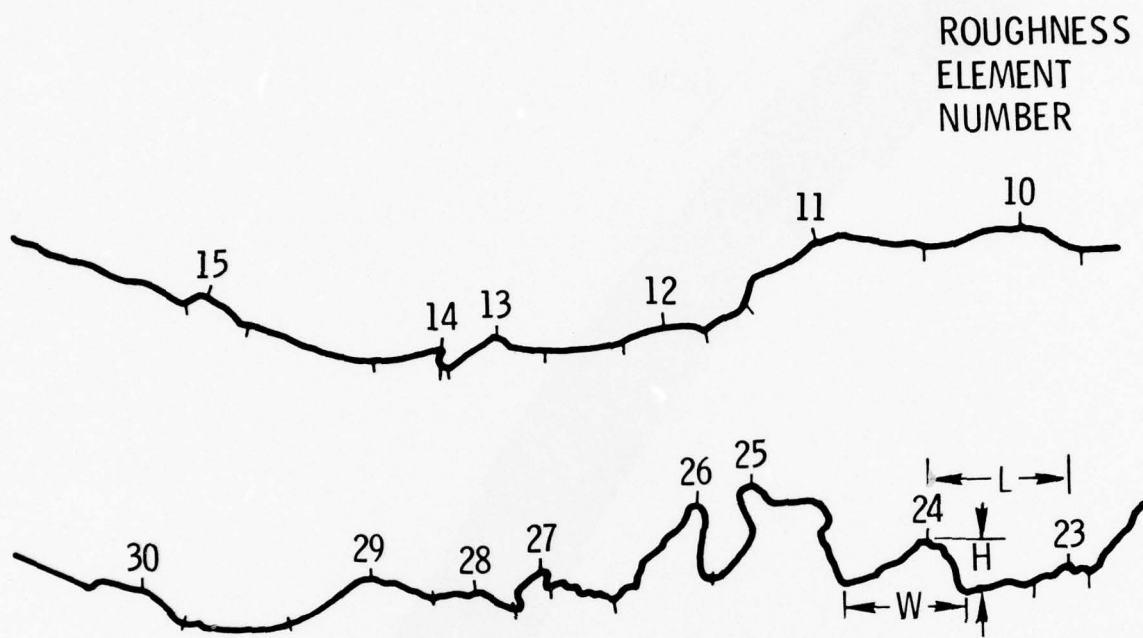
Figure 80. Surface Roughness Tracings

Table 1. Surface Roughness Data, Sample 3D-1

No.	h	W	L
1	1.5	12.0	12.5
2	1.5	12.0	24.0
3	1.0	15.0	8.5
4	1.0	2.5	7.0
5	2.5	14.5	34.5
6	1.5	29.5	25.0
7	0.5	5.0	6.0
8	0.25	2.5	22.0
9	1.5	37.0	14.0
10	1.0	10.0	27.0
11	2.0	20.0	11.0
12	0.5	8.0	7.0
13	0.5	5.0	4.5
14	0.25	3.0	3.5
15	0.25	5.0	5.5
16	0.25	2.0	4.0
17	0.25	3.0	3.5
18	0.5	4.5	19.0
19	4.5	17.5	9.0
20	0.5	8.0	10.0
21	0.5	4.5	10.0
22	5.0	16.0	20.5
23	1.0	23.0	26.0
24	0.5	7.0	9.0
25	0.5	3.0	11.0
26	1.0	13.5	9.0
27	1.5	8.0	11.0
28	0.5	5.0	12.0
29	1.0	14.0	8.5
30	1.0	5.0	11.0
31	2.0	6.0	19.0
32	2.0	19.0	12.0
33	1.5	15.0	50.0
34	4.0	41.5	33.0
35	3.5	24.5	

$h_{av} = 1.35$ $W_{av} = 12.03$ $L_{av} = 14.72$

$k_{av} = 1.72$ $= 24.06$ mil 29.44 mil

$= 44$ mil $(W_2)_{av} = 237.9$

$= 951.6$ mil^2

$D = 37.028$

$\lambda = 31.00$

$k_s/k_{av} = 0.204$

$k_s = 0.701$ mil

Table 2. Surface Roughness Data, Sample 3D-2

No.	h	W	L
1	0.75	14.0	21.0
2	2.25	18.0	11.5
3	1.5	2.0	26.0
4	2.5	32.0	14.5
5	0.5	3.5	5.5
6	1.5	5.5	33.5
7	0.5	8.0	11.5
8	1.5	11.5	21.0
9	2.25	13.0	15.0
10	3.0	17.5	20.0
11	3.25	19.5	45.0
12	7.5	23.0	40.0
13	1.25	12.0	21.0
14	7.0	29.0	37.0
15	6.0	29.0	24.0
16	6.0	28.5	20.0
17	1.0	10.5	

$L_{av} = 22.91$

$h_{av} = 2.84$ $W_{av} = 16.26$ $= 45.81$ mil

$k_{av} = 3.618$ $= 32.53$ mil

$= 7.236$ mil $(W^2)_{av} = 348.22$

$= 1392.9$ mil^2

$D = 48.059$

$\lambda = 19.13$

$k_s/k_{av} = 0.5103$

$k_s = 3.693$ mil

-92-

Table 3. Surface Roughness Data, Sample 3D-3

No.	h	W	L
1	2.5	15.5	18.5
2	0.75	12.0	12.0
3	9.0	29.5	40.0
4	6.5	43.5	42.0
5	0.5	4.0	23.5
6	5.0	25.0	13.0
7	3.0	18.5	30.0
8	1.75	20.0	19.0
9	3.5	14.0	13.5
10	2.5	9.0	5.0
11	0.25	2.5	3.0
12	0.5	3.0	15.5
13	4.5	31.0	35.0
14	2.75	23.0	5.0
15	1.0	7.0	28.5
16	6.5	37.5	24.0
17	3.5	15.5	15.0
18	1.25	12.0	15.5
19	0.5	4.0	5.0
20	3.5	8.0	11.0

$h_{av} = 2.869$ $W_{av} = 16.36$ $L_{av} = 18.7$

$k_{av} = 3.655$ $= 32.71$ mil $= 37.4$ mil

$= 7.31$ mil

$(W^2)_{av} = 395.8$

$= 1583.4$ mil^2

$D = 46.17$

$\lambda = 18.19$

$k_s/k_{av} = 0.5614$

$k_s = 4.104$ mil

Table 4. Surface Roughness Data, Sample 2D-1

No.	h	W	L
1	0.5	4.5	6.0
2	1.5	6.0	22.0
3	5.0	45.0	37.5
4	0.5	4.0	15.0
5	1.5	4.0	10.5
6	1.5	25.0	56.0
7	2.5	18.0	90.0
8	2.0	13.5	17.0
9	0.5	15.0	10.0
10	0.25	1.5	15.0
11	1.5	12.0	15.0
12	3.0	13.0	12.5
13	0.5	6.0	12.5
14	1.5	7.0	4.0
15	1.0	5.0	17.0
16	1.0	5.0	22.0
17	1.0	12.0	13.5
18	1.0	10.5	8.5
19	2.5	16.0	25.0
20	1.5	6.5	4.0
21	1.0	2.0	4.5
22	2.5	6.5	20.0
23	7.5	22.0	8.0
24	1.0	4.0	10.5
25	4.0	9.0	13.0
26	7.5	9.0	4.0
27	6.0	8.0	12.0
28	3.0	7.0	4.0
29	1.0	6.0	7.0
30	2.0	11.0	18.0
31	1.0	7.5	

h_{av} 2.15325 W_{av} 10.371 L_{av} 17.1333

34.2667 mil

k_{av} 2.74157   20.7419 mil

5.48314 mil $(W^2)_{av}$ 177.64

710.55 mil

D 37.188

λ 19.668

k_s/k_{av} 0.484

k_s 2.654 mil

-94-

2 OF 2
AD
A038159

END
DATE
FILMED
5—77

Table 5. Surface Roughness Data, Sample 2D-2

No.	h	W	L
1	1.0	10.0	7.0
2	0.75	8.0	10.0
3	0.5	8.0	69.0
4	0.5	2.0	5.0
5	0.25	1.5	7.0
6	0.25	1.5	2.0
7	0.5	3.5	3.0
8	0.5	2.5	4.0
9	1.0	5.5	8.5
10	3.0	9.0	7.5
11	1.0	3.0	5.5
12	1.0	7.5	13.5
13	2.5	23.5	55.0
14	1.0	2.0	1.5
15	0.5	1.5	2.0
16	0.5	4.5	5.5
17	0.5	2.5	2.0
18	0.5	2.0	2.0
19	0.75	1.5	2.5
20	1.0	2.5	20.0
21	1.25	18.0	7.0
22	0.75	6.0	33.0
23	0.5	3.5	21.0
24	0.5	3.0	5.0
25	1.75	11.0	6.5
26	0.75	2.5	2.5
27	0.75	2.5	6.5
28	1.75	11.5	7.5
29	0.5	3.0	2.0
30	0.5	1.5	2.0
31	1.0	5.0	7.0
32	2.75	16.5	7.0
33	0.75	5.0	6.0
34	0.75	2.0	10.5
35	1.0	14.0	18.0
36	2.5	14.0	5.0
37	1.25	3.0	31.0
38	1.2	2.0	5.0
39	0.75	3.0	2.0
40	0.75	3.0	7.0

Table 5. Surface Roughness Data, Sample 2D-2 (Continued)

No.	h	W	L
41	1.75	7.5	5.5
42	1.5	7.0	5.0
43	1.2	4.5	4.0
44	1.0	5.0	5.5
45	0.5	1.0	8.0
46	2.5	13.0	9.0
47	0.5	2.0	3.0
48	1.0	5.0	4.0
49	0.5	1.0	2.5
50	1.0	5.0	8.0
51	1.0	2.0	3.0
52	0.5	1.0	2.5
53	1.0	3.0	3.0
54	2.0	2.0	8.0
55	1.5	4.0	4.0
56	0.75	1.5	5.0
57	0.5	4.5	13.0
58	1.0	10.5	32.0
59	0.5	1.5	6.5
60	1.0	8.0	4.5
61	0.75	1.5	3.0
62	1.0	2.5	10.0
63	1.0	13.0	8.5
64	0.5	1.0	1.0
65	1.0	2.0	37.0
66	2.75	34.0	48.0
67	2.0	11.0	6.0
68	0.75	3.0	12.0
69	2.0	17.0	15.0
70	0.5	9.0	8.5
71	2.0	9.0	15.0
72	2.0	14.0	6.0
73	1.0	2.5	2.0
74	1.0	2.0	1.5
75	0.5	1.5	4.0
76	2.0	11.0	10.0
77	2.0	5.0	

$h_{av} = 1.0799$ $W_{av} = 5.974$ $L_{av} = 9.856$
$= 19.672$ mil

$k_{av} = 1.375$ $= 11.948$ mil

2.75 mil $(W^2)_{av} = 69.08$
$= 276.3$ mil^2

$D = 23.15$

$\lambda = 24.412$

$k_s/k_{av} = 0.321$

$k_s = 0.883$ mil

-96-

$$k_{av} = \frac{4}{\pi} h_{av}$$

$$\lambda = \left(\frac{D}{k_{av}}\right)\left(\frac{A_p}{A_s}\right)^{-4/3}$$

$$D = \left[\frac{3\pi}{8} L_{av} \frac{(W^2)_{av}}{W_{av}}\right]^{1/2}$$

and

$$\frac{k_s}{k_{av}} = \begin{cases} 139\, \lambda^{-1.9} & \text{for } \lambda > 4.93 \\ \\ 0.0164\, \lambda^{3.78} & \text{for } \lambda > 4.93 \end{cases}$$

where

h_{av} = average measured roughness height

L_{av} = average roughness peak-to-peak spacing

W_{av} = average roughness width

The quantity A_p/A_s represents the ratio of the proposed area of the roughness element in the flow direction to the windward surface area, accounts for the inclination of the roughness element to the flow, and is generally assumed to equal 0.45. Table 6 summarizes the results.

Table 6. Summary of Measurements

Sample[a]	Sample Location	Equivalent Sand Roughness k_s (mil)	Surface Area Ratio Estimated ζ
3D-1	Upstream Peak	0.701	1.11
3D-2	Upstream Valley	3.69	1.22
3D-3	Downstream Valley	4.10	1.28
2D-1	Upstream Valley	2.65	1.19
2D-2	Upstream Peak	0.88	1.08

[a]See Figs. 73 and 74 for sample location nomenclature

In rocket nozzle applications, it appears that the surface thermo-chemistry may be controlled by the rate at which reactions between the solid surface and the exhaust gas occur. Thus, there is an excess of gaseous reactant at the surface. Consequently, the more surface area available for reaction, the more mass loss will occur. Obviously, a roughened surface such as that shown in Fig. 73 has more available surface area for reaction than a smooth surface. The cross section mosaics also were used to estimate the ratio of roughened-to-smooth surface areas by measuring the length along the surface, dividing this by the smooth length, and squaring the result. The values obtained are presented in Table 6 and plotted versus equivalent sand roughness in Fig. 81.

3. MICROSTRUCTURAL OBSERVATIONS

Micromechanical arguments and direct observation of microstructure at elevated temperatures[2] suggest that many of the cracks seen in carbon-carbon close as the composite is heated to ablative temperatures. The sketches of Fig. 82 illustrate the probable differences in local surface
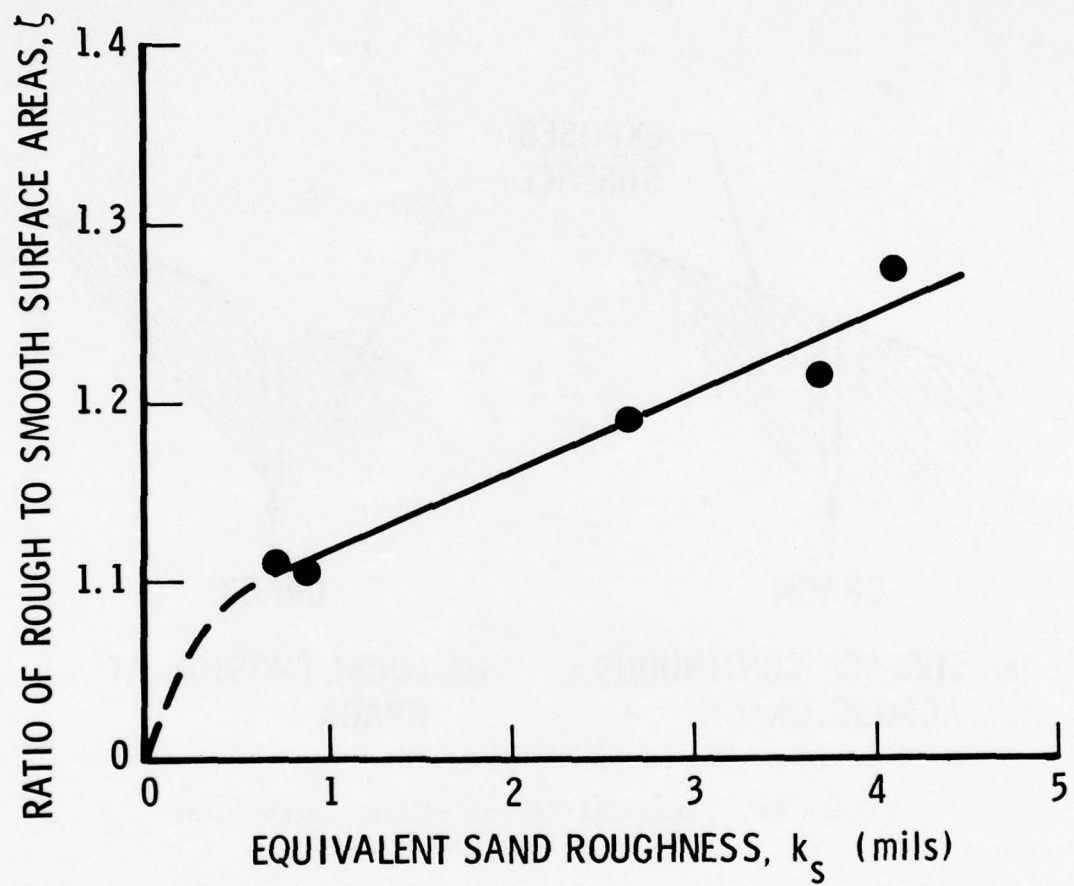
Figure 81. Roughened Area Correlation
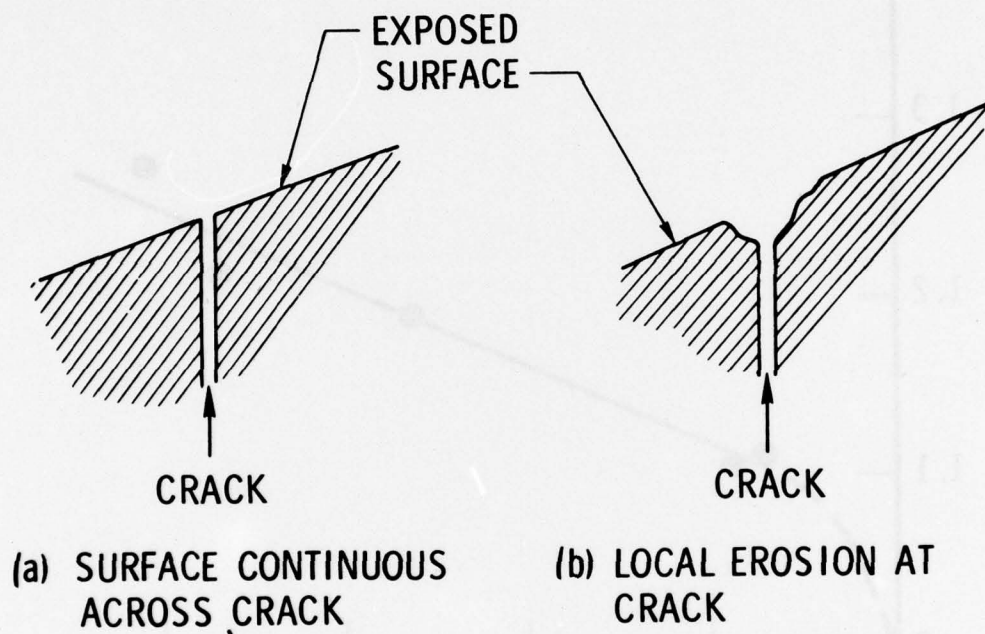
Figure 82. Potential Effects of Microstructural
Cracks at Exposed Surface

contour between closed cracks, which would be expected to give a continuous surface as in Fig. 82(a), and cracks that remain open, which would result in recession at the crack faces, Fig. 82(b). Review of Figs. 75 through 79 shows that most of the surfaces conform to Fig. 82(a); only in the downstream portion of sample 2D-1 is there significant evidence of local erosion at the cracks (Fig. 75), and this appears to be associated with a region of anomalously wide cracks and large porosity in the material. Figure 83 shows a portion of sample 3D-2 to illustrate the typical continuity of the surface across the cracks in the 3D material.

Whereas in most areas the crack faces do not appear to be preferentially eroded, the cracks do appear to be involved in mechanical (as opposed to chemical) mass removal. For example, Fig. 84 shows evidence that chunks of material may have been lost from sample 3D-3, presumably a consequence of weak bonding or cracks. This, of course, may be attributed to inadvertent mass removal during the polishing step. However, past results in similar work on nose tip carbon-carbons do not indicate a history of this kind of problem. Other examples can be seen in Figs. 77 and 79.

A thin film of unknown origin was observed on the ablated surfaces of both materials. Figure 85 shows a closeup view of the film on a portion of sample 3D-1.

D.   THERMAL EXPANSION AND STABILITY

The objectives of this portion of the characterization effort were threefold. First, thermal expansion excursions were to be developed in each of the primary reinforcement material directions. Second, the thermal stability of each material was to be investigated by cycling the thermal expansion excursions after a half hour heat treat at 5452°F. Third, the effect of thermal exposure to the rocket motor firing was to be examined by comparing backface and flamefront thermal expansions for selected samples.

FLOW →

250 μm
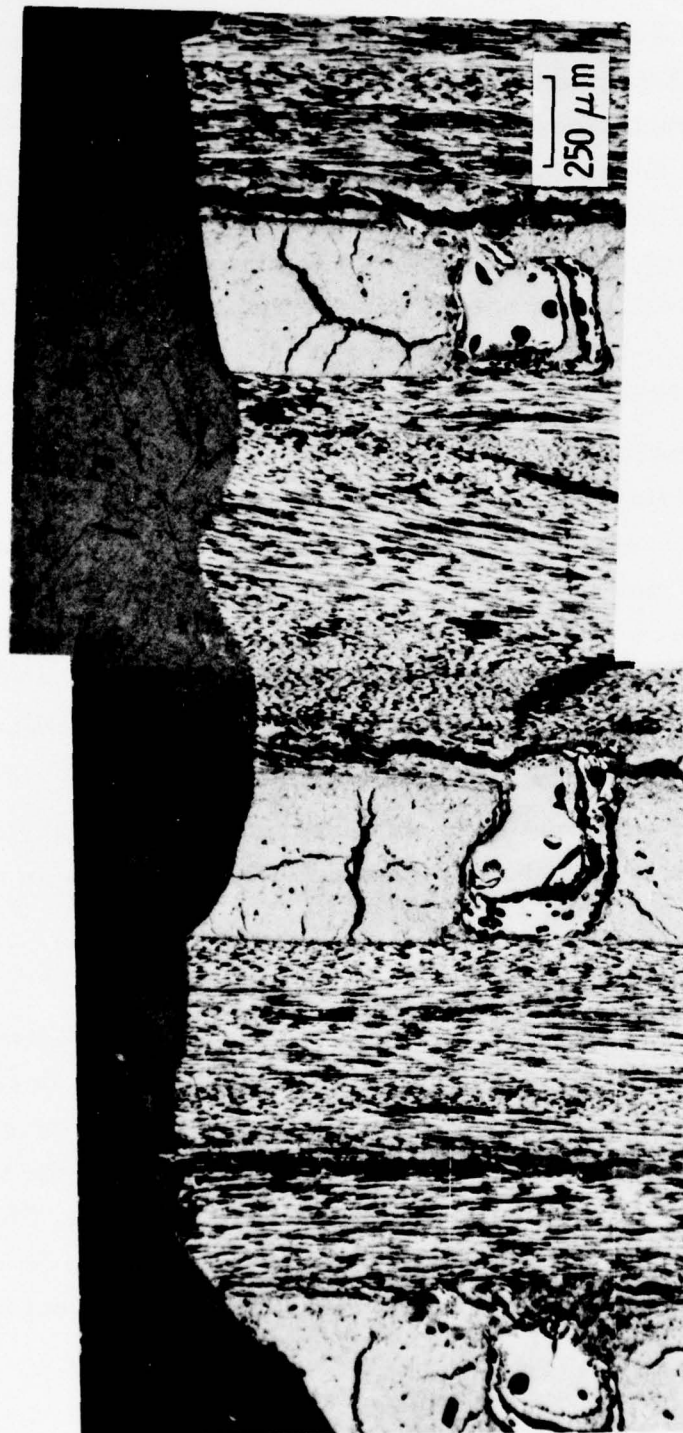
Figure 83. Portion of Sample 3D-2 with Surface Continuity Across Cracks Shown
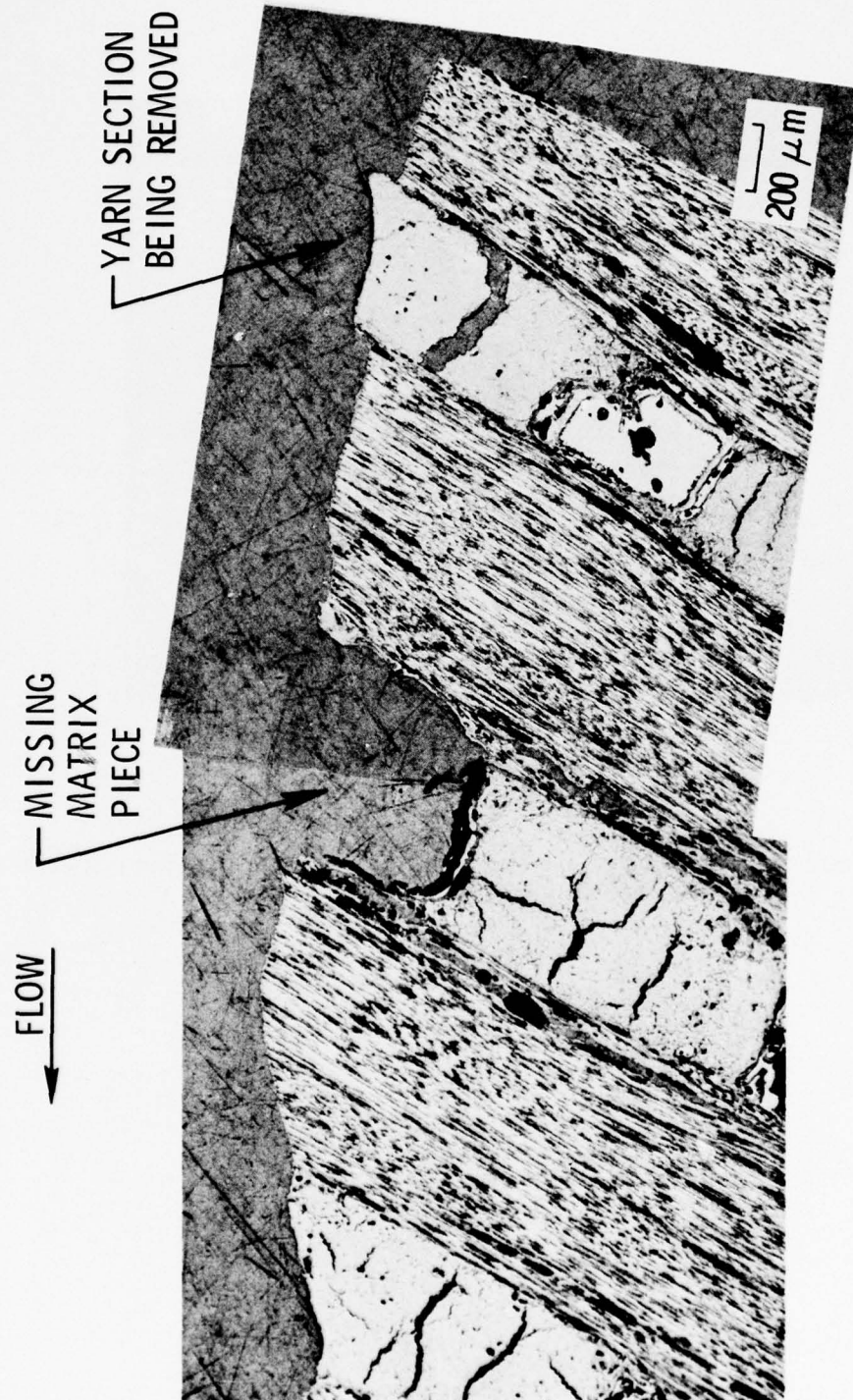
Figure 84. Portion of Sample 3D-3 with Evidence of Mechanical Erosion Shown
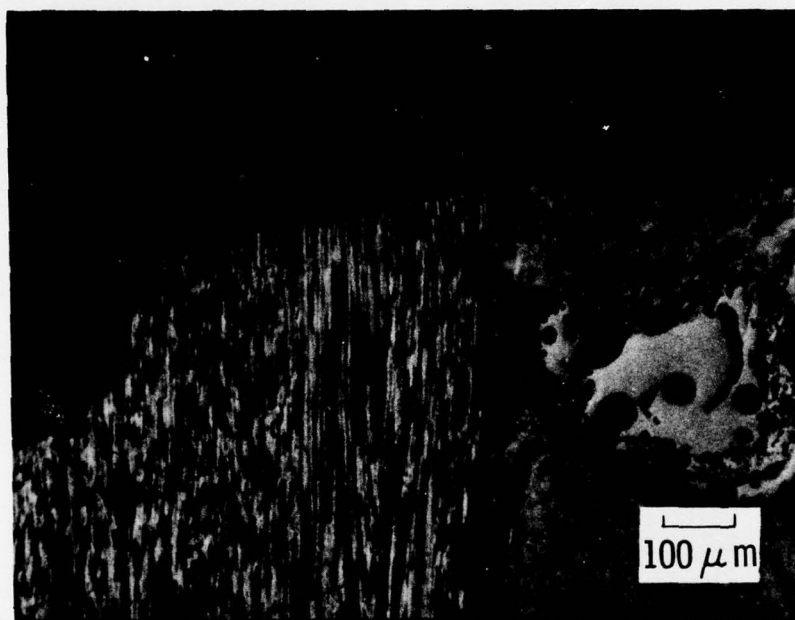
Figure 85. Portion of Sample 3D-1 with Film at Exposed Surface Shown

Thermal expansion was selected for this study because of the high degree of sensitivity this property has to both processing conditions and firing conditions. A Letiz model VBD quartz dilatometer was used for expansion determinations from room temperature to 2012°F (the upper limit of the equipment). Above 2012°F, a graphite tube furnace was utilized together with optical techniques for determining expansion. Dwell times were fixed at 15 min between readings for all materials, except that a 30-min hold was used to heat treat at 5432°F after the primary cycle was run. The optical device was a Gaertner telemicroscope with 50×10^6 divisions/in. In all cases, runs were made under an argon atmosphere and at ambient pressure. The dilatometer data were generated in a continuous and automated process, where $\Delta \ell / \ell_o$ x-y plots were inscribed on light-sensitive film.

The with-ply and cross-ply thermal expansion curves for entrance SN001 are shown in Fig. 86. The samples were carefully cut from the rosette structure so that they would allow true with- and cross-ply measurement. After each primary run, the samples were heat treated for 30 min at 5432°F and rerun to check the thermal stability in each direction. The stability of this material is evidenced by the way the expansion after 30 min at 5432°F closely matches the initial excursions. Indications are that this material was heat treated to 5432°F, or that firing itself had effectively achieved a stabilization through the thickness of the part.

Results of the thermal expansion excursions to 5000°F for the 3D reinforced entrance SN002 in the axial, radial, and circumferential directions are shown in Figs. 87, 88, and 89, respectively. In each case, the stability check run is shown with the initial excursion. The initial cycles indicate that the radial thermal expansion is the highest for this material, on the order of 10 in./in. at ~5000°F. The circumferential expansion is approximately 7 in./in. at the same temperature, and the axial expansion is just over 4 in./in. The thermal expansion in each direction was decreased
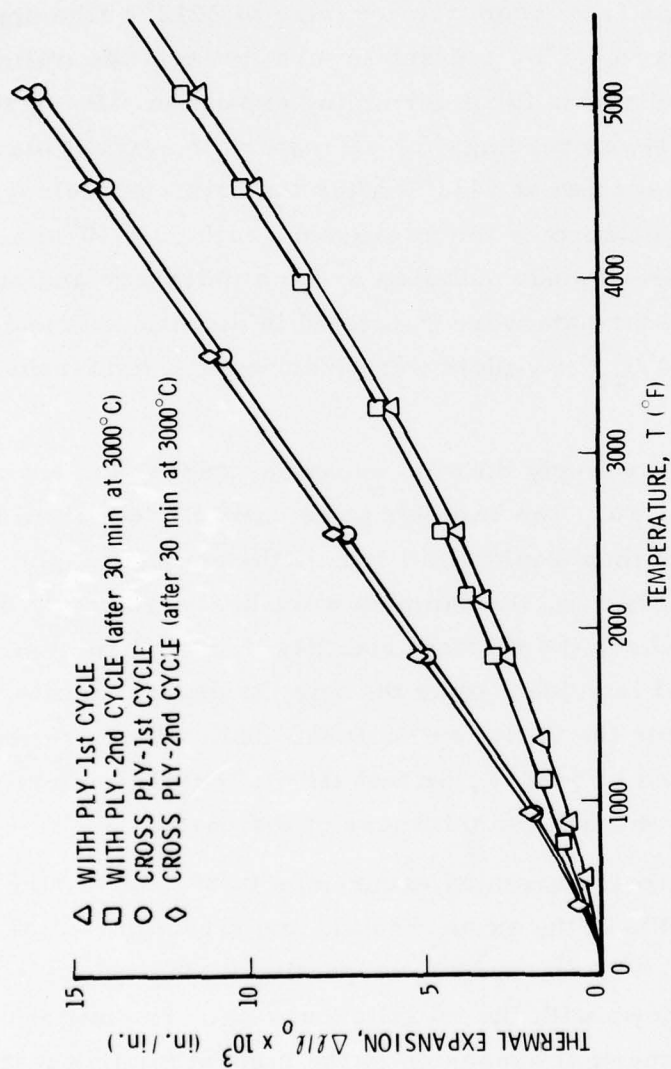
Figure 86. Thermal Expansion of Entrance SN001

Legend:
△ WITH PLY-1st CYCLE
□ WITH PLY-2nd CYCLE (after 30 min at 3000°C)
○ CROSS PLY-1st CYCLE
◇ CROSS PLY-2nd CYCLE (after 30 min at 3000°C)

X-axis: TEMPERATURE, T (°F)

Y-axis: THERMAL EXPANSION, $\Delta \ell / \ell_o$ x 10^3 (in./in.)
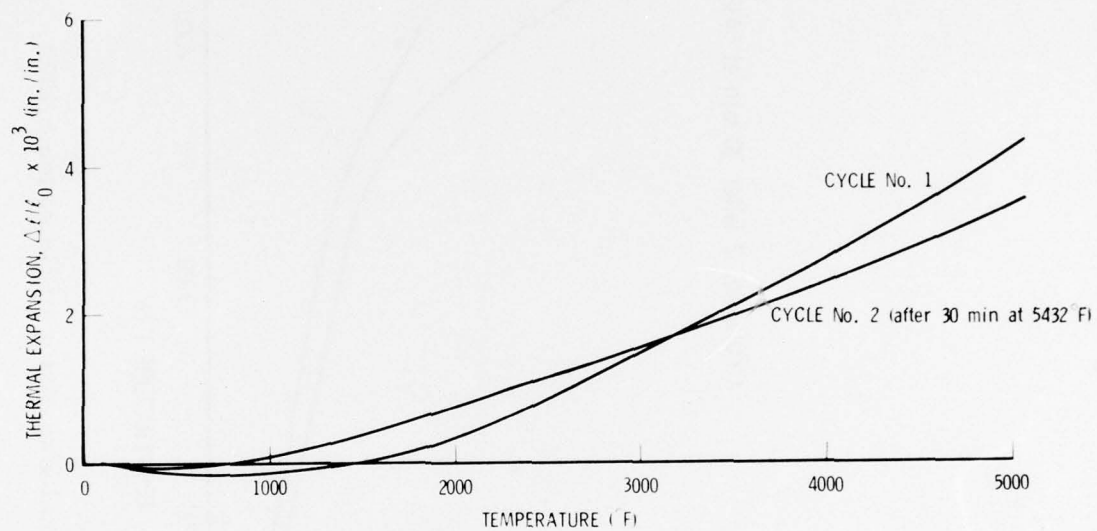
Figure 87.   Axial Thermal Expansion of Entrance SN002
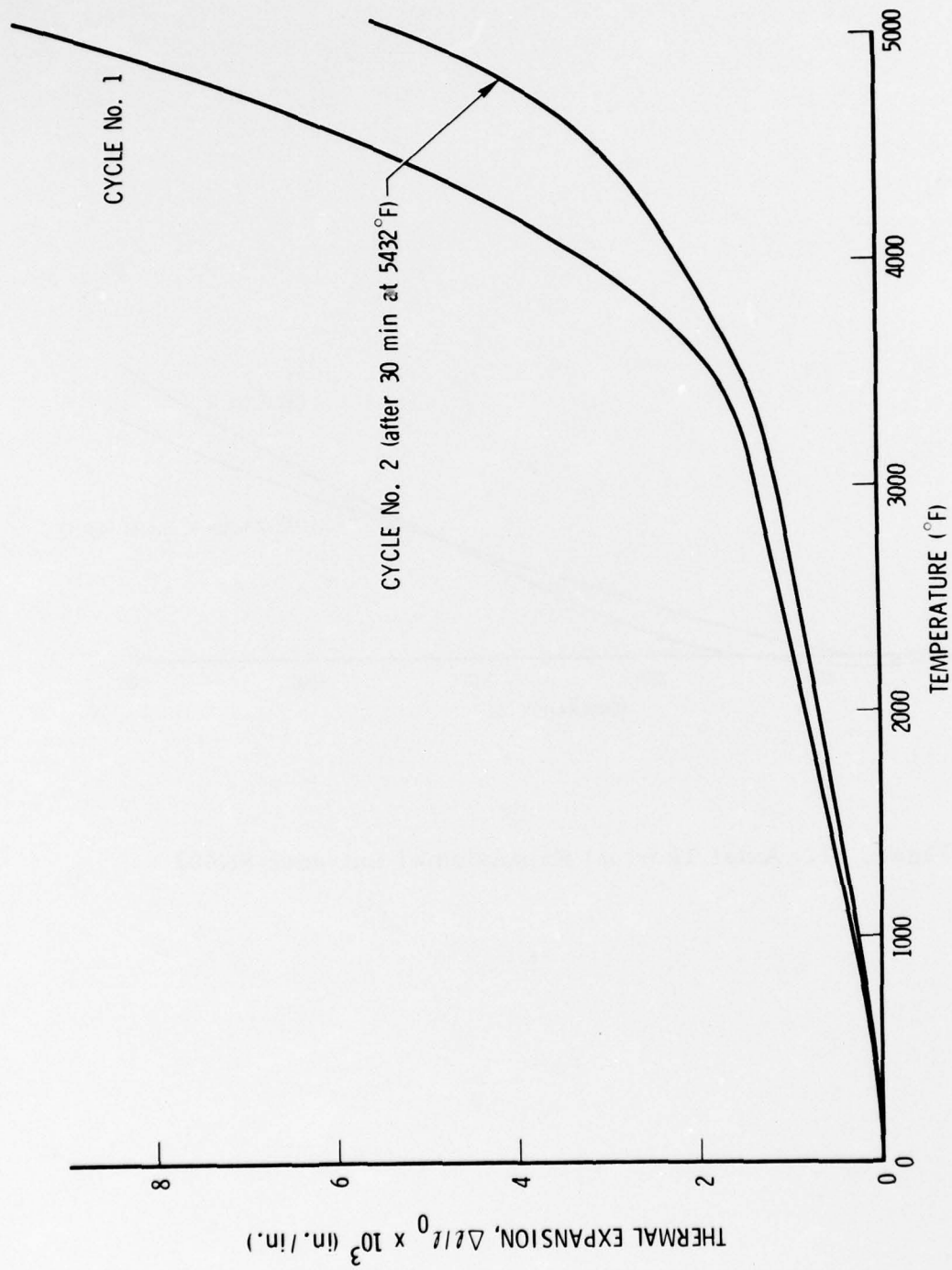
Figure 88. Radial Thermal Expansion of Entrance SN002
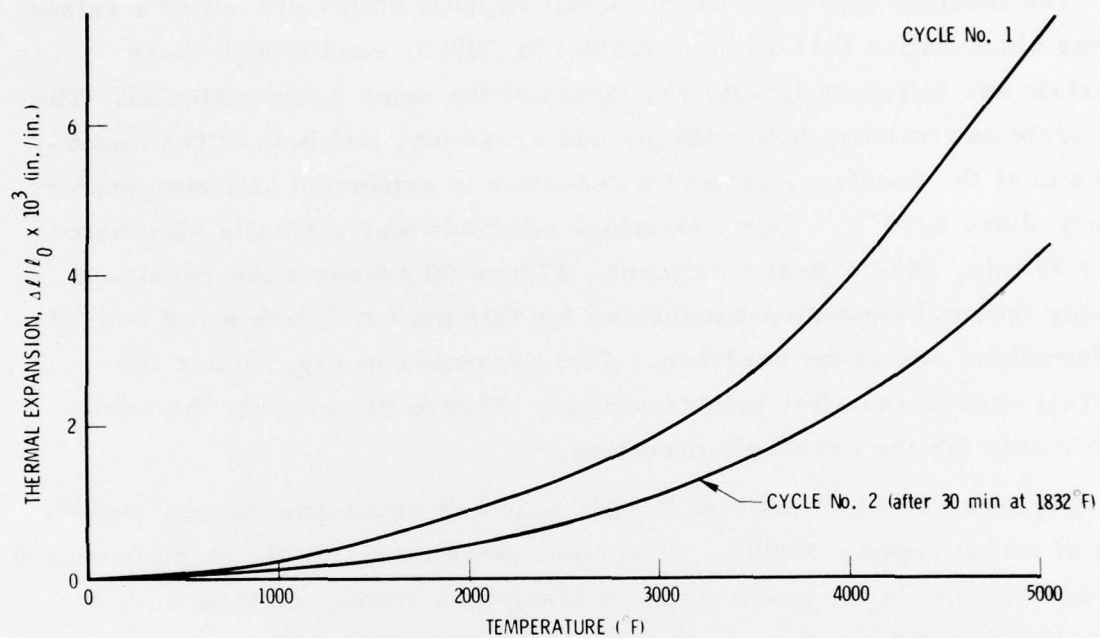
Figure 89. Circumferential Thermal Expansion of Entrance SN002

by the 30 min heat treatment at 5432°F. The net result was a condition approaching isotropic for the composite after heat treatment.

The thermal expansion of the throat support SN001 presented a rather curious phenomenon that was not evident in SN002, even though these materials are different density variations of the same basic material. The first cycle excursions, both with ply and cross ply, and both at the flame-front and at the backface, showed a reduction in expansion at a temperature slightly above 4000°F. This anomalous condition was virtually eliminated by the 30 min, 5432°F heat treatment. Figure 90 presents the results of with-ply thermal expansion excursions for this material monitored both at the flamefront and at the backface. Also presented in Fig. 90 are the resultant excursions after heat treatment. Figure 91 presents the comparable data for the cross-ply direction.

Figures 92 and 93 present the with-ply and cross-ply thermal expansions of throat support SN002. These data were taken for the flamefront and backface regions in the as-fired and heat-treated states, as they were for throat support SN001. None of the expansion reversal characteristics of SN001 was noted for SN002. After heat treatment, there was a tendency for both throat supports to develop similar thermal expansion characteristics. For example, the average with-ply thermal expansion of SN001 at 5000°F was 0.0041 in./in. after heat treatment. The comparable with-ply value for SN002 was 0.0042 in./in. Cross-ply values were 0.022 in./in. and 0.021 in./in. respectively. Translated to coefficients of thermal expansions (CTE), the data became 0.83×10^{-6} in./in./°F for SN001 with ply, 0.85×10^{-6} in./in./°F for SN002 with ply, 4.46×10^{-6} in./in./°F for SN001 cross ply, and 4.26 in./in./°F for SN002 cross ply.

E. DENSITY AND POROSITY

The density and porosity characteristics of the two entrances and the two throat supports were monitored as a part of this effort. These data were generated by combining data from optical pore counts, mercury
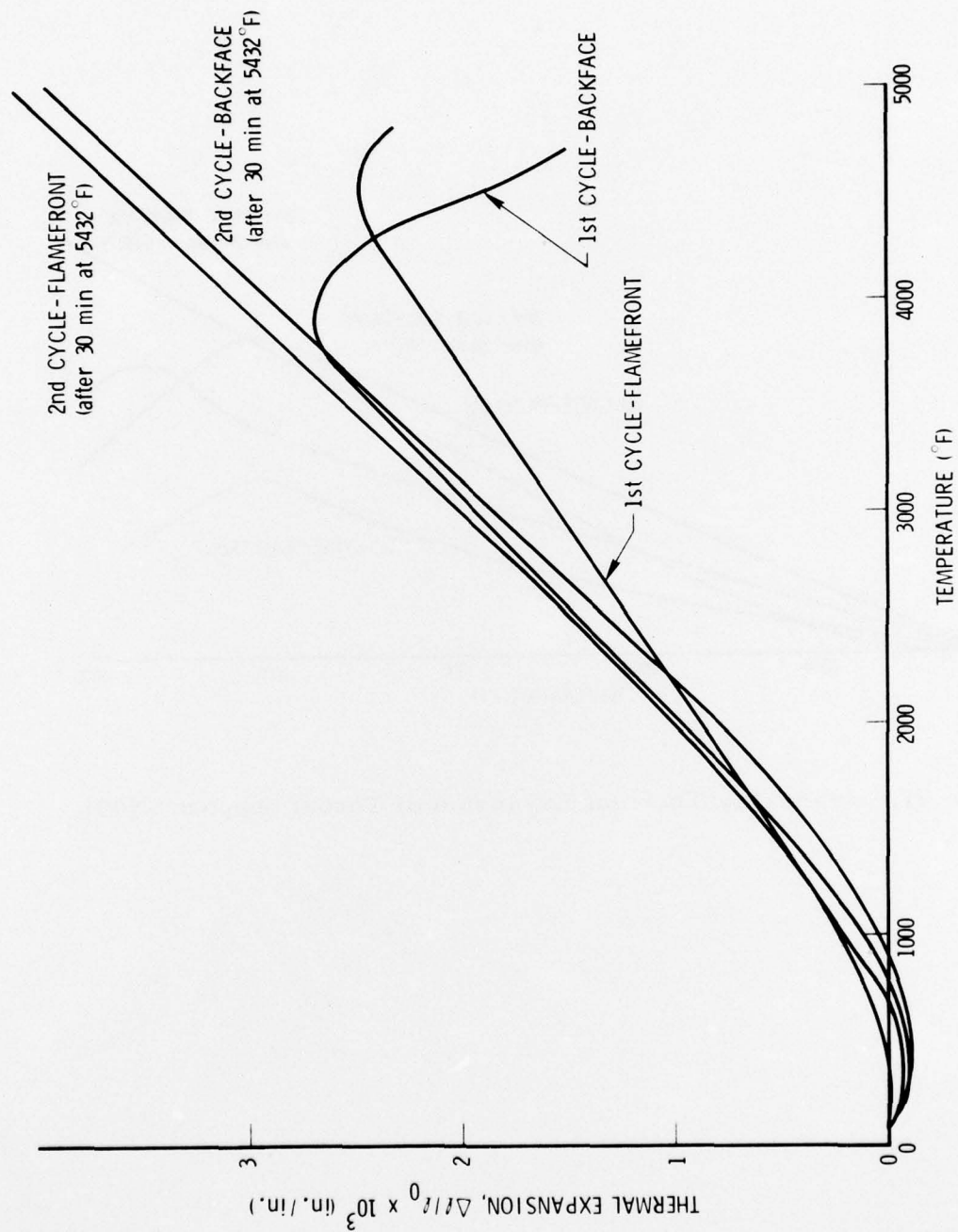
Figure 90. With-Ply Thermal Expansion of Throat Support SN001
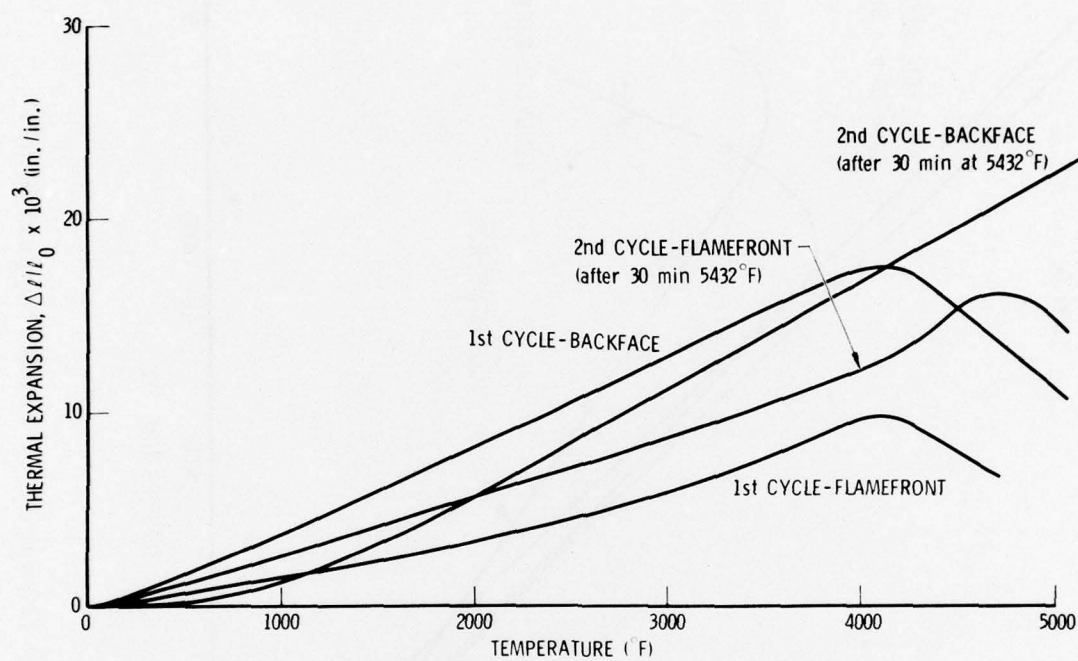
Figure 91. Cross-Ply Thermal Expansion of Throat Support SN001
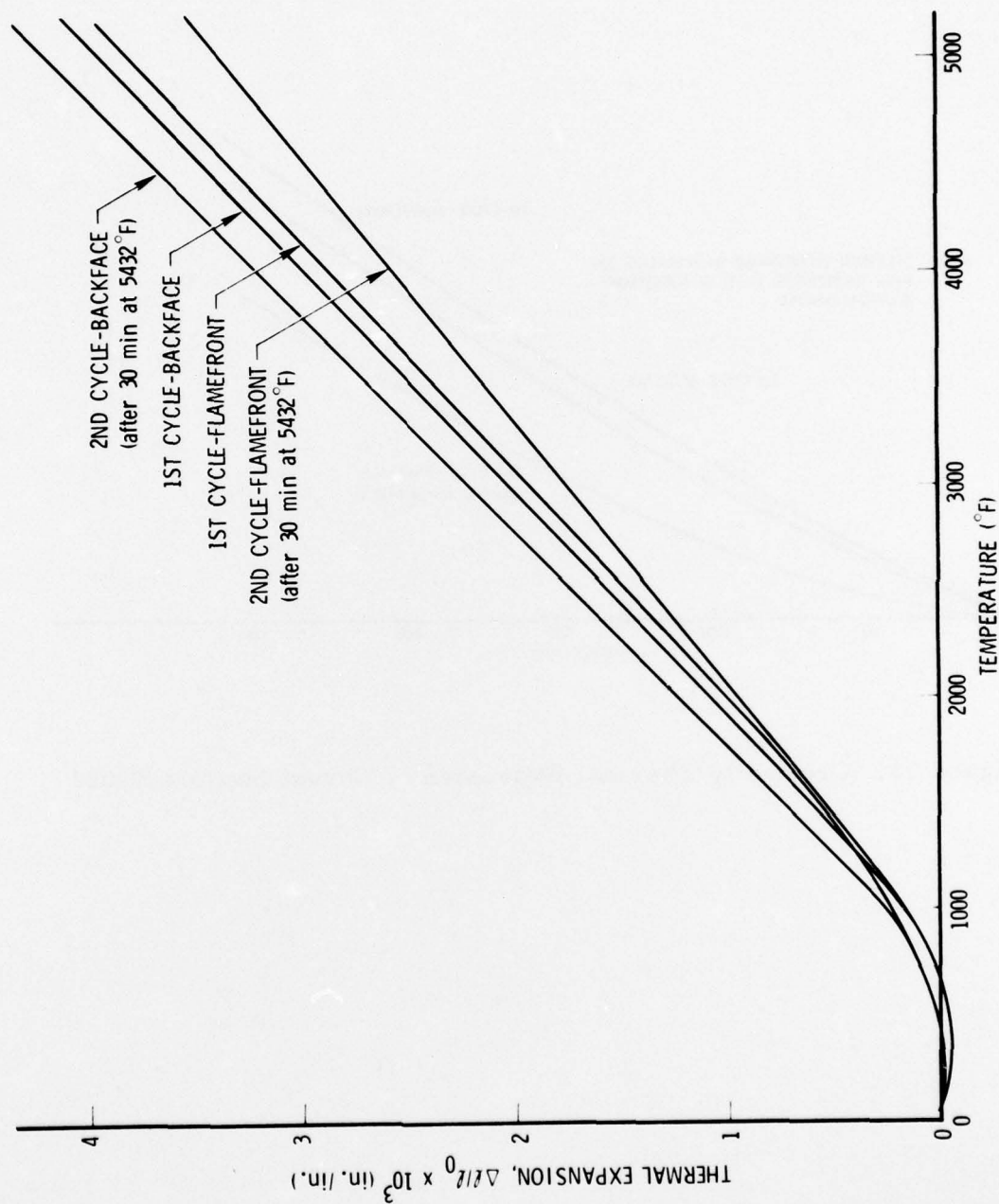
Figure 92. With-Ply Thermal Expansion of Throat Support SN002
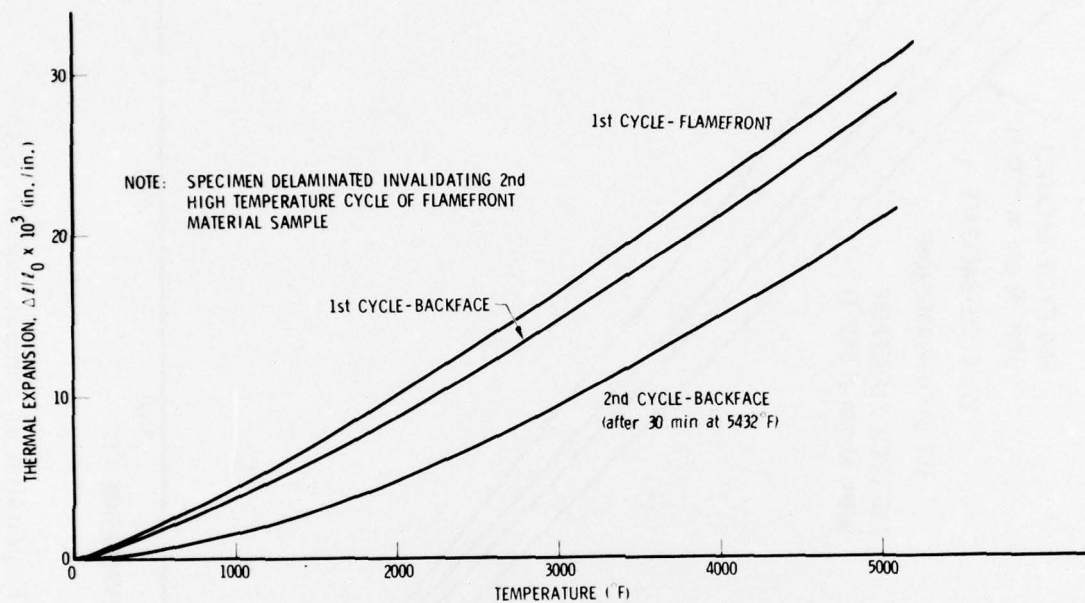
Figure 93. Cross-Ply Thermal Expansion of Throat Support SN002

intrusion, bulk density measurements, and the gas pycnometer. The measured data were then used to calculate percent open porosity from the relation

$$\epsilon_o = 1 - \frac{\rho_b}{\rho_a} \ (100)$$

where

ϵ_o = percent open porosity

ρ_b = bulk density

ρ_a = real apparent density

Percent total porosity is calculated from a modification of the above equation, which assumes that a true graphitic state exists for the composite, i.e., that the real density of the composite is 2.25 g/cm^3. This equation is given as

$$\epsilon_T = 1 - \frac{\rho_b}{2.25} \ (100)$$

where ϵ_T = percent total porosity. The total specific open pore volume $V_{\alpha o}$ is then

$$V_{\alpha o} = \frac{\epsilon_o}{100 \ \rho_b}$$

The values of bulk density, percent open porosity, percent total porosity, and specific open pore volume have been tabulated along with the values of open porosity expressed as a percentage of total porosity and are

shown in Table 7. These data have been generated for each material at the flamefront surface, in the interior, and at the backface.

Some noteworthy observations can be made from the data of Table 7. The 3D entrance had greater open porosity than either the rosette entrance or the flat laminate throat supports. However, it also exhibited the highest bulk density. This fact is consistent with the structure and the pitch matrix processing. This condition exists because the open porosity of the 3D entrance represents almost half of the total porosity, whereas the open porosity of the other carbon-carbon parts takes up little more than one quarter of the total porosity (Table 7). The 8 1/2% open porosity of the 3D part is somewhat higher than the 6 1/2 to 7 1/2% observed for T-50/pitch parts of like density, leading to the conjecture that processing may have been varied from these other parts. Another interesting observation can be made by examining the open porosity and porosity relationships of the two throat supports. The backface of SN001 and the flamefront of SN002 were subjected to porosity evaluation at the valley areas in the erosion profile (see section on microstructure). The total porosity in these areas is 10% higher than the other regions, and the open porosity is a whopping 30% greater. The bulk density in the valley areas is generally lower than in other locations of the same sample. On the basis of these factors, coupled with the evaluation of the microstructure, we conclude that there was most probably an unusual condition in the processing of these throat support elements (see Conclusions and Recommendations).

Table 7. Porosity Data Summary

Location		Bulk Density, g/cm³	Open Porosity, %	Total Porosity, %	Open Porosity, as % Total Porosity	Specific Open Pore Volume, cm³/g
Entrance SN001 AG Carb 101 Rosette (K408)	Backface	1.594	6.83	29.16	23.42	0.043
	Interior	1.593	7.06	29.20	24.18	0.044
	Flamefront	1.603	7.55	28.76	26.26	0.047
Entrance SN002 FMI T50 3D	Backface	1.825	8.52	18.89	45.11	0.047
	Interior	1.826	8.79	18.84	46.65	0.048
	Flamefront	1.835	8.39	18.44	45.49	0.046
Throat Support SN001 AG Carb 5451 (K550D)	Backface[a]	1.530	9.25	32.00	28.91	0.061
	Interior[b]	1.575	7.13	30.00	23.77	0.045
	Flamefront[b]	1.567	7.22	30.36	23.78	0.046
Throat Support SN002 AG Carb 5451 (K550D)	Backface[b]	1.761	7.22	21.73	33.22	0.041
	Interior[b]	1.697	7.42	24.58	30.19	0.044
	Flamefront[a]	1.676	9.01	25.51	35.32	0.054

[a] Measurements made in valley
[b] Measurements made on normal surface

Location

VALLEY — NORMAL SURFACE

LOCATION
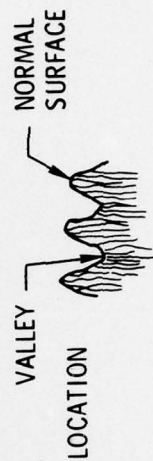
Reference Figs. 52 and 53

III. CONCLUSIONS AND RECOMMENDATIONS

A. CONCLUSIONS

The following summarizes the conclusions drawn from the characterization study performed on the two Aerojet MX upper stage subscale nozzles.

The overall performance of both entrance carbon-carbons and the throat retention carbon-carbons is satisfactory. The performance of the retainers, however, could be marginal for a more severe firing condition or for full-scale MX operation. A progression of the localized degradation could result in catastrophic failure of ply sets and subsequent failure or ejection of the throat pack. With only the erosion rate considered, all parts performed well and were consistent with the measured bulk densities.[4]

The rosette entrance, SN001, had an erosion rate, without pyrolytic graphite coating, of approximately 14 mil/sec as measured by ASPC. This rate matches that expected for a 1.6 g/cm^3 carbon part at these area ratios, with this propellant.[4] By means of a micro and macro roughness scale, the SN001 surface condition was determined to be smoother than the entrance SN002 surface. The interior structure of the part was mechanically sound. However, surface delaminations of the rosette indicate a potential danger when using this construction in this area of the nozzle.

The entrance SN002 appeared to be in excellent structural condition. The ASPC-measured average erosion rate of 9 mils/sec at the throat matches the predicted rate for a 1.85 g/cm^3 material. The 3D weave was geometrically true, and the composite exhibited no gross cracking. This part showed

---

[4]J. G. Baetz, "Advanced Carbon-Carbon Materials for Solid Rocket Nozzles," AIAA Paper No. 74-1057, presented at AIAA/SAE 10th Propulsion Conference, San Diego, California (October 1974).

less tendency toward the grooving response to the propellant grain configuration than entrance SN001.

Although the general performances of both throat retention parts have been considered satisfactory in their response to erosion, the overall reliability and predictability are marginal. The sawtooth erosion profiles of both throat retention elements were unusual and appeared to have been caused by an undesirable processing practice and not by an inherent material response characteristic. The erosion pattern was associated with density differences that appear to have been caused by processing sets of laminates. The open porosity of the throat retainers was significantly higher in the valleys than on the rest of the structure, and the bulk density was considerably lower in these same locations.

It is surprising to discover the large number of processing variables observed in all programs involving carbon-carbon materials.

More detailed examinations of the microstructure of the four carbon-carbons led to the following additional conclusions:

1.   The exposed surface of the 2D rosette (SN001) appears to be smoother than the 3D cylindrical material (SN002). The existence of fiber bundle cracking in the 3D may contribute to its greater roughness; the greater coarseness of the 3D structure also appears to affect this roughness. For entrance SN002 the varying depths to which material change occurs is shown to be a function of both the constituent and its orientation. Posttest characterization suggests that preferential macro and microcracking occurred perpendicular to the graphitic basal planes and that the existing microcracks contribute to the affected depth. Crack propagation tests support this observation of easy cleavage perpendicular to the graphitic basal planes. Composite porosity, particularly within the bulk matrix pockets, results in a rougher surface than at any other location.

2.   Surface roughness of both entrances appears to increase with distance traveling from the nozzle entrance toward the throat. A drastic variation for entrances SN001 and SN002 in both recession and roughness at different circumferential locations was noted. The data in Table 6 place the degree of variation between a factor of 3 and 4. Since the propellant grain was slotted, it

appears that grain geometry has a significant impact on erosion. The propellant grain affects the flow symmetry in the nozzle. The slots result in regions of higher erosion and greater surface roughness.

3. The reinforcement material of the throat retainers was, in general, removed below the overall matrix-reinforcement interface. This removal appeared to be independent of the angle of the reinforcement to the gas stream.

4. The thermal stability characteristics of these carbon-carbon materials were examined at progressively higher temperatures in an effort to study the onset of instability. The following observations were made:

    a. The thermal expansion of the rosette entrance indicated that this material had been stabilized to at least 5432°F. It is possible that this condition was affected by the rocket motor firing itself, but it is more likely that it was the result of processing. (The surface temperature would not exceed 5432°F for more than a few seconds, if at all, during this test.)

    b. The 3D entrance material was effectively stabilized during the heat treatment cycle imposed in this study. The thermal state approached an isotropic condition with heat treatment, and may be useful in improving the overall material properties.

    c. The thermal expansion studies of the two throat support materials showed that neither had been completely stabilized, and that each had been processed to a different stability. (The onset of instability of SN001 was approximately 4000°F. This value of SN002 could not be pinpointed.) The instability was substantiated by the tendency for both throat retainers to develop similar thermal expansion characteristics after 30 min, 5432°F heat treatment cycles.

B. RECOMMENDATIONS

It is recommended that the processing records of any carbon-carbon parts be available and studied with the autopsy characterization in an attempt to pinpoint any nonstandard procedures, which can be accomplished in the future by obtaining these records prior to the autopsy.

Observations indicate that the utilization of a heat-treatment cycle to stabilize the 3D entrance and to create an isotropic part may be a means of improving overall performance by creating a more stable composite.

Mass loss and surface smoothness may be enhanced by implementing the following recommendations:

1. Reduce the thickness of macrocracking between fiber bundles.

2. Increase interfilament matrix random orientation to reduce the long-range order and parallel orientation of low-pressure processed material.

3. Reduce the amount of porosity within the bulk matrix.

4. Implement high-pressure pitch impregnation procedures possibly with a thin CVD coating (no initial low pressure cycles) and cycle resin impregnation with appropriate cure cycles to reduce porosity (single graphitization of bulk matrix to reduce degree of graphitic orientation).

Continued microstructural characterization of fired surface and in-depth analyses are strongly recommended. Pretest samples would be an aid to material degradation assessment. Crack propagation should be continued on both pretest and posttest material but in a tensile mode to achieve uniform strain.

THE IVAN A. GETTING LABORATORIES

The Laboratory Operations of The Aerospace Corporation is conducting experimental and theoretical investigations necessary for the evaluation and application of scientific advances to new military concepts and systems. Versatility and flexibility have been developed to a high degree by the laboratory personnel in dealing with the many problems encountered in the nation's rapidly developing space and missile systems. Expertise in the latest scientific developments is vital to the accomplishment of tasks related to these problems. The laboratories that contribute to this research are:

Aerophysics Laboratory: Launch and reentry aerodynamics, heat transfer, reentry physics, chemical kinetics, structural mechanics, flight dynamics, atmospheric pollution, and high-power gas lasers.

Chemistry and Physics Laboratory: Atmospheric reactions and atmospheric optics, chemical reactions in polluted atmospheres, chemical reactions of excited species in rocket plumes, chemical thermodynamics, plasma and laser-induced reactions, laser chemistry, propulsion chemistry, space vacuum and radiation effects on materials, lubrication and surface phenomena, photosensitive materials and sensors, high precision laser ranging, and the application of physics and chemistry to problems of law enforcement and biomedicine.

Electronics Research Laboratory: Electromagnetic theory, devices, and propagation phenomena, including plasma electromagnetics; quantum electronics, lasers, and electro-optics; communication sciences, applied electronics, semiconducting, superconducting, and crystal device physics, optical and acoustical imaging; atmospheric pollution; millimeter wave and far-infrared technology.

Materials Sciences Laboratory: Development of new materials; metal matrix composites and new forms of carbon; test and evaluation of graphite and ceramics in reentry; spacecraft materials and electronic components in nuclear weapons environment; application of fracture mechanics to stress corrosion and fatigue-induced fractures in structural metals.

Space Sciences Laboratory: Atmospheric and ionospheric physics, radiation from the atmosphere, density and composition of the atmosphere, aurorae and airglow; magnetospheric physics, cosmic rays, generation and propagation of plasma waves in the magnetosphere; solar physics, studies of solar magnetic fields; space astronomy, x-ray astronomy; the effects of nuclear explosions, magnetic storms, and solar activity on the earth's atmosphere, ionosphere, and magnetosphere; the effects of optical, electromagnetic, and particulate radiations in space on space systems.

THE AEROSPACE CORPORATION
El Segundo, California